
Interaction between the neoclassical equilibrium and microturbulence in gyrokinetic simulations

Michael Oberparleiter

2015

Interaction between the neoclassical equilibrium and microturbulence in gyrokinetic simulations

Michael Oberparleiter

Dissertation zur Erlangung des Doktorgrades
Dr. rer. nat.
an der Fakultät für Naturwissenschaften
der Universität Ulm

vorgelegt von
Michael Oberparleiter
aus Roth

Ulm 2015

Amtierender Dekan: Prof. Dr. Joachim Ankerhold
Erstgutachter: Prof. Dr. Frank Jenko
Zweitgutachter: Prof. Dr. Joachim Ankerhold
Tag der Promotion: 10.07.2015

Abstract

The Sun is the omnipresent demonstration of the immense energy output generated by the nuclear fusion of hydrogen. Using this process as the heat source for electricity generation is thus not a far-fetched idea. The conditions necessary for a power plant, however, require temperatures of $10^7 - 10^8$ K if the fuel is magnetically confined. Hence, it is crucial to understand the processes which determine how well the emerging hot plasma is confined by the helical magnetic field surrounding and permeating it. In modern-day tokamak devices it has been established that the steep pressure gradients lead to a state of turbulence which in turn gives rise to most of the cross-field transport for the main ion species. There is, however, another transport channel driven by collisions and the curvature of the magnetic field: The so-called neoclassical transport provides a steady level of cross-field particle and momentum flux even in cases when turbulence becomes weak or suppressed. Furthermore, neoclassical and turbulent phenomena are only independent of each other in the so-called local limit if the length scales governing each of them are sufficiently separate, i.e. the ratio ρ_* between the ion gyroradius and the pressure gradient length is small enough. The goal of this work is to quantify the last statement and to better understand how neoclassical effects and turbulence can influence each other when their scales are not disparate.

For this purpose, the most suitable theoretical description is the well-established gyrokinetic model. Due to its complexity very often only numerical solutions to it are feasible. In this work the nonlinear gyrokinetic turbulence code `GENE` is employed. First, its capabilities for purely neoclassical systems are improved and successfully tested. In particular, its ability to self-consistently calculate the neoclassical radial electric field in global simulations is successfully benchmarked against the radial force balance equation. Additionally, `GENE` is used to study the plasma region close to the very center of a tokamak. Standard neoclassical theory assumes that the transport at a certain radial position is determined by the local plasma parameters at this very position, but this assumption is no longer valid in the so-called potato region. Indeed, simulation results show the importance of nonlocal effects which the standard neoclassical model does not account for.

In the next step a model system in the flux-tube limit which only considers a small plasma region around a specific field line is studied. There a sinusoidal long-wavelength external potential - based on the observed shape of the neoclassical field in global simulations - is imposed on ion temperature gradient-driven (ITG) turbulence. The comparably low computational cost of this system allows to study a wider range of physical parameters. With these simulations it is found that the presence of an external potential has a fundamental effect on the dynamics of the self-generated shear flow pattern of the turbulence: these zonal flows adapt to the imposed external pattern and even a small external $\mathbf{E} \times \mathbf{B}$ shear is sufficient to notably reduce turbulent cross-field energy transport.

Motivated by these indications for an interaction mechanism between neoclassics and turbulence global ITG simulations with fixed ion temperature gradient profiles are performed with and without inclusion of neoclassical effects. Comparison of these otherwise identical systems reveals that the presence of the neoclassical field enhances turbulent transport by 20 – 30% for $\rho_* > 1/300$. No difference is found for $\rho_* = 1/500$. A possible explanation found is that for high ρ_* the neoclassical field aligns a region of low $\mathbf{E} \times \mathbf{B}$ shear with the maximum of the gradient profile where the turbulent drive is strongest. Further investigation reveals that neoclassical effects also change the dependence of the system on physical parameters such as collisionality or the safety factor.

Finally, in physically more comprehensive (but computationally more demanding) simulations with fixed power input and a self-consistently evolving temperature profile, it is found that the presence of neoclassical phenomena modifies the self-organization behavior. For example, the additional neoclassical transport channel reduces the frequency and amplitude of intermittent turbulent transport bursts. The well-known phenomenon of profile stiffness is reproduced from three different power inputs.

Zusammenfassung

Die Sonne ist der allgegenwärtige Beweis für die hohe Energieausbeute der thermonuklearen Fusion von Wasserstoff. Es ist daher eine naheliegende Idee, diesen Prozess als Wärmequelle in der Elektrizitätserzeugung einzusetzen. Für den Betrieb eines Kraftwerks sind jedoch Temperaturen von $10^7 - 10^8$ K nötig, wenn der Brennstoff magnetisch eingeschlossen wird. Es ist daher wichtig die Prozesse zu verstehen, die bestimmen wie gut das Plasma durch das umgebende schraubenförmige Magnetfeld eingeschlossen wird. Bei modernen Experimenten vom Typ Tokamak ist bekannt, dass der steile Druckgradient im Plasma kleinskalige turbulente Fluktuationen antreibt, die wiederum für den überwiegenden Teil des radialen Teilchen- und Wärmetransports verantwortlich sind. Durch Stöße und die Krümmung des Magnetfeldes wird jedoch eine weitere Art von Transport angetrieben: Dieser sogenannte neoklassische Transport erzeugt ein stetes Niveau von radialem Fluss, selbst wenn die Turbulenz nur sehr schwach ist oder vollständig unterdrückt wird. Außerdem sind neoklassische und turbulente Phänomene nur im sogenannten lokalen Grenzfall unabhängig voneinander, d.h. wenn die jeweiligen mit ihnen verbundenen Längenskalen ausreichend verschieden sind. Mit anderen Worten, das Verhältnis ρ_* zwischen dem Ionengyroradius und der Abfalllänge des Druckgradienten muss klein genug sein. Ziel dieser Arbeit ist es letztere Aussage zu quantifizieren und besser zu verstehen, wie Neoklassik und Turbulenz miteinander wechselwirken, wenn ihre Skalen ähnlich sind.

Die zu diesem Zweck am besten geeignete theoretische Beschreibung ist das gyrokinetische Modell. Wegen seiner Komplexität ist sehr häufig nur ein numerischer Lösungsansatz praktikabel. In dieser Arbeit wird der nichtlineare gyrokinetische Turbulenzcode GENE verwendet. Zunächst wird seine Infrastruktur für rein neoklassische Simulationen verbessert und erfolgreich getestet. Insbesondere wird das radiale neoklassische elektrische Feld, das in globalen Simulationen selbstkonsistent berechnet wird, erfolgreich mit dem radialen Kräftegleichgewicht verglichen. Weiterhin wird mit GENE der Bereich des Plasmas im Zentrum des Magnetfeldes untersucht. Die neoklassische Standardtheorie enthält die Annahme, dass der Transport an einer bestimmten radialen Position durch die Plasmaparameter an genau dieser Position bestimmt ist, ihre Gültigkeit und diese Annahme ist in der sogenannten Kartoffelregion nicht mehr gültig. In der Tat zeigen Simulationsergebnisse die Bedeutsamkeit von nichtlokalen Effekten, die in der neoklassischen Standardtheorie nicht enthalten sind.

Als nächster Schritt wird ein Modellsystem in der Flussschlauchnäherung, die nur eine kleine Region in der Umgebung einer spezifischen Feldlinie betrachtet, untersucht. Dort wirkt ein sinusförmiges externes elektrostatisches Potential (basierend auf der Form des globalen radialen neoklassischen Feldes) auf Turbulenz, die vom Gradienten der Ionentemperatur (ITG) getrieben wird. Wegen des vergleichsweise niedrigen Rechenzeitaufwandes für dieses System ist es hiermit möglich einen großen Parameterbereich zu betrachten. Das Ergebnis dieser Simulationen ist, dass die Gegenwart des externen Potentials grundlegende Auswirkungen auf die Dynamik der intrinsischen Scherströmungen der Turbulenz hat: Diese sogenannten zonalen Flüsse passen sich der von außen vorgegebenen Struktur an. Außerdem ist erkennbar, dass bereits eine kleine externe $E \times B$ -Scherrate genügt um den radialen turbulenten Wärmefluss merklich zu verringern.

Ausgehend von diesen Anhaltspunkten für einen Wechselwirkungsmechanismus zwischen Neoklassik und Turbulenz werden globale ITG-Simulationen mit festgelegten Temperaturgradientenprofilen durchgeführt, jeweils mit und ohne neoklassische Effekte. Im Vergleich dieser ansonsten identischen Systeme zeigt

sich, dass für $\rho_* > 1/300$ bei Anwesenheit des neoklassischen Feldes der turbulente Wärmetransport um 20 – 30% höher ist, während bei $\rho_* = 1/500$ kein signifikanter Unterschied messbar ist. Eine mögliche Erklärung ist, dass das neoklassische Feld bei großem ρ_* einen Bereich mit schwacher $\mathbf{E} \times \mathbf{B}$ -Scherrate am Maximum des Temperaturgradientenprofils und damit am stärksten Antrieb der Turbulenz positioniert. Weitere Untersuchungen zeigen, dass neoklassische Effekte auch den Einfluss von Parametern wie Stoßfrequenz oder Sicherheitsfaktorprofil verändern.

Zuletzt werden physikalisch umfassendere (jedoch rechenaufwändigere) Simulationen mit festgelegter Leistungszufuhr und sich selbstkonsistent entwickelnden Profilen durchgeführt. Dabei zeigt sich, dass neoklassische Effekte die Selbstorganisation des Systems beeinflussen, z.B. in Form seltenerer und schwächerer Lawinen turbulenten Transports. Der bekannte Effekt der Profilsteifheit kann für drei Leistungszufuhren ebenfalls beobachtet werden.

Contents

Abstract	i
Zusammenfassung	iii
Contents	v
1 Introduction	1
1.1 Nuclear fusion	1
1.2 Magnetic confinement	2
1.2.1 The Tokamak	3
1.2.2 The Stellarator	3
1.3 Transport processes and modeling	4
1.4 Scope of this thesis	5
2 Theoretical model	7
2.1 Basic geometry of a tokamak	7
2.2 The single particle description	9
2.2.1 Gyro-orbits and classical transport	9
2.2.2 Drift orbits and neoclassical transport	10
2.2.3 Turbulent transport	13
2.3 The gyrokinetic description	13
2.3.1 Gyrokinetic ordering	14
2.3.2 The guiding-center and gyro-center transformation	15
2.3.3 The gyrokinetic Vlasov equation	17
2.3.4 The collision operator	19
2.3.5 Field aligned coordinates	21
2.3.6 The Poisson equation	22
2.3.7 The drift-kinetic limit	24
2.4 Summary	25
3 Numerical implementation of the gyrokinetic equation	27
3.1 Local and global simulations	27
3.2 Numerical approach in GENE	28
3.2.1 Coordinate choice and boundary conditions	29
3.2.2 Discretization schemes	32
3.3 Normalization	33

3.3.1	Basic quantities	33
3.3.2	Dimensionless parameters	34
3.3.3	Kinetic and Poisson equation	35
3.4	Steady state in global simulations	35
3.4.1	Gradient-driven setup	36
3.4.2	Flux-driven setup	37
3.5	Observables	38
3.5.1	Turbulent fluxes	39
3.5.2	Neoclassical fluxes	40
3.5.3	Error estimation for the fluxes	43
3.6	Summary	48
4	Purely neoclassical systems	49
4.1	Local neoclassical benchmarks	49
4.2	Radially global simulations	52
4.2.1	The radial electric field	52
4.2.2	The effects of potato orbits	54
4.3	Summary	60
5	Effects of non-turbulent electrostatic fields on ITG turbulence	63
5.1	Turbulence saturation by zonal flows	63
5.2	Effects of long wavelength external potentials	66
5.3	Summary	71
6	Synergy between turbulence and neoclassical effects	73
6.1	Gradient-driven setups	73
6.1.1	System size effects	74
6.1.2	Collisionality effects	79
6.1.3	Safety factor effects	80
6.2	Flux-driven setups	82
6.3	Summary	87
7	Conclusions	89
7.1	Summary	89
7.2	Outlook	91
A	Definitions of collision frequencies	93
	Bibliography	95
	Curriculum Vitae	101
	Danksagung	103

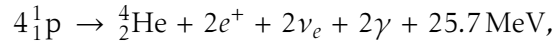
Chapter 1

Introduction

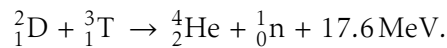
“Several billion trillion tons of superhot exploding hydrogen nuclei rose slowly above the horizon and managed to look small, cold and slightly damp.” - *Douglas Adams: Life, The Universe and Everything*

1.1 Nuclear fusion

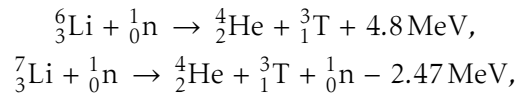
The question about the nature of the Sun is probably one of the oldest questions of mankind. We have come a long way from shining divine chariots to the discovery that it generates energy through the fusion of light nuclei, particularly hydrogen, into heavier ones [1]. The next step from there was if and how this process can be reproduced under controlled conditions on Earth to directly access its obviously high energy yield. As it turns out, the predominant fusion reaction of the Sun, the proton-proton chain,



is not well suited for this, as its first step involves the weak interaction leading to a very low reaction cross-section. While it is enough for a star to be in an equilibrium state with the immense gravity from its total mass, the most accessible process on terrestrial scales is instead the fusion of the heavier isotopes of hydrogen, deuterium and tritium:



Deuterium accounts for about 0.016% of naturally occurring hydrogen in the oceans, which means that it is abundant on Earth. The radioactive tritium, on the other hand, has a half-life of about 12 years and can thus be only found in trace amounts. It can be produced, however, by a nuclear reaction from lithium:



where the neutron from the fusion reaction can be used.

The D-T fusion reaction has been successfully applied on a large scale since the 1950s - unfortunately only in its uncontrolled form as the hydrogen bomb. Applying it in a peaceful way as the energy source for a power plant to generate electricity without

carbon dioxide emissions has evolved to be a greater challenge than anticipated by the pioneers of the field in the 1960s.

For nuclear fusion to occur the involved nuclei need to overcome the Coulomb barrier where "overcome" is used in the sense of being close enough for a high chance of tunneling. In terms of a collective state this means a very high temperature T to have particles with sufficient kinetic energy, a density n that provides enough collisions and a means of confinement for the fuel to sustain the former two conditions long enough. These circumstances can be summarized in the Lawson criterion:

$$nT\tau_E \gtrsim 10^{21} \frac{\text{keV} \cdot \text{s}}{\text{m}^3}, \quad (1.1)$$

where the energy confinement time τ_E quantifies the energy losses to the environment. Fulfilling this criterion means that the fuel has reached ignition, i.e. the fusion reaction sustains itself without external energy input.

The most straightforward approach to this is inertial confinement, where the only limiting factor for the rapid expansion of the system is the inertia of the fusion fuel. Obviously, this means that an intense initial compression is critical for a high fuel conversion rate and energy output. This is achieved by a shock wave created by, for example, a runaway fission reaction (in the case of warheads) or by a high-powered laser pulse [2]. It is inherently difficult to use inertial confinement in a steady-state process, which would be desirable for an electric power plant. Thus, there are other approaches, which use low density and compensate by higher temperatures and confinement times, namely confinement by magnetic fields.

1.2 Magnetic confinement

Hydrogen that is heated to the necessary temperatures for fusion of around $10^7 - 10^8$ K (equivalent to energies of $10 - 20 \text{ keV}^1$) becomes an ionized gas, a so-called plasma. It consists mainly of charged particles and can thus be influenced and confined by magnetic fields via the Lorentz force which restricts cross-field movement. Due to the high particle energy this requires typically a magnetic field strength of several Tesla. Then the confinement properties of the device are determined by the magnetic topology and shape of the field.

After early experiments with cylindrical configurations it became clear that the (so far) best concept is to have a toroidal geometry with magnetic field lines winding helically around the torus. In a purely toroidal field magnetic drifts would lead to charge separation, generating an electric field which in turn would lead to a radial $\mathbf{E} \times \mathbf{B}$ drift (see Sec. 2.2.2). The most prominent forms to technically realize a helical field on an annular shape are the *tokamak* [3] (from the transliteration of Russian "токамак", an acronym for "toroidal chamber with magnetic coils") and the *stellarator* [4] (from Latin "stella" = star).

¹A very popular definition in plasma physics is to measure temperatures in units of energy.

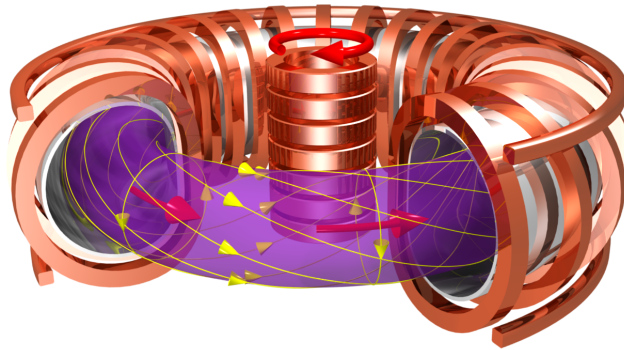


Figure 1.1: Coil system (orange), currents (red) and magnetic field (yellow) of a tokamak
(Source: IPP, Dr. Christian Brandt)

1.2.1 The Tokamak

The magnetic field for a tokamak has two contributions: The strong toroidal field B_t is generated by an annulus of planar coils around the plasma, while the weaker poloidal field B_p is generated by a toroidal current in the plasma. This current is driven inductively by a solenoid in the center of the torus (see Fig. 1.1). A fundamental property of the resulting field is that it is *axisymmetric*, i.e. symmetric in regard to the central axis of the torus. Additionally, toroidal coils are used to shape the poloidal cross-section of the plasma into a characteristic form.

As a result of its construction principle the machine is operating in pulses limited by the current ramps in the central coil. There are other means to drive a current in the plasma, such as the injection of neutral beams or the intrinsic bootstrap current (see Sec. 2.2.2), but they can only contribute to the toroidal current, not sustain it by themselves. Nonetheless, the tokamak has shown to be a successful line of research: Single experiments at the JET tokamak have reached around two thirds of energetic break-even and the ITER project, which is currently under construction at Cadarache in France, is planned to produce 500 MW of fusion power with a heating power of 50 MW.

1.2.2 The Stellarator

The magnetic field of a stellarator is completely generated by external coils, avoiding the necessity of driving a plasma current and allowing steady-state operation. This comes at the price of giving up axisymmetry and, as it turned out, having to use computer-optimized complex three-dimensional coil designs (see Fig. 1.2) to avoid catastrophic transport losses. Thus stellarator development has been lagging behind tokamak research. With the advent of high capacity computing and advanced manufacturing methods, however, it is nowadays a very active field of research and development.

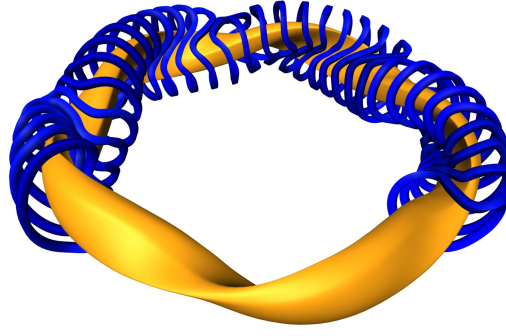


Figure 1.2: Coils and plasma shape of the stellarator Wendelstein 7-X (Source: IPP)

1.3 Transport processes and modeling

Since the energy confinement time τ_E is invariably connected to the cross-field transport of particles and energy (and to some degree also of momentum) in radial direction, the understanding of the processes governing it is one of the central goals of theoretical works in magnetic confinement fusion research. Two forms of transport are established to be important in this context: *Neoclassical* and *turbulent* transport. The former is driven by collisions between the confined particles and hence provides an essentially omnipresent level of minimum transport. The latter is usually much stronger in tokamaks and optimized stellarators² and is based on the system being far from thermodynamic equilibrium. The strong temperature and density gradients between core plasma and the edge (typically a drop from 10^7 K to 10^2 K) allows microinstabilities to grow and establish a state of turbulence.

The modeling formalism most suitable to describe these microinstabilities in a hot plasma with rare collisions is a *kinetic* treatment, which evolves a phase space distribution function for each species of the plasma (electrons and ions of hydrogen isotopes as well as of heavier impurities) according to the Vlasov equation (see Sec. 2.3). Although this is one of the most fundamental descriptions of a plasma, it poses a complex six-dimensional problem (3D in configuration, 3D in velocity space). In consequence, simplifications have to be made. If the plasma is magnetized, i.e. the dynamics are dominated by a strong magnetic background field, it is, for example, possible to average over the fast gyration around the magnetic field lines thus reducing dimensionality to 5D and removing the necessity to resolve a comparably fast timescale. If this is done in a way that consistently accounts for gyroradius scale fluctuations of the electromagnetic fields, the resulting model is called *gyrokinetic* theory. It also covers not only turbulent transport but also as a subset neoclassical transport and is the basis of multiple numerical modeling efforts for magnetic confinement fusion experiments.

²These modern stellarators, like Wendelstein 7-X, are, in fact, optimized to minimize neoclassical transport.

1.4 Scope of this thesis

In this work the gyrokinetic nonlinear Vlasov code `GENE` is employed and extended to study possible interaction mechanisms between the (usually) dominant turbulent transport and the subdominant neoclassical transport. In many cases both effects are treated separately and the total cross-field transport calculated by summation of the two. This can be analytically justified when the scale of the gyration movement is assumed to be infinitely small compared to the dimensions of the magnetic field or the time-averaged temperature and density gradients. In small devices or regions with steep gradients a clear scale separation is not possible and neoclassical effects can influence turbulence and vice versa. These steep gradients typically occur in zones of strongly reduced turbulence, so-called transport barriers. There is experimental [5] and theoretical [6] evidence that neoclassical transport and the neoclassical radial electric field are connected to the dynamics of barriers both in the core as well as the edge. This work forms the foundation for more comprehensive numerical investigations of transport barriers.

While some results in this work could also be applicable to stellarator physics, its focus lies exclusively on tokamaks. Accordingly, assumptions which only hold in a tokamak, such as axisymmetry of the magnetic guide field, are going to be used.

This thesis is structured in the following way: Chapter 2 contains a basic phenomenological description of neoclassical transport and an overview over the derivation of the gyrokinetic framework. It is also pointed out how this formalism covers not only the physics of turbulent transport but also contains neoclassical effects as a limit case. Chapter 3 covers how the equations are implemented in the `GENE` code with a focus on elements relevant to neoclassical transport and systems where it can interact with turbulence. Additionally, it is shown how to calculate the turbulent and neoclassical transport fluxes and discuss methods of estimating their uncertainty. Chapter 4 presents purely neoclassical simulations which confirm the validity of the simulation results for neoclassical transport in local simulations, demonstrate the ability to self-consistently calculate the neoclassical radial electric field in global simulations and finally study the nonlocal effects attributed to so-called potato orbits near the magnetic axis. In Chapter 5 the influence of low-wavelength electrostatic fields (similar to the neoclassical field) on local simulations of ion temperature gradient-driven (ITG) turbulence are studied. In Chapter 6 the interaction between neoclassical effects and ITG turbulence is demonstrated in global simulations both with fixed temperature gradient and fixed power input. Finally, Chapter 7 summarizes the results of this thesis and gives prospects for further investigations.

Chapter 2

Theoretical model

The magnetically confined plasmas in fusion applications are characterized by a high temperature and a low density and as a consequence by a very low number of collisions. Hence, a standard fluid model approach turns out to be insufficient for the mechanisms that drive plasma transport and a kinetic approach must be used. In order to better understand the phenomenon of neoclassical transport it is, however also helpful to consider the dynamics of single particles. This provides useful concepts such as the magnetic and the $E \times B$ drift velocities and allows for simple random walk estimates for the scalings of neoclassical transport. Afterwards we go through the steps of deriving the gyrokinetic Vlasov-Poisson equation system in the form it will be used in the numerical calculations of the following chapters.

2.1 Basic geometry of a tokamak

Before considering the dynamics of the plasma, we shall introduce the basic geometrical framework to operate on when describing tokamak physics. Obviously, the defining quantity for this is the magnetic field,

$$\mathbf{B} = \nabla \times \mathbf{A} = B_\varphi \hat{e}_\varphi + \nabla\psi \times \nabla\varphi, \quad (2.1)$$

$$\mathbf{B} = I(\psi)\nabla\varphi + \nabla\psi \times \nabla\varphi, \quad (2.2)$$

where φ is the toroidal angle and we have used the vector potential A to define the *poloidal flux function* $\psi = -RA_\varphi$ with R the distance from the axis of symmetry. Since

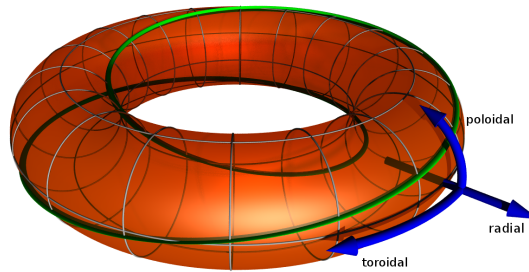


Figure 2.1: Basic tokamak shape with a $q = 2$ field line (green).

$\mathbf{B} \cdot \nabla \psi = 0$ holds, the magnetic field vector will lie on surfaces of constant ψ . This makes ψ one possible choice of a *flux surface* label. These surfaces form nested toroids in a tokamak.³ The innermost of these is degenerated to a circular line and called the *magnetic axis* where we set $\psi = 0$. Its radius is the *major radius* R_0 of the tokamak. The possible shapes of the flux surfaces are solutions of the Grad-Shafranov equation [7], which is derived from the magnetohydrodynamic equilibrium condition

$$\mathbf{j} \times \mathbf{B} = \nabla p.$$

The pressure $p = p(\psi)$ is an example of a *flux surface quantity*, i.e. a quantity that only depends on ψ . One possible solution are concentric (besides a small displacement of the center of the outer flux surfaces called Shafranov shift, which we neglect) circular toroids, which serve as a good model system for theoretical and numerical studies due to their symmetry. Obviously, this means that the distance of the surface from the magnetic axis is a function of ψ : $r = r(\psi)$. The radius of the outermost closed flux surface from the magnetic axis determines the *minor radius* a of the tokamak. The quotient

$$\epsilon = \frac{r}{R_0}$$

is called *inverse aspect ratio* and is an important dimensionless parameter.

If we introduce the poloidal angle θ as a third coordinate besides ψ and ϕ , we can define the volume element:

$$d^3x = \frac{d\psi d\theta d\phi}{|(\nabla\phi \times \nabla\psi) \cdot \nabla\theta|},$$

and with this the useful concept of the *flux surface average*, where we average over the volume between two neighboring flux surfaces at ψ and $\psi + d\psi$:

$$\langle Q \rangle(\psi) = \frac{\int Q(\psi, \theta) d^3x}{\int d^3x} = \oint \frac{Q(\psi, \theta)}{\mathbf{B} \cdot \nabla \theta} d\theta \bigg/ \oint \frac{1}{\mathbf{B} \cdot \nabla \theta} d\theta.$$

In case Q also is not axisymmetric (i.e. has a ϕ dependence), it also includes an integration over the toroidal angle.

The final parameter of the magnetic field we introduce here is the *safety factor*,

$$q = \frac{n_t}{n_p} = \frac{\langle \mathbf{B} \nabla \phi \rangle}{\langle \mathbf{B} \nabla \theta \rangle},$$

which describes the twistedness of the magnetic field, i.e. the number of toroidal turns n_t of a field line per poloidal turn n_p . It is a function of the radial position and its first order derivative is called the *magnetic shear*:

$$\hat{s} = \frac{1}{q} \frac{\partial q}{\partial r}.$$

³In experiments, situations occur where this does not hold anymore, such as the formation of magnetic islands which include stochastization of the field lines.

For the treatment of particle dynamics it is helpful to split velocities in components parallel and perpendicular to the background magnetic field (introducing $\hat{\mathbf{b}} = \mathbf{B}/B$):

$$\mathbf{v} = v_{\parallel} \hat{\mathbf{b}} + \mathbf{v}_{\perp}.$$

The sign of v_{\parallel} indicates if the velocity is co- or countercurrent to the field.

2.2 The single particle description

The most fundamental and intuitive approach for a theoretical description is to consider the trajectory of every particle in a plasma. While it is immediately obvious that this task is not feasible for a plasma consisting of about 10^{20} interacting particles, the picture is helpful to understand a number of phenomena relevant for this work in a qualitative and illustrative way.

2.2.1 Gyro-orbits and classical transport

Since the Lorentz force only restricts movement perpendicular to the magnetic field lines, the characteristic trajectory of electrons and ions is a helical curve. This movement determines two important characteristic scales of the plasma: the gyroradius (sometimes called Larmor radius) and the gyrofrequency:

$$\rho_{\sigma} = \frac{m_{\sigma} v_{\perp} c}{Z_{\sigma} e B}, \quad \Omega_{\sigma} = \frac{Z_{\sigma} e B}{m_{\sigma} c},$$

with mass m_{σ} , charge number Z_{σ} of the particle belonging to species σ , as well as the magnetic field B and perpendicular velocity v_{\perp} of the particle. Typical values for deuterium ions in fusion plasmas are a gyroradius in the millimeter range and a gyrofrequency around 10^{11} s^{-1} (where the machine dimensions amount to several meters). Hence, the magnetic field does not change notably over the time and space the particle needs to complete several gyrations and the magnetic moment,

$$\mu = \frac{m_{\sigma} v_{\perp}^2}{2B},$$

is a conserved quantity. This also includes the fact that collisions occur very infrequently. Such a plasma is called (strongly) magnetized.

Cross-field transport of particles, heat and momentum can be realized by collisions that displace the particles from their original field line as sketched in Fig. 2.2. It should be noted, though, that the shown large angle collision represents the net effect of many small angle collisions. This effect is known as *classical transport* [8]. Since the process is diffusive, its net transport can be estimated by a random walk argument with ρ as the step size. For the transport of electrons Γ_e due to a cross-field density gradient ∇n this results in:

$$\Gamma_e = -D_e \nabla n, \tag{2.3}$$

$$\text{with: } D_e \sim \frac{\rho_e^2}{2\tau_{ei}}, \tag{2.4}$$

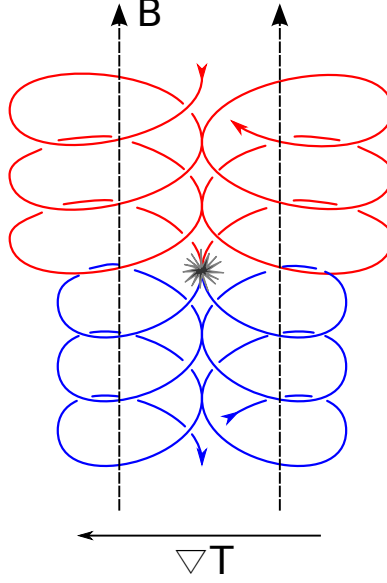


Figure 2.2: Principle of classical heat transport due to collisions in the presence of a temperature gradient

where τ_{ei} is the typical time for small-angle collisions of an electron with ions to accumulate to a 90° scattering. For the exact definition of τ_{ab} see Eq. (2.38). Analogously we find for the heat transport q_i by ions due to a temperature gradient ∇T :

$$q_i = -\kappa_i \nabla T, \quad (2.5)$$

$$\text{with: } \kappa_i \sim \frac{n_i \rho_i^2}{2\tau_{ii}}. \quad (2.6)$$

The contribution from ion-electron collisions can be neglected here, as it is smaller by a factor of the mass ratio m_e/m_i .

Because Coulomb collisions conserve momentum, particle transport by this mechanism must be automatically ambipolar, i.e. $\Gamma_i = \Gamma_e$, and self-collisions cannot contribute to particle transport. Classical transport turns out to have no significant contribution to the confinement time of fusion devices because it is very small compared to other effects that occur in toroidal magnetic field configurations.

2.2.2 Drift orbits and neoclassical transport

In the magnetic field of a tokamak the particle dynamics extend beyond the gyration. Movement of the particles' gyration centers is determined by three approximate constants of motion [9]: the magnetic moment μ , the total energy,

$$E = \frac{mv^2}{2} + Ze\phi,$$

where the electrostatic potential ϕ does not vary strongly on a flux surface, and the toroidal canonical momentum:

$$p_\phi = mRB_\phi v_\parallel / B - Ze\psi.$$

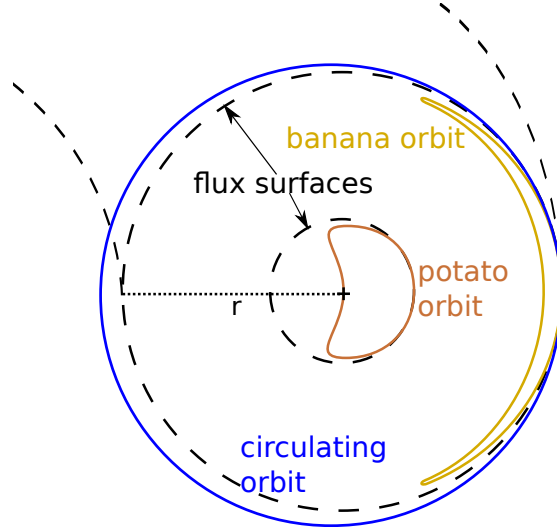


Figure 2.3: Poloidal projection of drift orbits in a tokamak

Since the strength of the magnetic field varies between B_{\max} on the inboard and B_{\min} on the outboard midplane, two distinct populations of particles exist. If a particle fulfills the condition,

$$0 < \frac{v_{\perp}^2}{v^2} < \frac{B}{B_{\max}},$$

it can reach all points on the flux surface and is referred to as *passing*, *circulating* or *untrapped*. On the other hand, ions or electrons satisfying,

$$\frac{B}{B_{\max}} < \frac{v_{\perp}^2}{v^2} \leq \frac{B}{B_{\min}},$$

are reflected at the point where $v_{\perp} = v$ and turn around, i.e. v_{\parallel} necessarily becomes 0 and changes sign. These are *trapped* on the outboard side of the torus. Particles with $\frac{v_{\perp}^2}{v^2} > \frac{B}{B_{\min}}$ cannot exist.

Furthermore, the gradient and curvature of the magnetic background field and also an electric field lead to a drift movement of the gyration centers [10]:

$$\mathbf{v}_D = \frac{\mathbf{E} \times \mathbf{B}}{B^2} + \underbrace{\frac{v_{\perp}^2}{2\Omega} \left(\mathbf{b} \times \frac{\nabla B}{B} \right) + \frac{v_{\parallel}^2}{\Omega} (\mathbf{b} \times (\mathbf{b} \cdot \nabla) \mathbf{b})}_{\mathbf{v}_{\nabla B} + \mathbf{v}_c = \mathbf{v}_d}, \quad (2.7)$$

where we have introduced the magnetic drift velocity \mathbf{v}_d , consisting of ∇B and curvature drift. The electric field must be weak enough to not violate the assumption of a magnetized plasma, i.e. $E/B \ll v_{\perp}$. The consequence of this phenomenon can be seen in Fig. 2.3: The gyration centers follow paths which are closed in the poloidal plane and are called *drift orbits*.

If we consider a circular flux surface with a small inverse aspect ratio $\epsilon \ll 1$ far away from the magnetic axis, a positive ion will always feel an upwards force. A passing

ion starting with $v_{\parallel} > 0$ on the outboard midplane then poloidally prescribes a circular path on the poloidal plane with a slightly bigger diameter than its original flux surface while its (otherwise identical) counterpart with $v_{\parallel} < 0$ will move equivalently with a smaller diameter. This excursion from the flux surface is quite small [9]:

$$\Delta r_c \sim \frac{qv}{\Omega}. \quad (2.8)$$

On the other hand, a trapped ion will undergo a motion whose poloidal projection motivates its iconic name *banana orbit*. Again the sign of v_{\parallel} on the outboard midplane determines the direction of displacement from the original flux surface. The width of this orbit can be estimated as:

$$r_b \sim \epsilon^{1/2} \rho_p = \epsilon^{-1/2} \Delta r_c, \quad (2.9)$$

where ρ_p is the poloidal gyroradius, i.e. the length scale derived from B_p instead of B .

Neoclassical transport

In the same way as gyro-orbits, drift orbits will not cause any transport perpendicular to the magnetic field unless they undergo collisions. Since this provides a stronger transport on top of the classical one, it was termed *neoclassical transport*. The mechanism was first described in Ref. [11]. We can again estimate it by a random walk argument, this time using the banana width $r_b \ll \rho$:

$$D_e \sim \frac{r_b^2}{2\tau_{ei}} \sim \epsilon^{-3/2} q^2 D_{cl}. \quad (2.10)$$

This means for the typical dimensions of a tokamak, neoclassical transport is around two orders of magnitude higher than classical transport. This observation holds equivalently for heat transport. The important underlying assumption here is that the average time to detrap a particle by collisions is much longer than the time to complete a poloidal orbit, estimated by the bounce frequency $\omega_b \sim \sqrt{\epsilon} v_{th}/qR$. This can be quantified with a dimensionless parameter, the collisionality ν_* :

$$\nu_* = \frac{\nu/\epsilon}{\omega_b} = \frac{\nu\epsilon^{-3/2}}{v_{th}/qR}, \quad (2.11)$$

where the particle velocity is estimated by the thermal velocity $v_{th} = \sqrt{2T/m}$. Based on ν_* , we can distinguish three specific transport regimes:

- $\nu_* \ll \epsilon^{3/2}$, the banana regime, which we just described.
- $\epsilon^{3/2} \ll \nu_* \ll 1$, the plateau regime, which only becomes clearly distinguishable for a big aspect ratio.
- $\nu_* \gg 1$, the Pfirsch-Schlüter regime, where the plasma can be described as a fluid and collisions completely disrupt the drift orbits.

We will present different analytical predictions for heat transport in these regimes when we compare them to numerical results in Sec. 4.1.

The assumption of locality, i.e. that particles do not drift away far from their flux surface ($r_b \ll r$), which underlies the standard theory of neoclassical transport in tokamaks, is valid in the majority of the plasma volume, but becomes invalid in the region near the magnetic axis. The radial position where this happens can be straightforwardly defined by setting $r_b = r$, which results in the potato width:

$$r_p = \sqrt[3]{4q^2\rho^2 R_0}. \quad (2.12)$$

As it is obvious from the potato orbit in Fig. 2.3, transport phenomena within this region cannot be described by parameters of a specific flux surface. We will elaborate on these non-local effects in Sec. 4.2.2 together with according numerical simulations.

Bootstrap current

The presence of magnetic drifts also affects the parallel direction: Radial gradients in density and temperature give rise to a parallel current - the *bootstrap current*. If we consider a system with a radial density gradient, we will find that there are more trapped ions with $v_{\parallel} < 0$ than $v_{\parallel} > 0$ on a specific flux surface as their average orbit radius is smaller than the flux surface. Since Eq. (2.7) contains the charge, the opposite holds for electrons resulting in a net parallel current [12]. This flow, however, is only the seed for the bootstrap current which is carried mainly by the circulating particles. Although the trapped population only makes up for a fraction of around $\sqrt{\epsilon}$ of the total density, collisions couple them to the rest and thus transfer the asymmetry in their parallel velocity distribution to the entire population.

The bootstrap current generated this way has been observed in experiments [13] and plays a role in concepts for steady-state operation [14] and advanced confinement scenarios [15] of tokamaks. On the other hand it also drives an instability known as neoclassical tearing mode [16].

2.2.3 Turbulent transport

While the neoclassical theory is able to explain the transport fluxes in some experimental cases, in general its predictions are still by an order of magnitude too small. The observed enhancement of the fluxes is sometimes referred to as anomalous transport, but we will use the term *turbulent transport* based on the underlying physical phenomenon. As this type of turbulence is based on collective states of the plasma, we abandon the concept of single particles at this point and turn to a model more apt to collective behavior.

2.3 The gyrokinetic description

For the desired quantitative predictions of neoclassical and turbulent transport the model of choice is describing each species σ of the plasma in terms of a (six-dimensional)

ensemble-averaged phase space distribution function $f_\sigma(\mathbf{x}, \mathbf{v}, t)$. The time evolution of this function is determined by the kinetic equation:

$$\frac{Df_\sigma}{Dt} = \frac{\partial f_\sigma}{\partial t} + \mathbf{v} \cdot \nabla_{\mathbf{x}} f_\sigma + \frac{\mathbf{F}}{m_\sigma} \cdot \nabla_{\mathbf{v}} f_\sigma = C(f_\sigma), \quad (2.13)$$

where the force field $\mathbf{F} = Ze(\mathbf{E} + \mathbf{v} \times \mathbf{B})$ is determined by the Maxwell equations:

$$\begin{aligned} \nabla \cdot \mathbf{E} &= 4\pi \sum_\sigma Z_\sigma e \int f_\sigma d^3v, \\ \nabla \cdot \mathbf{B} &= 0, \\ \nabla \times \mathbf{E} &= -\frac{1}{c} \frac{\partial \mathbf{B}}{\partial t}, \\ \nabla \times \mathbf{B} &= \frac{4\pi}{c} \sum_\sigma Z_\sigma e \int \mathbf{v} f_\sigma d^3v + \frac{1}{c} \frac{\partial \mathbf{E}}{\partial t}. \end{aligned}$$

The fields \mathbf{E} and \mathbf{B} are macroscopic variables. All microscopic interactions are subsumed in the term $C(f_\sigma)$, which is named collision operator due to the effect it describes. According to the form (see Sec. 2.3.4) of this collision operator Eq. (2.13) is called a Fokker-Planck equation. In the collisionless limit it is named the Vlasov equation.

In principle, it is possible to calculate a numerical solution to this system of equations (see, for example, Ref. [17]). The computational cost is, however, (still) prohibitive for everything beyond very simple systems, especially for the strong magnetic field of a tokamak. Thus it is necessary to make further approximations and adaptations for the equation system, which accommodate to the specifics of a strongly magnetized thin hot plasma of toroidal shape. This leads to the so-called *gyrokinetic* description which we explain briefly in the following section. For a comprehensive review of the subject see Ref. [18].

2.3.1 Gyrokinetic ordering

The fundamental temporal ordering is that any effect we consider happens on time scales that are much longer than the time for a gyration τ_g :

$$\tau_g \ll \tau_b \ll \tau_E,$$

with the bounce time τ_b and the energy confinement time τ_E . The space-scale ordering is expressed with

$$\varepsilon_\perp = |\mathbf{k}_\perp| \rho_i,$$

and we have to distinguish between $\varepsilon_\perp \sim 1$ for turbulent and $\varepsilon_\perp \ll 1$ for neoclassical phenomena.

Additionally, we assume that the distribution function can be split into a small perturbation f_1 and a Maxwellian background F_0 and that the perpendicular electric field fluctuations are small compared to the background magnetic field:

$$\left| \frac{f_1}{F_0} \right| \sim \left| \frac{c\delta E_\perp}{Bv_{th}} \right| \sim \varepsilon_\perp \frac{e\phi_1}{T_i} \sim \varepsilon_\delta. \quad (2.14)$$

The index 1 of ϕ_1 does not imply a direct ordering here, but merely that it is connected to f_1 . An analogous ordering can be introduced for a fluctuating vector potential $A_{1\parallel}$ and magnetic field $B_{1\parallel}$, but this is beyond the scope of this work and thus neglected from here on. This means we restrict this work to the *electrostatic limit* - assuming that the plasma pressure is so low that the fields induced by current fluctuations are negligible compared to the background field.

The scale separation between the ion gyroradius and the length scales of the magnetic field L_B and of the background equilibrium temperature and density gradients L_F allows to define the small parameters:

$$\varepsilon_B = \frac{\rho_i}{L_B} \quad \text{with} \quad \left| \frac{\rho_i \nabla B}{B} \right| \sim \varepsilon_B, \quad (2.15)$$

$$\varepsilon_F = \frac{\rho_i}{L_F} \quad \text{with} \quad \left| \frac{\rho_i \nabla F_0}{F_0} \right| \sim \varepsilon_F. \quad (2.16)$$

The ratio $\varepsilon_B/\varepsilon_F$ is in fact the inverse aspect ratio ϵ and can be used for the small aspect ratio limit in neoclassical theory. For turbulence studies it is usually assumed to be unity. The background changes on a time scale of order ε_B^3 , which is the typical transport time scale.

The last ordering we introduce is based on the strong anisotropy of the plasma dynamics:

$$\varepsilon_{\parallel} = \frac{|k_{\parallel}|}{|\mathbf{k}|} \ll 1.$$

In the derivation of the gyrokinetic Vlasov-Poisson system usually several of these ordering parameters are considered to be of similar magnitude and thus subsumed into one ε .

2.3.2 The guiding-center and gyro-center transformation

The modern form of gyrokinetics is based on using phase space coordinate transformations to reach equations of motion that are independent of the fast gyration time scale [18]. This is a two-step process, first moving to guiding-center coordinates in stationary electromagnetic fields and then to gyro-center coordinates which incorporate the fluctuating fields of a turbulent plasma. For clarity, we drop the species index in equations where it is not necessary.

Guiding-center transformation

The starting point is the single particle Hamiltonian

$$H(\mathbf{x}, \dot{\mathbf{x}}) = \frac{1}{2} m v^2 + Z e \phi(\mathbf{x}) \quad \text{with: } \mathbf{v} = \dot{\mathbf{x}}, \quad (2.17)$$

and the Lagrangian

$$L(\mathbf{x}, \dot{\mathbf{x}}) = \mathbf{p} \dot{\mathbf{x}} - H(\mathbf{x}, \dot{\mathbf{x}}), \quad (2.18)$$

with the canonical momentum $\mathbf{p} = m\mathbf{v} + \frac{Ze}{c}\mathbf{A}(\mathbf{x})$. This can also be expressed by a one-form γ which fulfills

$$\int L dt = \int \gamma.$$

The strong magnetization of the plasma allows to treat the gyration as purely circular and to introduce the transformation to guiding-center coordinates $(\mathbf{X}, v_{\parallel}, \mu, \theta, t)$ with the gyration phase angle θ :

$$\mathbf{x} = \mathbf{X} + \rho(\mathbf{X}, \mu) \mathbf{a}(\theta), \quad (2.19)$$

$$\mathbf{v} = v_{\parallel} \hat{\mathbf{b}}(\mathbf{X}) + v_{\perp}(\mathbf{X}, \mu) \mathbf{c}(\theta). \quad (2.20)$$

The unit vectors \mathbf{a} and \mathbf{c} represent the local radial and tangential directions of the gyro-orbit. If we only consider terms of first order in ε_B , applying this transformation and an average over the gyro-angle (a *gyroaverage*) to the one-form γ yields:

$$\Gamma_0 = \frac{Ze}{c} A_0^*(\mathbf{X}) \cdot d\mathbf{X} + \frac{\mu B(\mathbf{X})}{\Omega(\mathbf{X})} d\theta - H_0(\mathbf{X}, v_{\parallel}, \mu) dt, \quad (2.21)$$

where we have introduced:

$$A_0^* = A_0 + \frac{mc}{Ze} v_{\parallel} \hat{\mathbf{b}}, \quad (2.22)$$

$$H_0(\mathbf{X}, v_{\parallel}, \mu) = \frac{1}{2} m v_{\parallel}^2 + \mu B(\mathbf{X}) + Ze \phi_0(\mathbf{X}). \quad (2.23)$$

The zeroth order electrostatic potential ϕ_0 is associated with plasma rotation and is neglected from here on. The potential arising from neoclassical effects can technically be also considered zeroth order, but we absorb it in ϕ_1 based on the fact that it will be calculated from f_1 . This is justified by the ordering (2.14) where only $\varepsilon_{\perp} \phi_1$ is relevant. The one-form (2.21) is already sufficient to derive the drift-kinetic Vlasov equation, a limit we will discuss in Sec. 2.3.7.

Gyro-center transformation

For the model to cover turbulent transport, on the other hand, the guiding-center form has to be extended to allow short-wavelength and time-dependent perturbations in the electromagnetic potential - in this work limited to electrostatic perturbations. Hence, we extend the particle and guiding-center one-form and the Hamiltonian by $\mathcal{O}(\varepsilon_{\delta})$ contributions:

$$\gamma = \gamma_0 + \gamma_1,$$

$$\Gamma = \Gamma_0 + \Gamma_1,$$

$$H = H_0 + H_1,$$

which are found to be:

$$\gamma_1 = -H_1 dt,$$

$$H_1 = Ze \phi_1(\mathbf{x}, t).$$

When the gyroaverage is applied, it now turns out that the dependency of the one-form and the Hamiltonian on the gyrophase θ cannot be completely removed anymore because ϕ_1 varies on the gyroradius scale. The mathematical tool of choice to

treat this is the *Lie transform*, which is a near-identity coordinate transform and applies to one-forms in the following way:

$$\bar{\Gamma} = T^{*-1}\Gamma + dS,$$

with the gauge function dS . The operator T^{*-1} consists of a number of individual Lie transforms with the generator G in the form of Lie derivatives,

$$[L_G\Gamma](\mathbf{X}) = G^\lambda(\mathbf{X}) \left(\frac{\partial \Gamma_\nu(\mathbf{X})}{\partial X^\lambda} - \frac{\partial \Gamma_\lambda(\mathbf{X})}{\partial X^\nu} \right).$$

The number depends on the desired order of the smallness parameter ε (in this example ε^2):

$$T^{*-1} = e^{-\varepsilon L_1} e^{-\varepsilon^2 L_2} = 1 - \varepsilon L_1 + \varepsilon^2 \left(\frac{1}{2} L_1^2 - L_2 \right) + \mathcal{O}(\varepsilon^3).$$

A detailed description of the choices for G and dS can be found in Ref. [19, 20], we will just give the end result here. The gyro-center one-form resulting from this transformation of the perturbed guiding-center one-form is then found to be:

$$\bar{\Gamma} = \bar{\Gamma}_0 + \bar{\Gamma}_1 = \frac{Ze}{c} A_0^* \cdot d\mathbf{X} + \frac{\mu B}{\Omega} d\theta - \left(\frac{1}{2} m v_\parallel^2 + \mu B + q \bar{\phi}_1 \right) dt. \quad (2.24)$$

2.3.3 The gyrokinetic Vlasov equation

We can insert Eq. (2.24) in the Euler-Lagrange equations,

$$\left(\frac{\partial \bar{\Gamma}_\lambda}{\partial Z^\nu} - \frac{\partial \bar{\Gamma}_\nu}{\partial Z^\lambda} \right) \frac{dZ^\lambda}{dt} = 0 \quad \text{with } \mathbf{Z} = (\mathbf{X}, v_\parallel, \mu),$$

and arrive after some algebra at the equations of motion for the gyrocenters:

$$\begin{aligned} \dot{\mathbf{X}} &= v_\parallel \hat{\mathbf{b}} + \frac{B}{B_\parallel^*} \left(\frac{\mu}{\Omega m} \hat{\mathbf{b}} \times \nabla B + \frac{v_\parallel^2}{\Omega} (\nabla \times \hat{\mathbf{b}})_\perp + \frac{c}{B} \hat{\mathbf{b}} \times \nabla \bar{\phi}_1 \right) \\ &= v_\parallel \hat{\mathbf{b}} + \frac{B}{B_\parallel^*} (v_{\nabla B} + v_c + v_\phi) = v_\parallel \hat{\mathbf{b}} + \frac{B}{B_\parallel^*} v_D, \end{aligned} \quad (2.25)$$

$$\dot{v}_\parallel = -\frac{\dot{\mathbf{X}}}{m v_\parallel} \cdot (\mu \nabla B + Ze \nabla \bar{\phi}_1), \quad (2.26)$$

$$\dot{\mu} = 0 \quad (\text{as a conserved quantity}), \quad (2.27)$$

where we find the magnetic and the $\mathbf{E} \times \mathbf{B}$ drift velocity of Eq. (2.7) again. The parallel component of the generalized magnetic field $B_\parallel^* = B + \frac{B}{\Omega} v_\parallel \hat{\mathbf{b}} \cdot (\nabla \times \hat{\mathbf{b}})$ is kept for the system to fulfill the Liouville theorem [18], eq. B12. The second term is of order ε_B , though.

Inserting the equations of motion into Eq. (2.13) (while ignoring the collision operator for the moment), we arrive at the gyrokinetic Vlasov equation, which gives

the time evolution of the distribution function of the gyrocenters:

$$\frac{\partial F_0 + f_1}{\partial t} + \dot{\mathbf{X}} \cdot \nabla (F_0 + f_1) + v_{\parallel} \frac{\partial (F_0 + f_1)}{\partial v_{\parallel}} = 0 \quad (2.28)$$

$$\begin{aligned} \Rightarrow \frac{\partial f_1}{\partial t} + \left(v_{\parallel} \hat{\mathbf{b}} + \frac{\mu c}{ZeB_{\parallel}^*} \hat{\mathbf{b}} \times \mathbf{B} + \frac{v_{\parallel}^2 c B}{ZeB_{\parallel}^*} (\nabla \times \hat{\mathbf{b}})_{\perp} \right) \cdot \\ \cdot \left(\nabla (F_0 + f_1) - \frac{1}{mv_{\parallel}} \cdot (\mu \nabla B + q \nabla \bar{\phi}_1) \frac{\partial F_0 + f_1}{\partial v_{\parallel}} \right) = 0. \end{aligned} \quad (2.29)$$

If we assume most of the ordering parameters of Sec. 2.3.1 to be of the same magnitude, $\varepsilon_{\delta} \sim \varepsilon_B \sim \varepsilon_F \sim \varepsilon_{\parallel}$, we can separate the terms of this equation according to their order in ε into F_0 and f_1 .

The equilibrium distribution

For the lowest (0-th) order, we find:

$$v_{\parallel} \hat{\mathbf{b}} \cdot \left(\nabla F_0 - \frac{1}{mv_{\parallel}} \mu \nabla B \frac{\partial F_0}{\partial v_{\parallel}} \right) = 0. \quad (2.30)$$

Hence, F_0 is not explicitly evolved in time and we need to choose an equilibrium distribution that fulfills Eq. (2.30) at all times. One way to achieve this is a local Maxwellian for each species in the form:

$$F_{0\sigma}(x, v_{\parallel}, \mu) = \frac{n_{0\sigma}(x)}{\pi^{3/2} v_{\text{th}\sigma}^3(x)} \exp \left(-\frac{m_{\sigma} v_{\parallel}^2 / 2 + \mu B}{T_{0\sigma}(x)} \right), \quad (2.31)$$

where the background temperature and density only depend on the radial coordinate x since they are flux surface quantities.

The first order equation

Introducing the Maxwellian F_0 into the first order equation results in:

$$\begin{aligned} \frac{\partial f_1}{\partial t} + \frac{B}{B_{\parallel}^*} (\mathbf{v}_{\nabla B} + \mathbf{v}_c + \mathbf{v}_{\phi}) \cdot \left(\nabla (F_0 + f_1) + \nabla (\mu B + Ze\bar{\phi}_1) \frac{F_0}{T_0} \right) + \\ + v_{\parallel} \hat{\mathbf{b}} \cdot \left(\nabla f_1 + Ze \nabla \bar{\phi}_1 \frac{F_0}{T_0} - \frac{\mu}{mv_{\parallel}} \nabla B \frac{\partial f_1}{\partial v_{\parallel}} \right) = 0. \end{aligned} \quad (2.32)$$

The curvature drift velocity can be cast in a more convenient form by using Ampère's law and the magnetohydrodynamic equilibrium condition $\nabla p = \mathbf{j} \times \mathbf{B}/c$:

$$\begin{aligned} \frac{\Omega}{v_{\parallel}^2} \mathbf{v}_c &= (\hat{\mathbf{b}} \times (\hat{\mathbf{b}} \cdot \nabla) \hat{\mathbf{b}}) = \left(\nabla \times \frac{\mathbf{B}}{B} \right)_{\perp} = -\hat{\mathbf{b}} \times \left(\hat{\mathbf{b}} \times \left(\frac{4\pi}{cB} \mathbf{j} + \frac{1}{B} \hat{\mathbf{b}} \times \nabla B \right) \right) = \\ &= \hat{\mathbf{b}} \times \left(\frac{\nabla B}{B} + \frac{\beta}{2} \frac{\nabla p}{p} \right) \quad \text{with: } \beta = \frac{8\pi p}{B^2}. \end{aligned}$$

The parameter β is the ratio between the thermodynamic and the magnetic pressure. The electrostatic limit, which we use throughout this theory, implies $\beta \approx 0$.

In Eq. (2.28) we have neglected the right hand side of Eq. (2.13) which describes collisions. Since these are crucial for neoclassical transport (see Sec. 2.2.2), the collision operator will now be discussed in greater detail.

2.3.4 The collision operator

Even if we do not ignore collisions, they are still quite rare events in hot plasmas. For example, the core of fusion devices is typically in the banana regime described in Sec. 2.2.2. Hence, the collision operator can be restricted to binary collisions (including the case $\sigma = \sigma'$):

$$C(f_\sigma) = \sum_{\sigma'} C_{\sigma\sigma'}(f_\sigma, f_{\sigma'}).$$

Due to the long range of the Coulomb force, undergoing a collision changes the velocity of a particle only by a small step. This can be quantified by the parameter $\Lambda = \lambda_D/b_{\min}$, which compares the minimal impact parameter b_{\min} attributed to a 180 degree deflection with the Debye length λ_D as the typical impact parameter. The Coulomb logarithm $\ln \Lambda$ is in the range 15 – 25 for laboratory plasmas, a number of formulas for its value in different parameter regimes can be found in Ref. [21].

As a result we can express the collision operator as a combination of a drag force and a diffusive spreading in velocity space (repeated indices imply summation):

$$C_{\sigma\sigma'}(f_\sigma, f_{\sigma'}) = -\nabla_v \cdot j^{\sigma\sigma'},$$

$$j_k^{\sigma\sigma'} = \frac{\langle \Delta v_k \rangle^{\sigma\sigma'}}{\Delta t} f_\sigma - \frac{\partial}{\partial v_l} \left(\frac{\langle \Delta v_k \Delta v_l \rangle^{\sigma\sigma'}}{2\Delta t} f_\sigma \right),$$

where it is necessary to derive the expectation values $\langle \cdot \rangle / \Delta t$ from the collision dynamics. The original derivation by Landau can be found in Ref. [22] and a concise description appears, for example, in Ref. [9]. Here we only provide the final result:

$$C_{\sigma\sigma'}(f_a, f_b) = 4\pi \ln \Lambda \left(\frac{Z_\sigma Z_{\sigma'} e^2}{m_\sigma} \right)^2 \frac{\partial}{\partial v_k} \left(\frac{m_\sigma}{m_{\sigma'}} \frac{\partial \varphi_{\sigma'}}{\partial v_k} f_\sigma - \frac{\partial^2 \psi_{\sigma'}}{\partial v_k \partial v_l} \frac{\partial f_\sigma}{\partial v_l} \right), \quad (2.33)$$

with the *Rosenbluth potentials* [23]:

$$\varphi_{\sigma'}(v) = - \int \frac{1}{u} f_{\sigma'}(v') d^3 v', \quad \psi_{\sigma'}(v) = - \frac{1}{2} \int u f_{\sigma'}(v') d^3 v' \quad \text{where: } u = |v - v'|. \quad (2.34)$$

It can be easily shown that this collision operator fulfills a number of conservation laws:

$$\int C_{\sigma\sigma'}(f_\sigma, f_{\sigma'}) d^3 v = 0, \quad (2.35)$$

$$\int m_\sigma v C_{\sigma\sigma'}(f_\sigma, f_{\sigma'}) d^3 v = - \int m_{\sigma'} v C_{\sigma'\sigma}(f_{\sigma'}, f_\sigma) d^3 v, \quad (2.36)$$

$$\int \frac{m_\sigma v^2}{2} C_{\sigma\sigma'}(f_\sigma, f_{\sigma'}) d^3 v = - \int \frac{m_{\sigma'} v^2}{2} C_{\sigma'\sigma}(f_{\sigma'}, f_\sigma) d^3 v, \quad (2.37)$$

representing conservation of particles, momentum and energy. The operator is also Galilean invariant, since only relative velocities and derivatives of v appear. Lastly, if the operator is applied to two Maxwellian distributions with equal temperature, it vanishes.

Linearization and Maxwellian background

As the next step, we now apply the splitting of the distribution function from Sec. 2.3.3 to $C_{\sigma\sigma'}$, which yields:

$$C_{\sigma\sigma'} = C(F_{0\sigma}, F_{0\sigma'}) + \underbrace{C(f_{1\sigma}, F_{0\sigma'}) + C(F_{0\sigma}, f_{1\sigma'})}_{C_{\sigma\sigma'}^L} + \underbrace{C(f_{1\sigma}, f_{1\sigma'})}_{C_{\sigma\sigma'}^{\text{NL}}}.$$

The first term vanishes for self-collisions or species with equal temperatures. Otherwise, it represents thermalization between two species. Since we do not consider the slow evolution of the background distribution in the Vlasov equation, this term is simply neglected. Hence, Eq. (2.30) and the choice of F_0 remain valid in the presence of collisions. The term C^{NL} is second order in ε and is thus also not considered. The remaining terms constitute the *linearized Landau-Boltzmann operator*, where the first term is often called test-particle and the second one field-particle operator.

For the test-particle part it can be shown that the derivatives of the Rosenbluth potentials evaluate to:

$$\begin{aligned} \frac{d\varphi_{\sigma'}(x_{\sigma'})}{dv} &= -\frac{n_{\sigma'}}{v_{\text{th}\sigma'}^2 x_{\sigma'}^2} (\text{erf}(x_{\sigma'}) - x_{\sigma'} \text{erf}'(x_{\sigma'})), \\ \frac{d\psi_{\sigma'}(x_{\sigma'})}{dv} &= -\frac{n_{\sigma'}}{2} \left(\text{erf}(x_{\sigma'}) - \frac{\text{erf}(x_{\sigma'}) - x_{\sigma'} \text{erf}'(x_{\sigma'})}{2x_{\sigma'}^2} \right), \end{aligned}$$

with $x = v/v_{\text{th}\sigma'}$, $\text{erf}(x)$ the error function and $\text{erf}' = d\text{erf}/dx$. If inserted into Eq. (2.33) this gives the final result for the test particle operator. An explicit expression and more detailed derivations can be found, for example, in Ref. [24]. The prefactors of the collision operator can be combined to define a basic collision frequency and time⁴:

$$\underline{\nu}_{\sigma\sigma'} = \frac{4\pi n_{\sigma'} Z_{\sigma}^2 Z_{\sigma'}^2 e^4 \ln \Lambda}{m_{\sigma}^2 v_{\text{th}\sigma}^3}, \quad \tau_{\sigma\sigma'} = \frac{3\sqrt{\pi}}{4\underline{\nu}_{\sigma\sigma'}}. \quad (2.38)$$

The field part of the linearized collision operator poses a more complex problem. Although it is possible to compute the Rosenbluth potentials for the perturbed distribution function, usually an ad-hoc model which has the conservation properties (2.35)-(2.37) is sufficient. Details how this is accomplished can be found in Ref. [24] and references given therein. Care must also be taken so that the model conserves the property of self-adjointness of the general linearized collision operator, i.e. that the functional

$$S[\hat{f}, \hat{g}] = \int \hat{g}(v) C_{\sigma\sigma}^L(F_{0\sigma}, \hat{f}) d^3v,$$

⁴This is the definition from Ref. [9]. The definitions for ν and $\tau_{\sigma\sigma'}$ tend to vary in the constants and the definition of v_{th} (see Appendix A).

is symmetric in its arguments. Physically, this implies that collisions must have a positive entropy production rate.

Finally, the collision operator must be transformed from particle space to the gyro-center space of Eq. (2.32). By representing the guiding center coordinate transformation with the push-forward operator

$$T_{(\text{gc})}^{-1} : f \rightarrow f^{(\text{gc})} = T_{(\text{gc})}^{-1} f,$$

and the inverse transformation with the pull-back operator

$$T_{(\text{gc})} : f^{(\text{gc})} \rightarrow f = T_{(\text{gc})} f^{(\text{gc})},$$

we can formally write:

$$C_{\sigma\sigma'}^{(\text{gc})}(f_{\sigma}^{(\text{gc})}) = T_{(\text{gc})}^{-1} C_{\sigma\sigma'}(T_{(\text{gc})} f_{\sigma}^{(\text{gc})}). \quad (2.39)$$

In principle, this operator still has a gyro-angle dependence, since the guiding center transformation is only constructed to remove it from the Vlasov part of the kinetic equation. However, the smallness of the collision frequency justifies to only consider the gyro-angle independent part. Furthermore, the guiding center distribution function can be approximately replaced by its gyro-center counterpart.

2.3.5 Field aligned coordinates

In order to fully use the smallness of the ordering parameter ε_{\parallel} it is sensible to rewrite the vector expressions of the Fokker-Planck equation in terms of their components. While the toroidal-poloidal-radial coordinate system of Sec. 2.1 is very intuitive, field aligned coordinates are a better suited choice for this. Introductions to the topic can be found in Ref. [25, 26]. We use so-called Clebsch coordinates, where the magnetic field is:

$$\mathbf{B} = C \nabla x \times \nabla y.$$

The constant C only depends on the radial position, the labels x, y and z represent the radial, binormal and the parallel direction. In this formulation the parallel derivative becomes:

$$\hat{\mathbf{b}} \cdot \nabla = \frac{1}{\sqrt{g_{zz}}} \frac{\partial}{\partial z} = \frac{C}{JB} \frac{\partial}{\partial z},$$

and the triple products appearing in terms with the drift velocity turn into:

$$\hat{\mathbf{b}} \times \nabla \mathcal{A} \cdot \nabla \mathcal{B} = \frac{g_{kz}}{J \sqrt{g_{zz}}} \partial_i \mathcal{A} \partial_j \mathcal{B} \epsilon^{ijk} = \frac{C}{J^2 B} g_{kz} \partial_i \mathcal{A} \partial_j \mathcal{B} \epsilon^{ijk},$$

for arbitrary scalar fields \mathcal{A}, \mathcal{B} . $J = \sqrt{\det(g_{ij})}$ is the determinant of the Jacobian associated with the covariant metric coefficients $g_{ij} = \mathbf{e}_i \cdot \mathbf{e}_j$.

Applying these expressions to Eq. (2.32) (and adding the collision operator) allows now to identify terms smaller by order ε_{\parallel} and yields the final form of the first-order

Fokker-Planck equation:

$$\begin{aligned}
 \frac{\partial f_1}{\partial t} = & \frac{c}{C} \frac{B}{B_{\parallel}^*} \partial_y \bar{\phi}_1 \partial_x^{n,T} F_0 - \frac{c}{C} \frac{B}{B_{\parallel}^*} (\partial_x \bar{\phi}_1 \Gamma_y - \partial_y \bar{\phi}_1 \Gamma_x) + \\
 & + \frac{c}{C} \frac{B}{B_{\parallel}^*} \cdot \frac{\mu B + m v_{\parallel}^2}{Z e B} (K_x \Gamma_x - K_y \Gamma_y) - \frac{C}{J B} v_{\parallel} \Gamma_z + \\
 & + \frac{C}{J B} \frac{\mu}{m} \partial_z B \frac{\partial f_1}{\partial v_{\parallel}} + \frac{c}{C} \frac{B}{B_{\parallel}^*} \cdot \frac{\mu B + m v_{\parallel}^2}{Z e B} K_x \partial_x^{n,T} F_0 + C^L(f_1),
 \end{aligned} \tag{2.40}$$

which contains the following abbreviations:

$$\begin{aligned}
 \Gamma &= \nabla f_1 + Z e \frac{F_0}{T_0} \nabla \bar{\phi}_1, \\
 K_x &= \left(\partial_y B - \frac{g_{yz}}{g_{zz}} \partial_z B \right), \\
 K_y &= \left(\partial_x B - \frac{g_{xz}}{g_{zz}} \partial_z B \right), \\
 \partial_x^{n,T} F_0 &= \partial_x F_0 + \frac{\mu}{T_0} F_0 \partial_x B.
 \end{aligned}$$

This equation is already very close to the form used in the GENE code for numerical solving.

2.3.6 The Poisson equation

The remaining task for solving the gyrokinetic equations of motion is to evaluate the self-consistently generated electric field. As previously stated, we neglect fluctuations of the vector potential A . Based on Maxwell's equations, the electrostatic potential is determined by the Poisson equation:

$$-\nabla^2 \phi = 4\pi e \sum_{\sigma} Z_{\sigma} n_{\sigma}(\mathbf{x}), \tag{2.41}$$

where the density is now defined as the lowest order fluid moment of the particle distribution function:

$$n_{\sigma} = \int f_{\sigma}(\mathbf{x}, \mathbf{v}) d^3 v.$$

Since the equilibrium is assumed to be quasineutral, only field perturbations are explicitly calculated by this equation.

As for collisions, we have to express the particle distribution function in terms of the gyro-center distribution. This can again be written in terms of a pull-back operator, which now represents the *gyrocenter* transformation. For the first order perturbation it takes the form:

$$T^* f_{1\sigma}^{(\text{gy})} = f_{1\sigma}^{(\text{gy})} - e Z_{\sigma} \bar{\phi}_1 \frac{F_{0\sigma}}{T_{0\sigma}}, \tag{2.42}$$

where $\tilde{\phi}_1 = \phi_1 - \bar{\phi}_1$ denotes the gyro-angle dependent part of the potential in particle space. We can use this operation to calculate the fluid moments in terms of the gyro-center distribution function ($B_{||}^* \approx B$ from here on):

$$\begin{aligned} M^{ab} &= \frac{1}{m} \int \delta(X - \mathbf{x} + \boldsymbol{\rho}) T^* f_1(X, v_{||}, \mu) B v_{||}^a v_{\perp}^b d^3X dv_{||} d\mu d\theta \\ &= \frac{1}{m} \int \delta(X - \mathbf{x} + \boldsymbol{\rho}) \left(f_1(X, v_{||}, \mu) - \tilde{\phi}_1 \frac{F_0}{T_0} \right) B v_{||}^a v_{\perp}^b d^3X dv_{||} d\mu d\theta. \end{aligned} \quad (2.43)$$

Inserting $n(\mathbf{x}) = M_{00}(\mathbf{x})$ into Eq. (2.41) and moving all terms involving ϕ_1 to the left hand side then results in:

$$\begin{aligned} \nabla_{\perp}^2 \phi_1 - 8\pi^2 \sum_{\sigma} \frac{Z_{\sigma}^2 e^2}{m_{\sigma}} \int \left(\phi_1 B \frac{F_{0\sigma}}{T_{0\sigma}} - \left\langle \left\{ B \tilde{\phi}_{1\sigma} \frac{F_{0\sigma}}{T_{0\sigma}} \right\}_{x-\boldsymbol{\rho}} \right\rangle_{\text{gy}} \right) dv_{||} d\mu = \\ = -8\pi^2 \sum_{\sigma} \frac{Z_{\sigma} e}{m_{\sigma}} \int \langle \{ B f_{1\sigma} \}_{x-\boldsymbol{\rho}} \rangle_{\text{gy}} dv_{||} d\mu, \end{aligned} \quad (2.44)$$

where $\langle \dots \rangle_{\text{gy}}$ denotes a gyroaverage and $\{ \dots \}_{x-\boldsymbol{\rho}}$ implies that the content of the curled brackets is evaluated at the position $\mathbf{x} - \boldsymbol{\rho}$. Notably, this means that the Poisson equation contains two different gyroaverages: $\overline{\dots}$ is evaluated at the guiding center position, $\langle \dots \rangle_{\text{gy}}$ at the particle position. It can also be shown that the first term of Eq. (2.44) is small compared to the rest by a factor of the squared Debye length (see Sec. 3.3). Thus it can be neglected.

The left hand side of Eq. (2.44) can be considered as an operator which has to be inverted to calculate ϕ_1 from f_1 .

Adiabatic electrons

For a number of problems (such as those studied in this work) it is adequate to consider the electrons massless and thus infinitely fast along the magnetic field. This considerably reduces the complexity of the gyrokinetic Vlasov-Poisson system: The electron distribution function is not explicitly advanced as the perturbed density becomes:

$$\frac{n_{1e}}{n_{0e}} = \frac{e}{T_{0e}} (\phi_1 - \langle \phi_1 \rangle),$$

where $\langle \dots \rangle$ is the flux surface average (see Sec. 2.1). The simplified Poisson equation then is:

$$\begin{aligned} - \sum_{\sigma \neq e} \frac{m_e}{m_{\sigma}} Z_{\sigma}^2 e^2 \int \left(\phi_1 \left\langle \left\{ B \frac{F_{0\sigma}}{T_{0\sigma}} \right\}_{x-\boldsymbol{\rho}} \right\rangle_{\text{gy}} - \left\langle \left\{ B \tilde{\phi}_{1\sigma} \frac{F_{0\sigma}}{T_{0\sigma}} \right\}_{x-\boldsymbol{\rho}} \right\rangle_{\text{gy}} \right) dv_{||} d\mu = \\ = B e^2 \frac{n_{0e}}{T_{0e}} (\phi_1 - \langle \phi_1 \rangle) - \sum_{\sigma \neq e} \frac{m_e}{m_{\sigma}} Z_{\sigma} e \int \langle \{ B f_{1\sigma} \}_{x-\boldsymbol{\rho}} \rangle_{\text{gy}} dv_{||} d\mu. \end{aligned}$$

2.3.7 The drift-kinetic limit

We have now established the theoretical framework to describe and numerically simulate plasma microturbulence. As it turns out, this model also contains the neoclassical transport problem as a subset. The *drift-kinetic equation*, which has to be solved to calculate neoclassical transport coefficients [11, 27, 28], can be derived from the guiding-center Lagrangian. This means we allow the electrostatic potential, and in consequence the distribution function, to vary spatially only on the scale of the background ($\varepsilon_\perp \ll 1$, see Sec. 2.3.1) and specifically is assumed constant over the width of a gyro-orbit.

This has implications on the advection term $\mathbf{v}_d \cdot \nabla f_1$: The magnetic drift part is ordered as:

$$\mathbf{v}_d \cdot \nabla f_1 \sim \varepsilon_\delta \cdot \frac{\varepsilon_\perp}{\varepsilon_\delta} \cdot \varepsilon_\delta \sim \begin{cases} O(\varepsilon_\delta) & \text{for gyrokinetics (turbulence).} \\ O(\varepsilon_\delta^2) & \text{for drift-kinetics (neoclassical).} \end{cases}$$

Here, the ordering $\mathbf{v}_d \sim \varepsilon_F \sim \varepsilon_\delta$ implies that the banana orbits are narrow and do not deviate far from a flux surface so that the background quantities do not change across an orbit width. Since this assumption does not hold in the potato region near the magnetic axis (see Sec. 2.2.2 and 4.2.2) or in a region with very steep temperature/density gradient, this term provides insight into neoclassical effects beyond the standard theory.⁵

The $\mathbf{E} \times \mathbf{B}$ component of the drift on the other hand is consistently $O(\varepsilon_\delta)$ for both phenomena: The electric field associated with turbulent fluctuations has short-wavelength low-amplitude potential variations, while the neoclassical radial electric field varies over the background scale with a corresponding amplitude.

The first order drift-kinetic equation formally looks like Eq. (2.32) with $\bar{\phi}_1 = \phi_1$. If we write it in components, however, the axisymmetry of neoclassical transport in a tokamak can be used and the derivatives in the binormal direction can be neglected. Eq. (2.40) then takes the form (setting $B_\parallel^* \approx B$):

$$\begin{aligned} \frac{\partial f_1}{\partial t} = & \frac{c}{C} \frac{\mu B + m v_\parallel^2}{ZeB} K_x \left(\partial_x f_1 + Ze \frac{F_0}{T_0} \partial_x \phi_1 \right) - \frac{C}{JB} v_\parallel \Gamma_z + \\ & + \frac{C}{JB} \frac{\mu}{m} \partial_z B \frac{\partial f_1}{\partial v_\parallel} + \frac{c}{C} \frac{\mu B + m v_\parallel^2}{ZeB} K_x \partial_x^{n,T} F_0 + C^L(f_1). \end{aligned} \quad (2.45)$$

If we now enforce the neoclassical ordering and consider only narrow orbits with constant background gradients, f_1 will also not depend on the radial position within the narrow sheet of plasma. Additionally, the Poisson equation for this case reduces to a trivial expression that is fulfilled regardless of ϕ . This reflects the fact that the lowest order neoclassical fluxes are automatically ambipolar in this limit (see Sec. 3.5.2). The

⁵It has been argued that this term should be part of a second order equation involving the nonlinear part of the collision operator [29]. C^{NL} , however, is always $O(\varepsilon_\delta^2)$.

drift-kinetic equation of the standard neoclassical theory is thus:

$$\frac{\partial f_1}{\partial t} + v_{\parallel} \hat{\mathbf{b}} \cdot \left(\nabla f_1 - \frac{\mu}{mv_{\parallel}} \nabla B \frac{\partial f_1}{\partial v_{\parallel}} \right) + \mathbf{v}_d \cdot \nabla^{n,T} F_0 = C^L(f_1), \quad (2.46)$$

$$\frac{\partial f_1}{\partial t} = -\frac{C}{JB} v_{\parallel} \partial_z f_1 + \frac{C}{JB} \frac{\mu}{m} \partial_z B \frac{\partial f_1}{\partial v_{\parallel}} + \frac{c}{C} \frac{B}{B_{\parallel}^*} \cdot \frac{\mu B + mv_{\parallel}^2}{ZeB} K_x \partial_x^{n,T} F_0 + C^L(f_1). \quad (2.47)$$

This equation can be found in basically all works on the topic [9, 28, 30], usually without the $\partial_{v_{\parallel}}$ term (the so-called magnetic mirror term) when the parallel derivative is taken at constant energy instead of v_{\parallel} .

2.4 Summary

In this chapter the physical phenomena leading to collisional (classical and neoclassical) transport in a plasma were described and the gyrokinetic equations that make quantitative numerical predictions of turbulent and neoclassical transport possible were formally derived. The equations were taken in the limit without electromagnetic fluctuations and special attention was paid to the collision operator as it is crucial for correctly modeling neoclassical effects. The Poisson equation was also given for the frequently applied limit of massless (adiabatic) electrons. Finally, the connection to the simpler drift-kinetic equation was shown which in its local limit is the basis for standard neoclassical transport theory.

In the next chapter the cornerstones of the numerical schemes to solve these equations with the GENE code will be presented.

Chapter 3

Numerical implementation of the gyrokinetic equation

In even remotely physically realistic scenarios the nonlinear gyrokinetic Vlasov-Poisson system⁶ presented in the previous chapter is only solvable by numerical methods. One of the codes that implements this is GENE which has been developed at IPP since 1999 [24, 26, 31, 32, 33].

This chapter will give an overview of the numerical schemes used by GENE and elucidate in detail key elements and the features that are relevant for this work. This includes the classification of GENE as a δf code that can use the flux-tube and the global approach for its simulation domain, the choice of the coordinate system and boundary conditions and the normalization to make quantities dimensionless. In addition a scheme is presented to allow the background temperature and densities to evolve self-consistently in global simulations. Lastly, the calculation of the cross-field transport from the phase-space distribution function is shown and ways to calculate a statistically sound uncertainty estimate for them are discussed.

3.1 Local and global simulations

For the numerical realization of the gyrokinetic Vlasov-Poisson system as we have presented it in the last chapter there are two distinct approaches with regard especially to how the device geometry is reflected in the boundary conditions.

In the core of sufficiently large devices, such as JET, ASDEX-Upgrade or DIII-D and the future ITER, the perpendicular size of turbulent structures is so small compared to the characteristic system size that it is justified to do *local* simulations. This means that the values of the profiles at a single radial position are taken as constant over the entire simulation domain. First order derivatives, however, are still retained under the assumption that they do not change their base values significantly across the considered plasma region. Consequently, the boundary conditions for the perpendicular directions x and y can be set as periodic enforcing fixed background gradients. If the simulation

⁶Strictly speaking, it should be named the Fokker-Planck-Poisson system, but most works also call the collisional kinetic equation Vlasov equation.

domain size is chosen to be many times the turbulent correlation length, this will introduce no significant artificial effects. The benefit is that the equation system can be solved by applying spectral methods, which are very accurate and efficient to calculate the various derivatives and operators in the system. An interesting feature of the local model is that neoclassical effects exclusively exist on the $(k_x, k_y) = (0, 0)$ Fourier mode of the distribution function and thus completely decouple from the turbulent fluctuations. This means that the two phenomena can be treated separately even with different numerical codes.

The *non-local* or *global* approach, on the other hand, is required if background quantities vary across the scale of the turbulence. This can be the case for smaller tokamaks (e.g. TCV, Alcator C-Mod) or for transport barriers in larger machines, where the relevant background scale is the steep and quickly varying gradient length. Here, it is no longer justified to use periodic boundary conditions in the radial direction requiring an algorithm on a real space grid, while periodicity (and the spectral solution methods) can be kept in y thanks to the axisymmetry of the problem. A large stellarator requires the opposite: Its magnetic geometry varies strongly in the y direction, while locality can be assumed in x . Comprehensive modeling of small stellarators might even require a "fully" global model. We use global from here on to refer to a radially global model. Giving up the strong radial scale separation also implies that neoclassical and turbulent effects can no longer be analytically separated, motivating the investigations in this thesis. A step further in this concept is to not employ the splitting of the distribution function into background and perturbation when deriving the gyrokinetic Vlasov-Poisson system. Numerical approaches based on this method are called *full-f* codes. A particular feature of them is that neoclassical effects are inextricably included in them. In contrast, a code using the splitting is called δf -code.

Even though the global model is more physically comprehensive, local simulations are still of much value, as they are far less numerically demanding and allow to test phenomena separately and systematically in a less complex environment.

3.2 Numerical approach in GENE

GENE is a so-called *Eulerian* δf code, which means that the perturbation of the distribution function f_1 is discretized on a fixed phase space grid. Another common approach are particle-in-cell methods, which track particles in a Lagrangian framework.

GENE employs the method of lines, which treats spatial and temporal derivatives separately when solving a partial differential equation.

The gyrokinetic equation can be schematically written as:

$$\partial_t f_1 = L f_1 + \mathcal{N}[f_1] + Z_0 \quad (3.1)$$

where terms linear in f_1 are summarized in $L f_1$, $\mathcal{N}[f_1]$ represents the nonlinear part (the second term in Eq. (3.4)) and Z_0 only depends on the background F_0 . The right hand side is evaluated on the phase space mesh and the resulting ordinary differential equation system is then advanced in time with an explicit fourth order Runge-Kutta scheme. Over the development timespan of GENE numerous optimizations have been implemented to both of these steps, e.g. spatial differentiation schemes that conserve

properties of the analytic equation [34] or means for the optimal time step size in the Runge-Kutta scheme [35]. As a result simulations can be efficiently parallelized on up to tens of thousands of processors [36], allowing for the studies in this work, which include both fast turbulent as well as slow collisional time scales.

The algebraic solver for neoclassical equilibria

For the purely neoclassical (drift-kinetic) problem, it is possible to employ another method. While turbulence only reaches a steady state in a time-averaged sense, the neoclassical equilibrium is characterized by $\partial_t f_1 = 0$. This means the steady state fulfills the algebraic equation:

$$L f_1 = -Z_0.$$

In its discrete form this equation is a linear system that can be solved directly or iteratively. For this purpose GENE uses an iterative solver via an interface to the PETSc library. This method has the advantage that it can be tremendously faster than the explicit time stepping scheme for small grid sizes. Unfortunately, while the initial value computation has a complexity of $O(N)$ (N being the number of grid points) for each time step, the algebraic solver scales with $O(N^2)$ per iteration. The number of necessary steps/iterations on the other hand can depend on several parameters: A long collision time slows convergence for the initial value problem, because it requires to cover multiple τ_{ii} , but makes the linear system more sparse favoring the iterative solver. The baseline, however, is that the latter is better for local simulations, while explicit time evolution suits global problems better: The number of points in x increases from 1 to between 150 and 500. The initial value solver has the additional advantage that it yields salvageable results even if it does not reach the fully steady state.

3.2.1 Coordinate choice and boundary conditions

At this point, we have to remember that our physical model is not determined by the Vlasov-Poisson partial differential equations alone - we are, in fact, looking for the solution of a boundary value problem. Hence, care needs to be taken that the numerical boundary conditions in phase space correctly represent the physical ones. To sensibly do this, we also need to define which of the directions in a tokamak (see Sec. 2.1) our so far abstract curvilinear coordinates x, y, z represent.

Field line label(y)

The field line label is sometimes also called binormal direction although strictly speaking this term implies an orthogonal coordinate system. It is defined as:

$$y = C_y(q(\rho)\theta - \varphi),$$

where φ is the toroidal angle, q the safety factor profile and θ is the straight field line angle, i.e. it is chosen so that the field lines appear as straight lines in the $y - z$ plane. The constant $C_y = \rho_0/q_0$ is a constant length factor determined by the reference position $\rho_0 = x_0$. The y direction is represented in Fourier space for both local and global GENE simulations.

The boundary condition in y can be derived in a straightforward way from the physical periodicity:

$$\begin{aligned} f(\rho, \varphi, \theta) &= f(\rho, \varphi + 2\pi, \theta) \\ \Rightarrow f(x, y, z) &= f(x, y - 2\pi C_y, z). \end{aligned}$$

Hence, the simulation domain in y has periodic boundaries if its length is chosen as $L_y = 2\pi C_y$. If the turbulent correlation length is considerably smaller than a full toroidal turn, as is usually the case, it is enough to limit L_y to only an integer fraction of a full toroidal turn:

$$L_y = \frac{2\pi x_0}{n_0 q_0}.$$

The lowest nonzero wavenumber in the simulation is then $k_{y,\min} = n_0/C_y$ and we write $k_y = j k_{y,\min}$, $j \geq 0$. Neoclassical effects do not depend on y in a tokamak, hence they are part of exclusively the $k_y = 0$ Fourier mode.

Radial direction(x)

As its name suggests, x is a flux surface label. A common convention is to define:

$$x = \rho = \sqrt{\psi},$$

where ψ is either the poloidal or toroidal flux function. For our simple model with concentric circular flux surfaces it is valid to write $x = r$ (r being the local minor radius). Details of the ad-hoc geometry with circular concentric flux surfaces we use throughout this entire work can be found in Ref. [37].

The boundary conditions for the radial direction depend on which model of Sec. 3.1 is chosen: Local simulations have periodic boundaries in x and the direction is treated in Fourier space. Global simulations on the other hand offer primarily the choice between Dirichlet and von Neumann boundaries⁷. The former is a sane choice for the outer boundary (i.e. at big x) because it represents assuming a fixed temperature at the edge of the plasma. The inner boundary is less straightforward. Since the field-aligned coordinate system becomes singular at the magnetic axis, the simulation domain has to end at least a gyroradius away from it. The plasma itself has no physical edge there, so choosing a Dirichlet boundary can produce numerical artifacts. As we will show in Sec. 4.2.1, a von Neumann boundary for the $k_y = 0$ mode is the superior choice there for long range neoclassical effects, while the short-wavelength turbulence is only minimally affected by the Dirichlet boundary condition.

Additional problems can arise when the perturbation f_1 (or in a less harmful form its radial derivative) has still finite values at grid points next to the radial boundary. In this case the finite difference scheme tends to produce numerical oscillations (“zigzag”) that can over time reach large amplitudes and spread into the rest of the domain. GENE can prevent this by adding a Krook damping term of the form

$$S_b = -\kappa_b(x) f_1$$

⁷Specifically, we refer to setting f_1 or its derivative to *zero*. Other boundaries are in principle an option if it is clear what they would represent in a physical system.

to the gyrokinetic equation. $\kappa_b(x)$ is typically fourth-order polynomial decaying to zero within an adjustable distance to the boundary. While this is an excellent choice for Dirichlet boundary conditions, it is not compatible with a von Neumann boundary, which would be simply converted to Dirichlet by the damping. It can be a good choice to damp modes with finite k_y in this case, though.

Parallel direction (z)

The direction along the field line is chosen to be $z = \theta$. Its boundary condition is based on the poloidal periodicity of the system:

$$f(\rho, \varphi, \theta) = f(\rho, \varphi, \theta + 2\pi).$$

This affects also the y coordinate, leading to:

$$f(x, y, z) = f\left(x, y + 2\pi q(x) \frac{n_0}{k_{y,\min}}, z + 2\pi\right),$$

which in Fourier space for y takes the form:

$$f(x, k_y, z) = f(x, k_y, z + 2\pi) e^{2\pi i j n_0 q(x)}.$$

This form of the parallel boundary condition is sufficient for global simulations. It, however, requires further adaption to also satisfy the periodicity in x for the local model. The safety factor $q(x)$ is expanded to first order around x_0 :

$$q(x) = q_0 + (x - x_0) \frac{\partial q}{\partial x} = q_0 \left(1 + \frac{x - x_0}{x_0} \hat{s}\right),$$

and we can write:

$$\sum_{k_x, k_y} f(k_x, k_y, z) e^{i k_x x} = \sum_{k_x, j} f(k_x, j k_{y,\min}, z + 2\pi) e^{i k_x x} e^{2\pi i j n_0 q_0} e^{2\pi i j n_0 \hat{s} (x - x_0) / C_y}.$$

Thus, under the assumption $C_y = x_0/q_0$, the parallel boundary condition couples the k_x and k_y grid in the form that

$$k'_x = k_x + 2\pi \hat{s} k_y$$

has to be a wave number present in the system. The minimal (finite) radial wavenumber is consequently:

$$k_{x,\min} = \frac{2\pi \hat{s} k_{y,\min}}{\mathcal{N}} \quad \text{with: } \mathcal{N} = \frac{2\pi \hat{s} L_x}{L_y}.$$

When the number of k_x modes given by the grid is reached, the physical parallel boundary condition can no longer be sustained and field or distribution function components with higher k_x are simply set to zero in GENE.

Velocity space (v_{\parallel}, μ)

Since we assume f_1 to be small compared to F_0 , the total distribution function is approximately Maxwellian and therefore has to exponentially decay with increasing velocity. If the simulation domain is big enough, it is thus justified to use Dirichlet boundary conditions for v_{\parallel} in the non-collisional part. The magnetic moment μ is a parameter for the non-collisional part and thus no boundary condition for it is required. The collision operator uses a finite volume discretization scheme that assumes vanishing fluxes at the μ and v_{\parallel} boundaries.

3.2.2 Discretization schemes

GENE employs a number of different schemes to discretize the derivatives in the gyrokinetic equations. In the case of periodic boundaries (y and in local simulations x) they become mere multiplications in Fourier space with machine precision. The other directions, however, require different schemes. In our case these are fourth order centered finite differences of the form

$$\partial f_i = \frac{1}{12\Delta} (f_{i-2} - 8f_{i-1} + 8f_{i+1} - f_{i+2}).$$

The index i represents a position in one of the grid directions and Δ is the constant grid spacing. Centered finite differences are non-dissipative but dispersive, which means the occurrence of sub-grid oscillations originating from the boundary must be suppressed by numerical *hyperdiffusion*. Details on this can be found in Ref. [32]. The role of v_{\parallel} hyperdiffusion is also fulfilled by collisions and vice versa (in a rather crude way). This means that its amplitude can and has to be chosen low in collisional simulations.

An alternative differencing scheme is motivated by recasting the gyrokinetic equation so that the parallel advection and the nonlinear term take the form of two-dimensional Poisson brackets

$$\{F, G\}_{v_{\parallel}, z} = \frac{\partial F}{\partial v_{\parallel}} \frac{\partial G}{\partial z} - \frac{\partial F}{\partial z} \frac{\partial G}{\partial v_{\parallel}}.$$

In order to numerically conserve the mathematical properties of this bracket an Arakawa scheme [34] can be used. This is important for applications which rely on the exact conservation of constants of motion such as studies of turbulent energetics, but is generally not harmful, so it is nowadays the standard choice for the nonlinearity in GENE. Its use in the parallel advection term leads to a notably higher computational cost (directly and by increased grid point number requirements) leading to a bad cost-benefit ratio for expensive global simulations. Hence, the simulations in Chapter 6 do not employ it for the parallel advection.

The discretization of the collision operator employs a different scheme: It uses a finite volume method after writing C as the divergence of a flux analogously to Eq. (2.3.4). The details of this procedure are described in Ref. [24]. A convenient property of this scheme is the conservation of density. It, however, does not fully preserve the self-adjointness property (2.3.4).

The last important part of the numerical discretization schemes is the implementation of the gyrophase average. Here the application of the integral operator $\mathcal{G}f = \frac{1}{2\pi} \int_0^{2\pi} f d\theta$ becomes a matrix-vector multiplication. Its derivation can be found in Ref. [19] including the local case, where \mathcal{G} becomes the scalar Bessel function $J_0(k_\perp \rho)$.

This concludes the overview over the numeric representations of elements of the gyrokinetic Vlasov-Poisson system. But in order to make predictions from global simulations we need to introduce a number of additional terms that are not originally part of the equations.

3.3 Normalization

A final preparatory step for the implementation of any physical model as a numerical problem is to make all quantities dimensionless with the benefit that all normalized variables in the calculations are kept at roughly order unity. This generally improves the stability of the numerical schemes. Normalization can be performed by defining appropriate reference values, which were originally defined in Ref. [38] and extended for global simulations in Ref. [19]. Obviously, it is easy to reintroduce units in the post-processing to compare, for example, with experimental data.

3.3.1 Basic quantities

The units for normalization are the basic quantities $L_{\text{ref}}, m_{\text{ref}}, n_{\text{ref}}, T_{\text{ref}}$ and B_{ref} and the composed quantities:

$$c_{\text{ref}} = \sqrt{\frac{T_{\text{ref}}}{m_{\text{ref}}}}, \quad \rho_{\text{ref}} = \frac{m_{\text{ref}} c_{\text{ref}} c}{e B_{\text{ref}}}.$$

Typical choices for them are:

$$\begin{aligned} m_{\text{ref}} &= m_i, & n_{\text{ref}} &= n_e, & T_{\text{ref}} &= T_e, \\ L_{\text{ref}} &= R \text{ or } L_{\text{ref}} = a, & B_{\text{ref}} &= B(x=0) \text{ (i.e. at the magnetic axis).} \end{aligned}$$

The particle charge is normalized by the elementary charge e , i.e. $\widehat{Ze} = Z$. For the background density and temperature we can define the normalized profiles $\hat{n}_{p\sigma}, \hat{T}_{p\sigma}$:

$$n_{0\sigma}(x) = n_{\text{ref}} \hat{n}_{0\sigma}(x_0) \hat{n}_{p\sigma}(x), \quad T_{0\sigma}(x) = T_{\text{ref}} \hat{T}_{0\sigma}(x_0) \hat{T}_{p\sigma}(x),$$

thus splitting dimension, species and radial dependency.

The normalizations for the phase space coordinates reflect the anisotropy between the parallel and perpendicular plasma dynamics:

$$\begin{aligned} x &= \hat{x} \rho_{\text{ref}}, & y &= \hat{y} \rho_{\text{ref}}, & z &= \hat{z}, \\ v_{\parallel} &= \hat{v}_{\parallel} \hat{v}_{\text{th}\sigma} \Big|_{x_0} c_{\text{ref}}, & \mu &= \hat{\mu} \hat{T}_{0\sigma} \Big|_{x_0} \frac{T_{\text{ref}}}{B_{\text{ref}}}, & t &= \hat{t} \frac{L_{\text{ref}}}{c_{\text{ref}}}, \end{aligned}$$

For post-processing of simulations that consider the full radial extent of the torus it can be convenient to give x as a fraction of the minor radius a . The normalized

thermal velocity is $\hat{v}_{\text{th}} = \sqrt{2\hat{T}_{0\sigma}/\hat{m}_\sigma}$. Hence, the velocity space normalization is species-dependent to account for scenarios with differing temperatures. On the other hand we do not consider the radial dependence substantially yet: The notation $|_{x_0}$ means that the quantity is evaluated at the reference position x_0 , typically $x = 0.5a$ and the velocity space box sizes have to be chosen appropriately. There is undergoing work, though, to make use of an adaptive velocity space grid [39].

For spatial derivatives two different normalizations are used depending on whether they apply to background or fluctuating quantities:

$$\frac{\partial}{\partial x} = \begin{cases} \frac{1}{\rho_{\text{ref}}} \frac{\partial}{\partial \hat{x}} & \text{on fluctuating quantity,} \\ \frac{1}{L_{\text{ref}}} \frac{\partial}{\partial \hat{x}} & \text{on background quantity,} \end{cases}$$

and analogously for y . This reflects the gyrokinetic ordering in the normalization and puts the normalized quantities in the same order of magnitude.

The distribution function and the electrostatic potential are accordingly written as:

$$F_{0\sigma} = \hat{F}_{0\sigma} \frac{n_{\text{ref}}}{c_{\text{ref}}^3} \frac{\hat{n}_{0\sigma}}{\hat{v}_{\text{th}\sigma}^3} \Big|_{x_0}, \quad f_{1\sigma} = \hat{f}_{1\sigma} \frac{n_{\text{ref}}}{c_{\text{ref}}^3} \frac{\hat{n}_{0\sigma}}{\hat{v}_{\text{th}\sigma}^3} \Big|_{x_0} \frac{\rho_{\text{ref}}}{L_{\text{ref}}}, \quad \phi_1 = \hat{\phi}_1 \frac{T_{\text{ref}}}{e} \frac{\rho_{\text{ref}}}{L_{\text{ref}}}. \quad (3.2)$$

The normalized background local Maxwellian thus takes the form:

$$\hat{F}_{0\sigma}(x, v_{\parallel}, \mu) = \frac{\hat{n}_{p\sigma}(x)}{\pi^{3/2} \hat{T}_{p\sigma}^{3/2}(x)} e^{-\frac{v_{\parallel}^2 + \mu \hat{B}(x)}{\hat{T}_{p\sigma}(x)}}.$$

Finally, the collision frequency (2.38) can be written in normalized quantities as:

$$\underline{\nu}_{\sigma\sigma'} = \frac{4\hat{n}_{\sigma'} Z_{\sigma'}^2 Z_{\sigma}^2}{\hat{m}^{1/2} \hat{T}_{0\sigma}^{3/2}} \frac{c_{\text{ref}}}{L_{\text{ref}}} \nu_c \quad \text{with } \nu_c = \frac{\pi e^4 n_{\text{ref}} L_{\text{ref}} \ln \Lambda}{2^{3/2} T_{\text{ref}}^2}. \quad (3.3)$$

Obviously, the collision frequency depends on the radial position via the density and temperature. ν_c can be directly set to conveniently determine the overall collisionality of the simulated system. The collision operator is normalized accordingly:

$$C_{\sigma\sigma'}^{\text{L}} = \frac{c_{\text{ref}}}{L_{\text{ref}}} \frac{n_{\text{ref}}}{c_{\text{ref}}^3} \frac{\hat{n}_{0\sigma}}{\hat{v}_{\text{th}\sigma}^3} \Big|_{x_0} \rho_* \hat{C}_{\sigma\sigma'}^{\text{L}}.$$

3.3.2 Dimensionless parameters

The introduced normalizations also allow to define reference values for parameters that are already dimensionless by themselves, namely ρ_* and β_{ref} .

The length ratio $\rho_* = \rho_{\text{ref}}/L_{\text{ref}}$ fundamentally determines the importance of nonlocal effects in the system considered by relating the microscopic to the macroscopic scale. While local simulations are not affected by it, its value in global simulations is as a basic indicator for the importance of using the global model. It should be noted though, that

ρ_* only describes the impact of the machine dimensions (minor or major radius), which is not necessarily the decisive characteristic length (see Chapter 6).

The ratio $\beta_{\text{ref}} = 8\pi n_{\text{ref}} T_{\text{ref}} / B_{\text{ref}}^2$ controls the plasma pressure assumed for the particular magnetic equilibrium. It is consistent to set $\beta_{\text{ref}} = 0$ when choosing concentric circular flux surfaces. Since β_{ref} also determines the strength of electromagnetic effects (fluctuations of A), this choice justifies the electrostatic limit we are using in this work. As it turns out the normalized form of B_{\parallel}^* also becomes $B_{\parallel}^* = B$ for $\beta_{\text{ref}} = 0$ thus making the approximation made in Sec. 2.3.6 apply in a strict sense.

3.3.3 Kinetic and Poisson equation

With all quantities and derivatives normalized, we can now write the field-aligned first-order gyrokinetic equation in dimensionless form:

$$\begin{aligned} \frac{\partial \hat{f}_1}{\partial t} = & \frac{1}{\hat{c}} \partial_{\hat{y}} \hat{\phi}_1 \partial_{\hat{x}}^{n,T} \hat{F}_0 - \frac{1}{\hat{c}} (\partial_{\hat{x}} \hat{\phi}_1 \hat{\Gamma}_y - \partial_{\hat{y}} \hat{\phi}_1 \hat{\Gamma}_x) + \\ & + \frac{1}{\hat{c}} \frac{\hat{T}_0|_{x_0}}{Z} \cdot \frac{\hat{\mu} \hat{B} + 2 \hat{v}_{\parallel}^2}{\hat{B}} (\hat{K}_x \hat{\Gamma}_x - \hat{K}_y \hat{\Gamma}_y) - \frac{\hat{c}}{\hat{f} \hat{B}} \hat{v}_{\parallel} \hat{v}_{\text{th}}|_{x_0} \hat{\Gamma}_z + \\ & + \frac{\hat{c}}{\hat{f} \hat{B}} \frac{\hat{\mu}}{2} \partial_{\hat{z}} \hat{B} \frac{\partial \hat{f}_1}{\partial \hat{v}_{\parallel}} + \frac{1}{\hat{c}} \frac{\hat{T}_0|_{x_0}}{Z} \cdot \frac{\hat{\mu} \hat{B} + 2 \hat{v}_{\parallel}^2}{\hat{B}} \hat{K}_x \partial_{\hat{x}}^{n,T} \hat{F}_0 + \hat{C}^L(\hat{f}_1), \end{aligned} \quad (3.4)$$

where we have dropped the part of the curvature drift that is proportional to β_{ref} .

The normalized Poisson equation is:

$$\begin{aligned} \hat{\lambda}_D^2 \hat{\mathbf{V}}_{\perp}^2 \hat{\phi}_1 - \sum_{\sigma} \pi Z_{\sigma}^2 \frac{\hat{n}_{0\sigma}}{\hat{T}_{0\sigma}} \bigg|_{x_0} \int \left(\hat{\phi}_1 \hat{B} \frac{\hat{F}_{0\sigma}}{\hat{T}_{p\sigma}} - \left\langle \left\{ \hat{B} \hat{\phi}_{1\sigma} \frac{\hat{F}_{0\sigma}}{\hat{T}_{p\sigma}} \right\}_{x-\rho} \right\rangle_{\text{gy}} \right) d\hat{v}_{\parallel} d\hat{\mu} = \\ = - \sum_{\sigma} \pi \hat{n}_{0\sigma}|_{x_0} Z_{\sigma} \int \left\langle \left\{ \hat{B} \hat{f}_{1\sigma} \right\}_{x-\rho} \right\rangle_{\text{gy}} d\hat{v}_{\parallel} d\hat{\mu}, \end{aligned} \quad (3.5)$$

which contains the normalized Debye length,

$$\hat{\lambda}_D = \sqrt{\frac{B_{\text{ref}}^2}{4\pi n_{\text{ref}} m_{\text{ref}} c^2}},$$

meaning that the first term is very small compared to the rest of the left-hand side of the equation and can be justifiably left out.

With these normalizations the system of equations is now in a convenient form for discretization.

3.4 Steady state in global simulations

While local simulations intrinsically keep temperature, density and their respective gradients constant (in a time-averaged sense) by their periodic boundary conditions, the particle and heat fluxes in global scenarios will relax them and lose energy and

particles at the Dirichlet outer radial boundary. Thus, appropriate sources and sinks of heat and particles have to be introduced in order to reach the desired steady state. This can be achieved in two ways: as a *gradient-driven* or as a *flux-driven* scenario.

3.4.1 Gradient-driven setup

The first choice strives to preserve the initial state of the gradient profiles mirroring the behavior of the local case. In a δf splitting this means that adaptive sources need to be employed to force the perturbed part of the distribution function f_1 towards zero. GENE achieves this with Krook-type sources originally inspired by Ref. [40], implemented in Ref. [41] and expanded in Ref. [26]. The particle source is a term added to the right-hand side of the Fokker-Planck equation (2.40):

$$S_{P\sigma} = -\kappa_P \left(\langle f_\sigma(\mathbf{X}, |v_\parallel|, \mu) \rangle - \frac{\sum_{\sigma'} Z_{\sigma'} \langle \int \langle f_{\sigma'}(\mathbf{X}, |v_\parallel|, \mu) \rangle d^3v \rangle}{Z_\sigma n_{\text{spec}} \langle \int \langle F_{0\sigma}(\mathbf{X}, |v_\parallel|, \mu) \rangle d^3v \rangle} \langle F_{0\sigma}(\mathbf{X}, |v_\parallel|, \mu) \rangle \right),$$

where the prefactor κ_P regulates the strength of the source and the distribution function is symmetrized in v_\parallel to not introduce parallel momentum. n_{spec} is the total number of species considered in the simulation and $\langle \dots \rangle$ denotes the flux surface average as introduced in Sec. 2.1. This form of the source fulfills

$$\sum_\sigma Z_\sigma \left\langle \int S_{P\sigma} d^3v \right\rangle = 0,$$

i.e. it does not violate the quasineutrality and does not introduce spurious electrostatic potentials. The particle source is generally not needed for turbulence simulations with the adiabatic electron approximation, which is almost exclusively used for the results presented in this work, since density and potential fluctuations are in phase and produce no particle transport. If, however, the electrostatic potential is completely neglected in purely neoclassical simulations, the $v_d \cdot \nabla f_1$ term in Eq. (2.45) can drive particle transport and the source is required.

The Krook-type heat source has a similar form:

$$S_{H\sigma} = -\kappa_H \left(\langle f_\sigma(\mathbf{X}, |v_\parallel|, \mu) \rangle - \frac{\langle \int \langle f_\sigma(\mathbf{X}, |v_\parallel|, \mu) \rangle d^3v \rangle}{\langle \int \langle F_{0\sigma}(\mathbf{X}, |v_\parallel|, \mu) \rangle d^3v \rangle} \langle F_{0\sigma}(\mathbf{X}, |v_\parallel|, \mu) \rangle \right), \quad (3.6)$$

where the second term now ensures that S_H does not act as a particle source:

$$\left\langle \int S_{H\sigma} d^3v \right\rangle = 0.$$

The opposite is not true, though: Calculating the v^2 fluid moment of S_P shows that the particle source introduces heat. This can be remedied by replacing κ_H by $\kappa_{\text{eff}}(\mathbf{X}, \kappa_H, \kappa_P)$ whose definition can be found in Ref. [26].

3.4.2 Flux-driven setup

The second choice to achieve steady state is physically more meaningful but also computationally more challenging. Flux-driven scenarios operate with a fixed power input with the aim of predicting the time evolved profiles. Due to the connection of the source with the physical power input in Watts, we use explicit normalization notation here.

The heat source in this case is localized and is constructed in the dimensionless form:

$$\hat{S}_H = \hat{S}_0 \hat{S}_x \hat{S}_E, \quad (3.7)$$

where

$$\hat{S}_E = \frac{2}{3} \frac{1}{\hat{p}_{0\sigma}(x)} \left(\frac{\hat{v}_{\parallel}^2 + \hat{\mu} \hat{B}}{\hat{T}_p(x)} - \frac{3}{2} \right) \hat{F}_{0\sigma}$$

ensures that no particles or parallel momentum are introduced and $S_x(x)$ allows to specify a radial profile with the normalization

$$\int \hat{S}_x(x) \hat{f}(x, z) d\hat{V} = 1.$$

The remaining factor \hat{S}_0 , with the units

$$[\hat{S}_0] = \frac{n_{0\sigma}(x_0) \rho_{\text{ref}} c_{\text{ref}}}{\hat{v}_{\text{th}}^3(x_0) L_{\text{ref}}^2},$$

gives the source the desired amplitude with the correct dimensions, so that its volume integral is the normalized injected power:

$$P_{\text{add}} = \hat{S}_0 n_{\text{ref}} T_{\text{ref}} \rho_{\text{ref}}^3 \frac{c_{\text{ref}}}{L_{\text{ref}}}.$$

Compared to the Krook sources in Sec. 3.4.1 this type of source is much closer to the physical conditions in an experiment as it does not cool the plasma in the core to keep the profiles fixed. The price to pay for this is that the profiles must evolve to their steady state over transport time scales, which are typically another order of magnitude longer than the already big ion-ion collision time.

Additionally, strong deviations from the initial state profiles will violate the δf splitting employed in the derivation of the gyrokinetic Vlasov equation. So unless the initial condition is already a good guess of the equilibrium state measures have to be taken to ensure $f_1/F_0 = \varepsilon_\delta \ll 1$.

Resetting the distribution function

GENE solves this by adapting the background profiles and thus the Maxwellian F_0 . This is not an entirely physical evolution but amounts to an iterative optimization of the initial state. If f_1/F_0 or the corresponding fluid moment ratios n_1/n_0 and T_1/T_0 exceed a prespecified threshold value, typically around 0.1, the time stepping scheme is stopped and the following procedure performed:

1. Set the new background temperature and density profiles based on the current total distribution function:

$$n_{0\sigma,\text{new}} = n_{0\sigma} + n_{1\sigma}, \quad T_{0\sigma,\text{new}} = T_{0\sigma} + T_{1\sigma}.$$

2. Apply a smoothing filter to these new profiles to remove gyroradius scale fluctuations which are formally and numerically problematic when they are transferred to the background profiles and distribution function. The default choice is a Gaussian filter with adjustable window width, typically 10 ion gyroradii.
3. Use the smoothed profiles to define the new background Maxwellian distribution $F_{0\sigma,\text{new}}(n_{0\sigma,\text{new}}, T_{0\sigma,\text{new}})$.
4. Reinitialize the time stepping scheme with

$$f_{1\sigma,\text{new}} = F_{0\sigma} + f_{1\sigma} - F_{0\sigma,\text{new}}.$$

We will further address the numerical challenges and limitations of this method in the context of simulation results in Sec. 6.2.

For obvious reasons, flux-driven simulations are the preferred operation mode of full-f codes (which do not employ the f_1, F_0 splitting) and it is possible to observe the physical evolution from an arbitrary initial state to the equilibrium with them.

3.5 Observables

While the formalism and numerical schemes presented so far are mainly concerned with the distribution function of the gyrocenters f_1 , the foremost goal of any numerical simulation is to make predictions on physically measurable quantities such as density, temperature, mean flow velocities and the fluxes of particles, heat and momentum in particle space. We shall now present how to gain those tangible quantities from the distribution function. In GENE they are calculated in regular intervals and output as binary or ASCII data (and optionally in the HDF5 format).

The starting point are the fluid moments defined in Eq. (2.43), which are normalized according to Sec. 3.3:

$$M_{\sigma}^{ab}(\mathbf{x}) = \rho_* n_{\text{ref}} \hat{n}_{0\sigma}(x_0) c_{\text{ref}}^{a+b} \hat{v}_{\text{th}_\sigma}^{a+b}(x_0) \hat{M}_{\sigma}^{ab}(\mathbf{x}).$$

These moments contain the transformation to particle space so that we can calculate, for example, the (normalized) density, temperature and parallel flow velocity fluctuations of species σ :

$$n_{1\sigma} = M_{\sigma}^{00}, \quad T_{1\sigma} = (M_{\sigma}^{20} + 2M_{\sigma}^{02})/3n_{\sigma}, \quad u_{\parallel} = M_{\sigma}^{10}/n_{\sigma}.$$

We monitor the parallel flow more closely in the form of

$$j_{B\sigma} = Z_{\sigma} e \langle u_{\parallel\sigma} B \rangle = Z_{\sigma} e \left\langle B \int v_{\parallel} f_{1\sigma} d^3v \right\rangle = Z_{\sigma} e \langle B M_{\sigma}^{10} \rangle, \quad (3.8)$$

which is the contribution of each species to the bootstrap current. While each individual summand is of first order, their sum $j_{BS} = \sum_{\sigma} j_{B\sigma}$ is second order as the electron current nearly compensates the ion current [12].

Since it determines the confinement time and thus ultimately the energy yield of a fusion device, measuring cross-field transport is of foremost interest in numerical simulations. The origin of these fluxes is the radial component of the drift $\mathbf{v}_D = \mathbf{v}_d + \mathbf{v}_\phi$ (see Eq. (2.7) and (2.25)). We do not measure the classical fluxes (see Sec. 2.2.1) as they are negligibly small compared to both turbulent and neoclassical fluxes in all relevant scenarios.

The normalization of radial fluxes in GENE are so-called *gyro-Bohm units*, which are based on the assumption that transport is coupled to the gyroradius scale, i.e. that it is a local effect:

$$\Gamma_{gB} = n_{\text{ref}} c_{\text{ref}} \rho_*^2, \quad \Pi_{gB} = n_{\text{ref}} m_{\text{ref}} c_{\text{ref}}^2 \rho_*^2, \quad Q_{gB} = p_{\text{ref}} c_{\text{ref}} \rho_*^2.$$

Although this scaling is not found everywhere in experiments and simulations, it still fulfills the purpose of avoiding very large or small numbers in numerical schemes quite well. A notable feature of the gyro-Bohm heat flux is its strong temperature dependency of $T_{\text{ref}}^{5/2}$. This means that scenarios with similar dimensionless quantities can exhibit quite different physical heat fluxes.

3.5.1 Turbulent fluxes

The radial fluxes measured in GENE as *turbulent fluxes* of particles, parallel momentum and heat are in the electrostatic limit those driven by the fluctuating component of the $\mathbf{E} \times \mathbf{B}$ velocity \mathbf{v}_ϕ :

$$\begin{aligned} \Gamma_{\text{turb}}^x &= \left\langle \int \mathbf{v}_\phi^x f_1(\mathbf{x}, \mathbf{v}) d^3v \right\rangle, \\ \Pi_{\text{turb}}^x &= \left\langle \int \mathbf{v}_\phi^x v_{\parallel} f_1(\mathbf{x}, \mathbf{v}) d^3v \right\rangle, \\ Q_{\text{turb}}^x &= \left\langle \int \mathbf{v}_\phi^x (\mathbf{v} - \mathbf{u})^2 f_1(\mathbf{x}, \mathbf{v}) d^3v \right\rangle \approx \left\langle \int \mathbf{v}_\phi^x v^2 f_1(\mathbf{x}, \mathbf{v}) d^3v \right\rangle. \end{aligned}$$

The flux surface average $\langle \dots \rangle$ means that we are interested in the net flux through a magnetic surface. In field-aligned coordinates \mathbf{v}_ϕ^x is written as:

$$\mathbf{v}_\phi^x = -\frac{c}{\mathcal{C}} \left(\frac{\partial \phi_1}{\partial y} - \frac{g_{23}}{g_{33}} \frac{\partial \phi_1}{\partial z} \right),$$

where we neglect the second part based on the parallel wave number ordering. Thus we define:

$$\begin{aligned}\Gamma_{\text{turb}}^x &= \left\langle -\frac{c}{\mathcal{C}} \frac{\partial \phi_1}{\partial y} M^{00}(\mathbf{x}) \right\rangle = -\Gamma_{\text{gB}} \frac{\hat{n}_0}{\hat{\mathcal{C}}} \left\langle -\frac{\partial \hat{\phi}_1}{\partial \hat{y}} \hat{M}^{00}(\hat{\mathbf{x}}) \right\rangle, \\ \Pi_{\text{turb}}^x &= m \left\langle -\frac{c}{\mathcal{C}} \frac{\partial \phi_1}{\partial y} M^{10}(\mathbf{x}) \right\rangle = -\Pi_{\text{gB}} \frac{\hat{m} \hat{n}_0 \hat{v}_{\text{th}}}{\hat{\mathcal{C}}} \left\langle -\frac{\partial \hat{\phi}_1}{\partial \hat{y}} \hat{M}^{10}(\hat{\mathbf{x}}) \right\rangle, \\ Q_{\text{turb}}^x &= \frac{m}{2} \left\langle -\frac{c}{\mathcal{C}} \frac{\partial \phi_1}{\partial y} (M^{20}(\mathbf{x}) + M^{02}(\mathbf{x})) \right\rangle = -Q_{\text{gB}} \frac{\hat{n}_0 \hat{T}_0}{\hat{\mathcal{C}}} \left\langle -\frac{\partial \hat{\phi}_1}{\partial \hat{y}} (\hat{M}^{20}(\hat{\mathbf{x}}) + \hat{M}^{02}(\hat{\mathbf{x}))) \right\rangle.\end{aligned}$$

Notably, if we consider the y dependence in Fourier space (as we do generally in this work) the $k_y = 0$ component of f_1 and F_0 do not contribute to these fluxes.

3.5.2 Neoclassical fluxes

The definition of the *neoclassical fluxes* is a bit more involved. There are two ways of defining them, which are straightforwardly shown to be equivalent in the local model but require additional attention in the global one. In the latter case the goal is to find a definition that is consistent with other observables, e.g. to have vanishing particle fluxes for a purely neoclassical simulation without density profile evolution and no particle source (see Sec. 4.2). Additionally, turbulent and neoclassical effects do not fully separate in a global simulation - studying their interaction is the goal of this work, after all. Thus the name neoclassical fluxes becomes a formal denomination for the radial fluxes occurring due to the $k_y = 0$ mode of the distribution function.

Fluxes in the local limit

As stated in Sec. 2.3.7, it is not possible to calculate the self-consistent electrostatic potential in the local model because the neoclassical particle fluxes are automatically ambipolar in all orders of ε_δ we are considering. This is shown by finding that the particle flux can be expressed via the parallel friction force $F_{\parallel} = \int m v_{\parallel} C(f_1) d^3v$ [9, 27] (for the definition of I and ψ see Sec. 2.1):

$$\Gamma_{\text{nc}}^x = -\frac{I}{d\psi/dx} \left\langle \frac{F_{\parallel}}{ZeB} \right\rangle, \quad (3.9)$$

where we cast the radial coordinate from the poloidal flux ψ to the minor radius of the flux surface $x = r$ by means of $\nabla\psi = \frac{d\psi}{dx} \nabla x$. Ambipolarity of the fluxes is the requirement:

$$\sum_{\sigma} Z_{\sigma} \Gamma_{\text{nc}\sigma} = 0,$$

which can easily be shown to hold for Eq. (3.9) by using the conservation of momentum from Eq. (2.36).

In order to derive a definition involving the drift from Eq. (3.9), we have to insert the drift-kinetic equation (2.46) in steady state ($\partial_t f_1$) for the collision operator. This

results in:

$$\Gamma_{\text{nc}}^x = \frac{I}{d\psi/dx} \left\langle \underbrace{\frac{1}{ZeB} \int mv_{\parallel}^2 \left(\mathbf{b} \cdot \nabla f_1 - \frac{\mu}{mv_{\parallel}} \frac{\partial f_1}{\partial v_{\parallel}} \mathbf{b} \cdot \nabla B \right)}_{\text{I}} + \underbrace{mv_{\parallel} \mathbf{v}_d^x \cdot \nabla F_0}_{\text{II}} d^3v \right\rangle.$$

The integral over Term II vanishes because it is odd in v_{\parallel} . Term I can be transformed using

$$(\hat{\mathbf{b}} \times \nabla B) \cdot \nabla \psi = -IB \cdot \nabla B, \quad (3.10)$$

which makes use of the system's axisymmetry and we find:

$$\Gamma_{\text{nc}}^x = \left\langle \int \left(\frac{mv_{\parallel}^2}{eB^2} + \frac{\mu}{eB} \right) (\mathbf{b} \times \nabla B) \cdot \nabla_x f_1 d^3v \right\rangle = \left\langle \int v_d^x f_1 d^3v \right\rangle. \quad (3.11)$$

This form shows a nice correspondence with the turbulent flux definition and we can write it in component form as:

$$\Gamma_{\text{nc}}^x = \left\langle \frac{mK_x}{CZeB} \left(\frac{1}{2} M^{20}(\mathbf{x}) + M^{02}(\mathbf{x}) \right) \right\rangle = \Gamma_{\text{gB}} \left\langle 2\hat{K}_x \frac{\hat{n}_0(x_0)\hat{T}_0(x_0)}{Z\hat{B}} \left(\frac{1}{2} \hat{M}^{20}(\hat{\mathbf{x}}) + \hat{M}^{02}(\hat{\mathbf{x}}) \right) \right\rangle. \quad (3.12)$$

A similar argument holds for the energy flux, which we measure in the form:

$$Q_{\text{nc}}^x = \left\langle \int \frac{m}{2} v^2 v_d^x f_1 d^3v \right\rangle, \quad (3.13)$$

$$\begin{aligned} Q_{\text{nc}}^x &= \left\langle \frac{m^2 K_x}{2CZeB} \left(\frac{1}{2} M^{40} + \frac{3}{2} M^{22} + M^{04} \right) \right\rangle = \\ &= Q_{\text{gB}} \left\langle 2\hat{K}_x \frac{\hat{n}_0(x_0)\hat{T}_0(x_0)^2}{Z\hat{B}} \left(\frac{1}{2} \hat{M}^{40} + \frac{3}{2} \hat{M}^{22} + \hat{M}^{04} \right) \right\rangle. \end{aligned} \quad (3.14)$$

The parallel momentum flux definition is accordingly:

$$\Pi_{\text{nc}}^x = \left\langle \int mv_{\parallel} v_d^x f_1 d^3v \right\rangle, \quad (3.15)$$

$$\Pi_{\text{nc}}^x = \left\langle \frac{m^2 K_x}{CZeB} \left(\frac{1}{2} M^{30}(\mathbf{x}) + M^{12}(\mathbf{x}) \right) \right\rangle = \Pi_{\text{gB}} \left\langle 2\hat{K}_x \frac{\hat{n}_0(x_0)\hat{m}^2 \hat{v}_{\text{th}0}(x_0)^3}{Z\hat{B}} \left(\frac{1}{2} \hat{M}^{30} + \hat{M}^{12} \right) \right\rangle. \quad (3.16)$$

It should be emphasized again, that only the $(k_x, k_y) = (0, 0)$ mode of the distribution function contributes to these fluxes. Thus, they are entirely decoupled from the turbulent fluxes, which depend on finite wave numbers.

Fluxes in global simulations

In the global model this separation does not formally exist: The maximal spatial scale (i.e the lowest possible wave number k_x) is now given by the system size. Consequently, we also can calculate the self-consistent electrostatic potential ϕ_1 and have to include

its contributions. If we start again from the parallel friction definition (3.9) for the particle flux, inserting the kinetic equation Eq. (2.32) now yields:

$$\begin{aligned} \Gamma_{\text{nc}}^x = \Gamma_{\text{nc,loc}}^x &+ \frac{I}{d\psi/dx} \underbrace{\left\langle \frac{1}{ZeB} \int m v_{\parallel} \left(\mathbf{v}_d^x \cdot \nabla f_1 + \frac{ZeF_0}{T_0} \mathbf{v}_d^x \cdot \nabla \phi_1 \right) d^3v \right\rangle}_{\text{III}} + \\ &+ \frac{I}{d\psi/dx} \underbrace{\left\langle \int \frac{ZeB}{T_0} m v_{\parallel}^2 F_0 \hat{\mathbf{b}} \cdot \nabla \phi_1 d^3v \right\rangle}_{\text{IV}}, \end{aligned}$$

i.e. we need to treat two additional terms compared to the local result. In term III, the field dependent summand is odd in v_{\parallel} and hence vanishes. We neglect its other part on the basis that it is formally higher order than the rest. The contribution from term IV on the other hand corresponds to the covariant x-component of the $\mathbf{E} \times \mathbf{B}$ drift from z-variations of ϕ_1 . Using Eq. (3.10) we can show that:

$$-\frac{I}{d\psi/dx} \left\langle \int \frac{ZeB}{T_0} m v_{\parallel}^2 F_0 \hat{\mathbf{b}} \cdot \nabla \phi_1 d^3v \right\rangle = \left\langle \int \frac{m v_{\parallel}^2}{T_0 B} F_0 (\hat{\mathbf{b}} \times \nabla \phi_1) \cdot \nabla x d^3v \right\rangle.$$

In fact, this represents transport due to poloidal variations of the potential because axisymmetry does not allow a toroidal component of the parallel derivative. It is also straightforward to show that term III can be reproduced by evaluating the local definition Eq. (3.11) for $f_1 + \frac{F_0}{ZeT_0} \phi_1$ instead of f_1 . Comparing with the form of the pull-back operator (2.42) this provides a convenient way to implement term III. In conclusion the definition of the particle flux in global simulations amounts to:

$$\Gamma_{\text{nc}}^x = \left\langle \int ([f_1]_{k_y=0} \mathbf{v}_d^x + F_0 [\mathbf{v}_{\phi}^x]_z) d^3v \right\rangle, \quad (3.17)$$

where the contribution of $F_0 \mathbf{v}_d^x$ vanishes for up-down symmetric systems such as the one we are considering. In other cases, the asymmetries in the curvature are small and it is still legitimate to neglect this flux. In component form we can simply employ Eq. (3.12) to calculate the normalized flux if the moments M^{ab} are modified so that $T^* f_{1\sigma} = f_{1\sigma}$.

The energy flux is derived in an analogous way as

$$Q_{\text{nc}}^x = \left\langle \int \frac{m v^2}{2} ([f_1]_{k_y=0} \mathbf{v}_d^x + F_0 [\mathbf{v}_{\phi}^x]_z) d^3v \right\rangle, \quad (3.18)$$

and the normalized component form is equal to Eq. (3.14) with the modified moments. It is important to note that this is only the flux of *kinetic* energy. It can lead to an increase in electron heat flux by a factor of $\sqrt{m_i/m_e}$ compared to the local result. Helander has pointed out in Ref. [42], though, that the kinetic energy flux is compensated by a flux of *potential* energy:

$$Q_{\text{pot}}^x = \left\langle \int Ze \phi_1 F_0 \mathbf{v}_d^x d^3v \right\rangle.$$

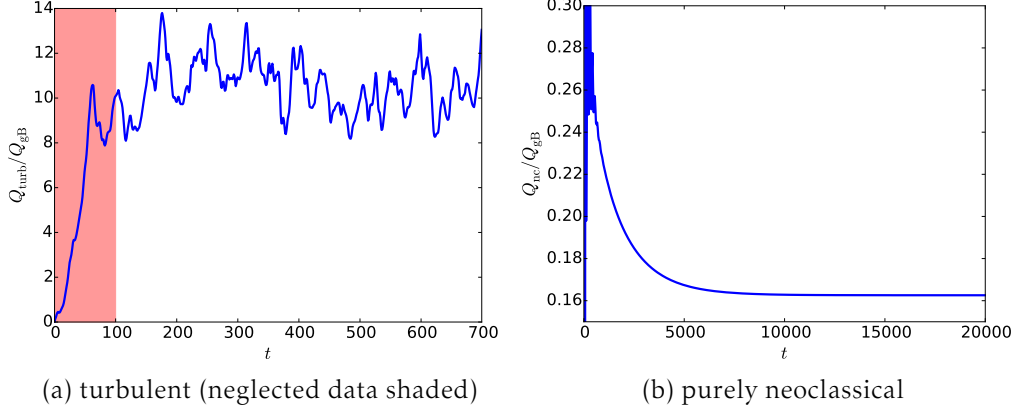


Figure 3.1: Examples of simulation time traces starting at $t = 0$. Time units are normalized according to Sec. 3.3, i.e. a/c_s .

This effect was also shown in numerical simulations [43]. For the ion heat flux it only provides a small correction, so it is not included in the present study. Future investigations which do not use the adiabatic electron approximation will have to take it into account, though.

Finally, the momentum flux is:

$$\Pi_{\text{nc}}^x = \left\langle \int m v_{\parallel} ([f_1]_{k_y=0} v_d^x + F_0 [v_{\phi}^x]_z) d^3 v \right\rangle, \quad (3.19)$$

and we can use the same concept as for particle and heat flux to calculate it with Eq. (3.16).

3.5.3 Error estimation for the fluxes

With the expressions for the radial fluxes established, it is an important question how reliable estimates of these and their uncertainty can be given based on data from numerical simulations. A very natural first step is, of course, to neglect data from the initial phase of the simulation. As can be seen for the turbulent example in Fig. 3.1 this phase is easily recognizable.

In the case of purely neoclassical systems (without turbulent fluctuations in a global simulation, see Chapter 4), the final result is a steady state established over several collision times and the fluxes (ideally) have constant values as shown for the energy flux in Fig. 3.1(b). Thus their uncertainty can only be estimated by considerations of the exactness of the underlying theory and comparisons between several simulations. An example for the former is that the collision operator is only accurate up to first order in $1/\ln \Lambda \approx 1/10 - 1/20$ (see Sec. 2.3.4), i.e. neoclassical fluxes cannot be more accurate than up to 5-10% tolerance. Comparisons between simulations can give hints on the influence of non-physical parameters, such as the grid resolution or numerical schemes.

Turbulent fluxes, on the other hand, fluctuate, i.e. their time evolution follows a probability distribution and we can use statistical analysis for them. The same applies

to the neoclassical fluxes measured in global turbulence simulations where the two phenomena cannot be separated. An important feature of these time series is that the neighboring data values are usually correlated; physically, the autocorrelation time t_c may, for instance, represent the lifetime of turbulent eddies. We estimate t_c by calculating the discrete autocorrelation function:

$$R(t_i) = \sum_{j=0}^N q_i q_{i+j} \quad \text{with } q_i = Q_i - \langle Q \rangle, \quad (3.20)$$

$$R(t_c) = R(t_0)/e, \quad (3.21)$$

where $\langle Q \rangle$ is the average over the entire time trace.

In order to calculate a meaningful error based on the standard deviation, we thus preprocess the flux data by combining all measurements within windows of several autocorrelation times into a single mean value. This can be understood as a form of *subsampling* or *two-stage sampling* [44]. Ref. [45] refers to this method as *batch means*. The set of window averages is now assumed to constitute statistically independent measurements. It is important to note that the estimate of the correlation time does not need to be very robust; it is sufficient if it is not grossly underestimated. In terms of physical processes we have grouped measurements belonging to single turbulent eddies. In the following we denote the time average over one window by \bar{Q}_n and the average over all window averages by $\langle Q \rangle$ as it is equivalent to the mean of all data due to the linearity of the mean value.

The standard deviation of the window means is then calculated according to the usual expression:

$$\sigma_{\text{win}} = \sqrt{\frac{1}{N_{\text{win}} - 1} \sum_{n=1}^{N_{\text{win}}} (\bar{Q}_n - \langle Q \rangle)^2}.$$

In general, the standard deviation of the full sample σ provides an estimate of the amplitude of the turbulent fluctuations, which can be used as a proxy to estimate the uncertainty of the fluxes. Its application to the window means, though, suffers from a number of flaws as we will show in the following. On the other hand, if we consider our dataset as a sample of an infinitely long time series, the standard estimate for the error of the sample mean compared to the mean of the infinite series is

$$s_{\text{win}} = \frac{\sigma_{\text{win}}}{\sqrt{N_{\text{win}}}} \quad \text{or for small } N_{\text{win}}: s_{\text{win}} = \frac{\sigma_{\text{win}}}{\sqrt{N_{\text{win}} - 2}}, \quad (3.22)$$

where the second expression assumes a Student's t -distribution rather than a Gaussian. This is a statistically rigorous estimate of the uncertainty of the mean. Standard deviation and standard error can also be divided by the mean $\langle Q \rangle$ giving the relative quantities $\hat{\sigma}$ and \hat{s} (as well as their windowing equivalents).

A basic test for this calculation is a set of artificial data of the form:

$$Q_n = 2.5 + 10\xi_n,$$

where $\xi_n \in [0, 1)$ is a (pseudo-)random number, i.e. we have a set of completely uncorrelated data which is shown in Fig. 3.2(a).

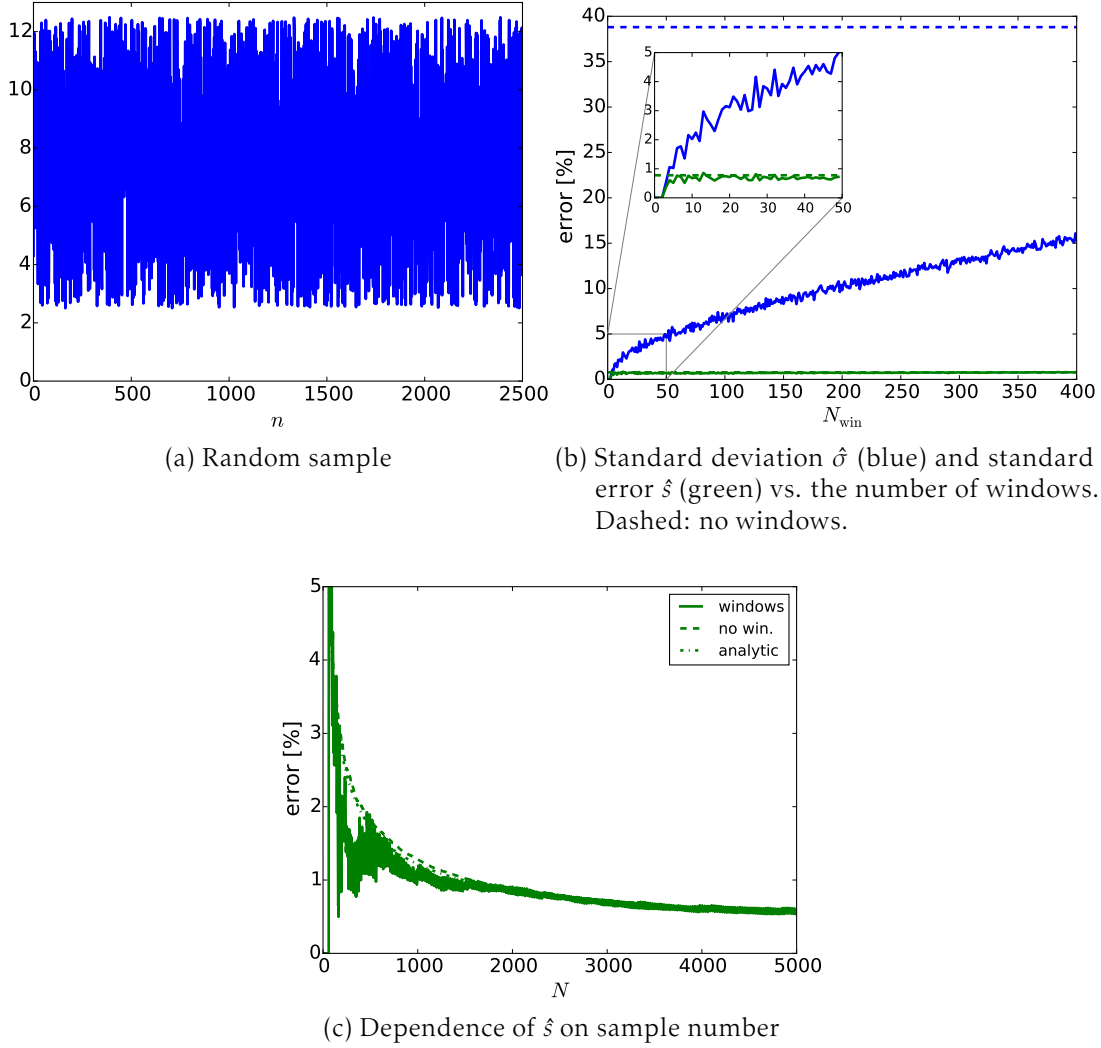


Figure 3.2: Artificial uncorrelated dataset of random numbers

In Fig. 3.2(b) we study the dependence of our two choices of uncertainty quantification on the number of averaging windows used. The standard deviation of samples from a uniform distribution of width w is known to be $\sigma_0 = w/2\sqrt{3}$, i.e. $\hat{\sigma}_0 = \sigma_0/\langle Q \rangle = 38\%$, which can be found as the blue dashed line in Fig. 3.2(b). The corresponding relative standard error of the mean depends on the number of samples N . In our case of $N = 2500$ it is $\hat{s}_0 = 0.8\%$ (dashed green line). These two values form the reference for the estimators based on the two-stage sampling. As should be the case for uncorrelated data, the windows' standard error of the mean agrees well with its target value and is largely independent from the number of windows (solid green line). The standard deviation of the window means, on the other hand, is systematically smaller than its reference and scales with $\sqrt{N_{\text{win}}}$ for fixed N (solid blue line). This means that considerable care needs to be taken when interpreting its exact value.

If we, on the other hand, consider how the uncertainty estimate scales with the number of samples - practically the length of the simulation - it is obvious that σ

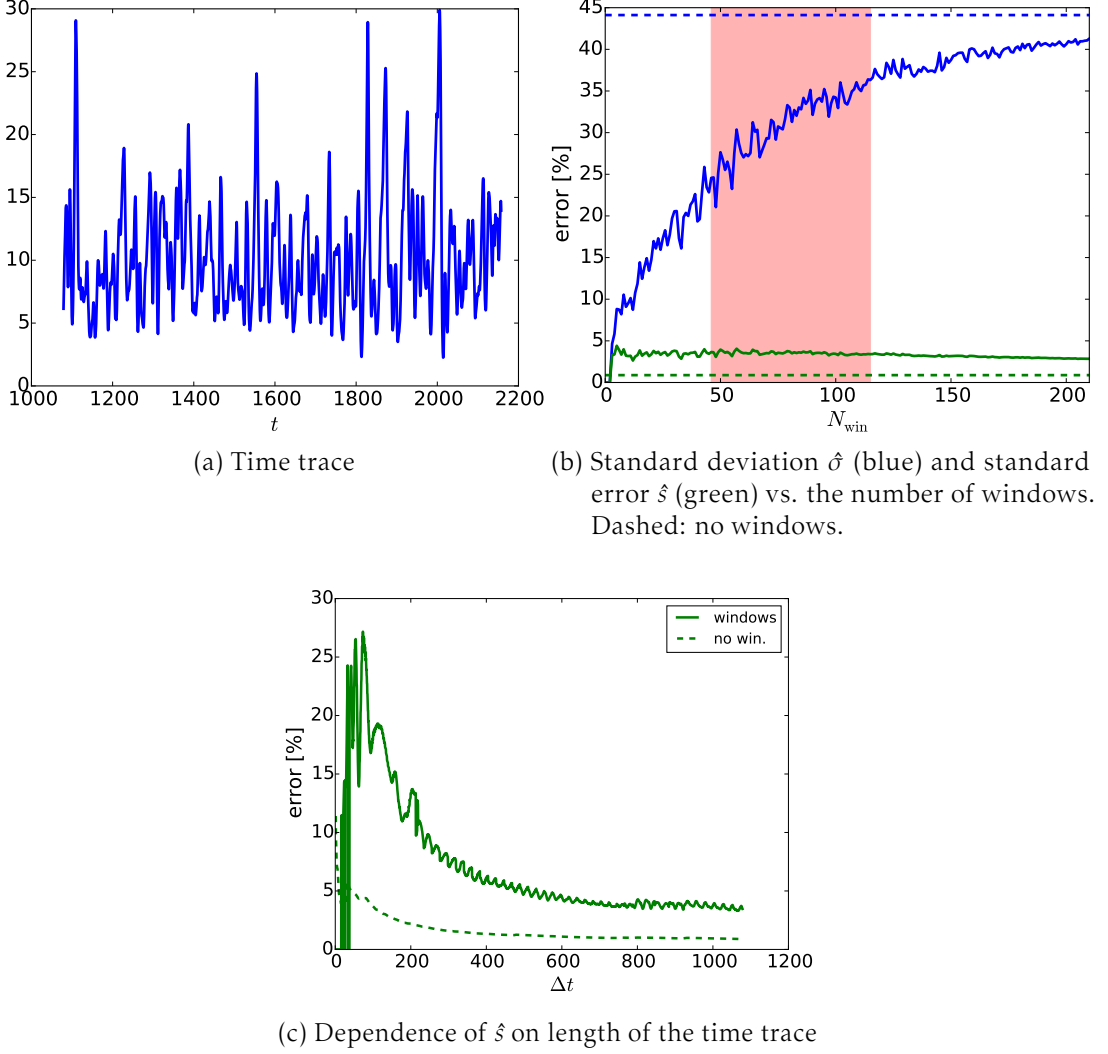


Figure 3.3: Turbulent heat flux from a global ITG simulation (from chapter 6)

(windowed or not) is independent from it for sufficiently large N ; it represents the width of the distribution function after all. Consequently, the standard error of the mean scales with $N^{-1/2}$ exhibiting the intuitively expected property that the uncertainty should decrease with a growing number of samples. In Fig. 3.2(c) we illustrate this for our random dataset and fixed windows containing 25 samples each compared to the straightforward standard error of the mean and its analytical reference \hat{s}_0 . The batch subsampling clearly increases the minimum N required to arrive at a robust value for the error but beyond this limit we achieve good agreement of all three curves.

The necessity of the batch procedure naturally becomes apparent when we analyze a time trace of autocorrelated simulation data. As previously mentioned the samples are assumed to be correlated over a time span of approximately the turbulent eddy lifetime; in this case the autocorrelation function decays to $1/e$ after $t_c = 4.7$ time units, an order of magnitude that appears plausible for the time trace of Fig. 3.3(a). If the

Subsampling	$\hat{\sigma}$	\hat{s}
no windows	44%	0.8%
48 windows ($5t_c$)	23%	3.4%
115 windows ($2t_c$)	36%	3.4%

Table 3.1: Standard deviation and error of the mean for turbulent heat fluxes

width of the averaging windows is determined based on multiples of this time, we arrive at the estimates for the full time trace length presented in Tab. 3.1. The $5t_c$ and $2t_c$ window numbers are also the left and right boundary of the shaded region in Fig. 3.3(b) where we again show the dependence of the estimators on the number of subsampling windows chosen for the entire time trace length. The standard error of the mean \hat{s} exhibits good properties: it is nearly independent of the number of windows, at least in the range that is typically used, and its value for the window averages is larger than for the full sample, i.e. respecting the autocorrelation of the data increases the uncertainty. The standard deviation of the windows, however, again shows a scaling with $\sqrt{N_{\text{win}}}$ for a fixed time interval and is generally smaller than the standard deviation of the full sample. This is somewhat plausible because the window averaging removes strong bursts, e.g. at $t \approx 2000$ and this effect is stronger for big windows.

If we study only parts of the time trace with varying length but keep the window size fixed (e.g. $5t_c$), the number of windows scales linearly with the length of the time trace, analyzing more data can possibly lead to a higher error estimate with the window standard deviation. At best, it remains independent of the length of the time trace. The standard error, on the other hand, has a scaling of $N_{\text{win}}^{-1/2} \sim \Delta t$; the uncertainty estimate for the mean improves for longer simulations if they remain in a state of equilibrium. The batch mean standard error in Fig. 3.3(c) also shows a small modulation caused by the fact that the number of windows has to be a positive integer.

In conclusion, the standard error of the $5t_c$ window means is our recommended estimator for the uncertainty caused by the limited length of a turbulence simulation. Selecting smaller multiples of the correlation time, such as $2t_c$, would also be possible for the case shown in Fig. 3.3 as the estimator is relatively independent of the number of windows. Longer windows, however, provide a safety margin against underestimates of the correlation time. A caveat of the proposed method is that it only removes the bias on the error estimate originating from short-time correlations, typically the turbulent eddy life time. Many systems under consideration, though, exhibit phenomena which introduce long-term correlations to the measured quantities. Examples for this are the occurrence of intermittency and transient bursts when turbulence becomes weak or cases of bifurcation. If the simulation time is big enough, the standard error can become negligibly small compared to other errors, especially for comparisons with experimental data, which introduce uncertainties in the simulation parameters. Future work could be the construction of an a priori estimator for the error based on known properties of the distribution function, e.g. in Ref. [46], in order to determine an optimal run time for nonlinear simulations.

The standard deviation of the sample on the other hand provides an estimate of the fluctuation amplitude, which is a quantity worth studying in its own right. It can

even be used (cautiously) as an error estimator for the mean because it provides a rather pessimistic error margin that can cover other error sources. The subsampling procedure, however, introduces a severe bias and an alternative estimator for the fluctuation amplitude should be found while still respecting the autocorrelation of the fluctuations.

3.6 Summary

In this chapter elements of the numerical implementation of the gyrokinetic equation which are relevant for this work were introduced. This included the basic distinction between global and local simulations, the normalization used by the GENE code, the discretization and the choice of boundary conditions for the phase space directions. Furthermore, the two ways of establishing a steady state in global simulations were presented and discussed. Lastly, expressions were introduced to calculate physical quantities from the distribution function, especially radial transport fluxes. This included the discussion of means for estimating the uncertainty of these fluxes, concluding that due to their inherent autocorrelation the measurements from their time series should be grouped into batches whose means are not correlated. The standard error of the mean of these batch/window means then provides a sound uncertainty estimate.

In the following chapter the presented methods will be employed to investigate systems that contain exclusively neoclassical effects.

Chapter 4

Purely neoclassical systems

Before studying neoclassical phenomena in turbulent systems it is also worthwhile to investigate them on their own. A number of theoretical predictions exist for local scenarios, so the numerical calculations can be benchmarked against them. This also provides an excellent numerical test, especially, for the collision operator. In global simulations the influence of effects exclusive to the model are investigated. In particular, the focus lies on the radial electric field, whose physically correct representation is crucial for the turbulence studies later in this work. Furthermore, the situation near the magnetic axis where neoclassical transport becomes nonlocal and analytic predictions in the literature have obtained contradicting results will be studied.

The simulations performed in this chapter are purely neoclassical in the sense that only the $k_y = 0$ (and additionally $k_x = 0$ in the local case) Fourier component of the distribution function is considered and consequently only the linear part of the gyrokinetic Vlasov equation is solved.

4.1 Local neoclassical benchmarks

The validity of the neoclassical equilibrium solver for the flux-tube limit has already been well established in Ref. [24]. In this chapter additional tests which are significant as a preparation for global simulations are presented. In particular these are results of the initial value (IV) solver. Local simulations with the IV solver are in general more costly than the algebraic (NC) solver as they need at least several ion-ion collision times to ensure convergence. On the other hand they tend to be more robust and convergence can be monitored more easily (see Sec. 3.2). We also use this opportunity to introduce three relevant analytic predictions for neoclassical radial transport of energy. A fundamental aspect here, is that expressions are usually derived for the *conductive* heat flux q_{nc} , which is related to the energy flux by

$$q_{\text{nc}} = Q_{\text{nc}} - \frac{5}{2} T \Gamma_{\text{nc}}. \quad (4.1)$$

For simulations employing the adiabatic electron approximation, such as all in this thesis, this distinction is less relevant as $\Gamma = 0$ holds for them.

For the Pfirsch-Schlüter regime ($\nu_* \gg 1$), the high collisionality justifies a fluid treatment. Since collisions disrupt the banana orbits, the random walk estimate given

in Sec. 2.2 is not valid, but the presence of the magnetic curvature still provides an enhancement of q^2 over classical transport. The original derivation by Pfirsch and Schlüter was never published, but it can be found in several reviews on the topic [9, 28, 47]. Its end result for the ion heat flux, as given in Ref. [9], is

$$q_{\text{PS},i}^x = -I^2 \left\langle \frac{(B\kappa_{\wedge,i})^2}{\kappa_{\parallel,i}} \left(\frac{1}{B^2} - \frac{1}{\langle B^2 \rangle} \right) \right\rangle \frac{\partial T_i}{\partial x}, \quad (4.2)$$

where

$$\kappa_{\wedge,i} = \frac{5n_{0i}T_i}{2m_i\Omega_i}, \quad \kappa_{\parallel,i} = 3.9 \frac{n_iT_i\tau_i}{m_i}.$$

In fact, the Pfirsch-Schlüter flux is present in all collisionality regimes as it is an effect caused purely by the field curvature. Since it only scales with q^2 , effects that scale with $q^2\epsilon^{-3/2}$ overshadow it at low collisionality.

For the limit of very low collisionality the most accurate prediction was derived by Taguchi [48]. It has the form:

$$q_{\text{Ta},i} = -\frac{2n_iT_iI^2}{m_i\Omega_i^2\tau_i} \left(\left\langle \frac{B_0^2}{B^2} \right\rangle - \frac{f_c}{f_c + 0.462f_t} \right) \frac{\partial T_i}{\partial x}, \quad (4.3)$$

which contains the fraction of free particles f_c and of trapped particles $f_t = 1 - f_c$.

The most common expression for the heat flux is the so-called *Chang-Hinton formula* [49], which provides a prediction for a large parameter regime by interpolating between the $\epsilon \ll 1$ and $\epsilon = 1$ limit as well as for ν_* from the banana up to the Pfirsch-Schlüter regime. The full formula also includes corrections for Shafranov shift and the presence of heavy high-Z impurities, which we leave out here for the sake of clarity:

$$q_{\text{CH},i} = -\epsilon^{1/2} n_i \frac{\rho_{\theta,i}^2}{\tau_i} K_2 \frac{\partial T_i}{\partial x}, \quad (4.4)$$

where

$$K_2 = \frac{0.66 + 1.88\epsilon^{1/2} - 1.54\epsilon}{1 + 1.03\nu_*^{1/2} + 0.31\nu_*} \left\langle \frac{B_\varphi^2}{B^2} \right\rangle + 1.6 \frac{0.74\nu_*\epsilon^{3/2}}{1 + 0.74\nu_*\epsilon^{3/2}} F(x), \quad (4.5)$$

$$F(x) = \frac{1}{2\epsilon^{1/2}} \left\langle \frac{B_\varphi^2}{B^2} - 1 \right\rangle. \quad (4.6)$$

It is known, though, to overpredict the flux for $\epsilon \sim 0.1$ by up to 30% [48]. Since we will use this prediction also in future sections, we also provide the normalized version.

$$\hat{q}_{\text{CH},i} = \frac{16\sqrt{2}}{3\sqrt{\pi}} \hat{n}_i^2 Z^4 \hat{T}_i^{1/2} \hat{m}_i^{1/2} q^2 \epsilon^{-3/2} \sqrt{1 - \epsilon^2} K_2 \nu_c \hat{\omega}_T, \quad (4.7)$$

where we use the normalized temperature gradient length $\hat{\omega}_T = \frac{L_{\text{ref}}}{T_i} \frac{\partial T_i}{\partial \hat{x}}$. It should be noted that from this point on we will drop the \hat{x} notation and consider all quantities to be normalized according to the rules given in Sec. 3.3 unless explicitly stated.

In order to benchmark GENE with the three presented predictions we use local simulations with parameters given in Tab. 4.1. The numerical grid resolution used is

ϵ	R	q	\hat{s}	$\omega_n = a/L_{n_i}$	$\omega_T = a/L_{T_i}$
0.18	2.78	1.4	0.796	0.789	3.0

Table 4.1: Simulation parameters for local neoclassical benchmark (CBC-like, length scales normalized to $L_{\text{ref}} = a$)

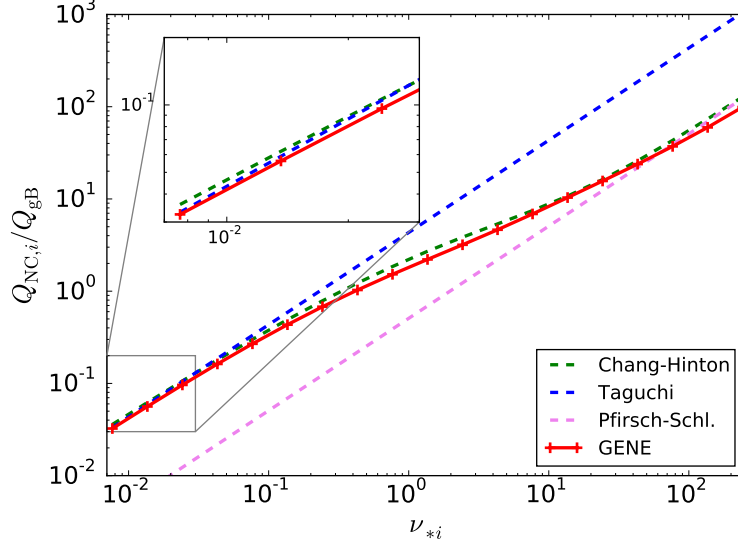


Figure 4.1: Neoclassical ion heat flux with adiabatic electrons compared to different analytical models.

$N_{k_x} \times N_{k_y} \times N_z \times N_{v_{\parallel}} \times N_{\mu} = 1 \times 1 \times 32 \times 96 \times 64$ with a velocity space box of $(l_{v_{\parallel}}, l_{\mu}) = (3.0, 9.0)$ (in normalized units). The geometry parameters and ω_{n_i} are based on the so-called *Cyclone Base Case* (CBC), a standard benchmarking scenario for gyrokinetic codes [50].

Fig. 4.1 shows the ion heat fluxes in the local neoclassical equilibrium over a wide range of collisionalities from the banana up to the Pfirsch-Schlüter regime. The simulation shows good agreement with the Chang-Hinton formula, yielding overall smaller values than the formula (see above). For small ν_* (inset in Fig. 4.1) we find better agreement with the more accurate Taguchi prediction. At very high collisionalities, on the other hand, a notable deviation occurs between simulation and the Pfirsch-Schlüter prediction. Collisions are the dominant process in this regime, so even very small imperfections of the numerical schemes of the collision operator start to matter. Since this high collisionality does not occur in almost all relevant fusion plasma applications, the deviation can be considered the result of a trade-off between accuracy and computational cost.

Summarily, the GENE results for local neoclassical simulations are reliable, especially, if we regard the more expansive benchmarks performed in Ref. [24].

4.2 Radially global simulations

When we expand our simulations to the global model, a number of interesting physical effects and with them also numerical challenges are introduced. Since the (almost) full radial domain is considered, the value of the inverse aspect ratio ϵ varies from values close to 0 up to the ratio $a/R_0 \sim 0.4$ for our typical cases. Additionally, with the introduction of temperature and density profiles the collision frequency is smaller in the inner region due to the usually higher temperature. This means that the value of ν_* can vary over several orders of magnitude.

In this work we initialize the background density and temperature profiles with an analytic ad-hoc function which takes either the peaked form

$$\omega_{n_0, T_0}(x) = \kappa_{n, T} \frac{\cosh\left(\frac{x - c_{n, T}}{w_{n, T}}\right)^{-2} - \cosh\left(\frac{c_{n, T}}{w_{n, T}}\right)^{-2}}{1 - \cosh\left(\frac{c_{n, T}}{w_{n, T}}\right)^{-2}}, \quad (4.8a)$$

$$\omega_{n_0, T_0}(x) = \kappa_{n, T} \cosh\left(\frac{x - c_{n, T}}{w_{n, T}}\right)^{-2}, \quad (4.8b)$$

with the former specifically used for $c_{n, T} = 0.5$ and the latter in all other cases, or the flat-top form

$$\omega_{n_0, T_0}(x) = \frac{1}{2} \kappa_{n, T} \left(\tanh\left(\frac{x - c_{n, T} + \delta_{n, T}}{w_{n, T}}\right) - \tanh\left(\frac{x - c_{n, T} - \delta_{n, T}}{w_{n, T}}\right) \right). \quad (4.9)$$

The safety factor profile is chosen to be:

$$q(x/a) = 0.854 + 2.239(x/a)^2 + 0.147(x/a)^4, \quad (4.10)$$

which reproduces q and \hat{s} of the CBC-like parameters at $x = 0.5a$. For a plot see “std q ” and “std \hat{s} ” in Fig. 6.9.

4.2.1 The radial electric field

One important additional physical effect that becomes tractable in global simulations is the neoclassical radial electric field E_r . As we will demonstrate in chapters 5 and 6, it is in fact the cornerstone of the interaction between neoclassical and turbulent phenomena. A fundamental test for the self-consistent calculation of this electric field is to employ the *radial force balance*:

$$ZeE_r = -\nabla_x p + (\mathbf{u} \times \mathbf{B})_x = -\nabla_x p + u_\varphi B_\theta - u_\theta B_\varphi, \quad (4.11)$$

which reflects conservation of toroidal angular momentum [43] and which we need to transform into our specific set of curvilinear coordinates. If the poloidal flow velocity is determined by neoclassical effects, it can be expressed in terms of the temperature gradient. The derivation can be found in Ref. [28] and the end result can be written normalized as:

$$\langle u_{\parallel \sigma} B \rangle = \frac{1}{Z_\sigma} \frac{B_\varphi}{B_\theta} n_\sigma T_\sigma \left(\omega_{n_\sigma} + (1 - k) \omega_{T_\sigma} + \frac{Z}{T_\sigma} E_r \right), \quad (4.12)$$

	c_1	c_2
Analytical	1.0	0.0
Dirichlet	0.52	0.39
von Neumann	0.97	0.01
vN, no $\mathbf{v}_d \cdot \nabla f_1$	0.98	-0.01

Table 4.2: Regression results for the force balance Eq. (4.14)

where the dimensionless parameter $k = k(\nu_*)$ was introduced. It was already predicted for the banana regime in Ref. [28] but in Ref. [51] a more generally valid estimate was found. Nonetheless, no exact function for k is known.

If, on the other hand, we assume a simpler system with constant temperature, the force balance equation reduces to a relation between parallel flow, radial electric field and the density gradient, all three readily measurable quantities:

$$\langle u_{\parallel\sigma} B \rangle = \frac{1}{Z_\sigma} \frac{B_\varphi}{B_\theta} n_\sigma T_\sigma \left(\omega_{n_\sigma} + \frac{Z}{T_\sigma} E_r \right), \quad (4.13)$$

or with the further assumption of only one ion species and no toroidal rotation ($u_{\parallel} \approx 0$):

$$E_r = -\frac{T_i}{Z_i} \omega_{n_\sigma}, \quad (4.14)$$

where we can set the normalized quantities to $T_\sigma = Z = 1$.

For our simulations we impose a background density gradient profile of the peaked form (4.8a), which has the advantage that it assumes the value 0 at $x = \{0, a\}$. The parameters are chosen to be $\kappa_n = 2.789$, $c_n = 0.5$ and $w_n = 0.15$. This is a rather narrow, peaked gradient profile since the field is sensitive to particle and momentum sources at the radial boundary, as we will show in the following.

With the predetermined gradient we can perform a linear regression for Eq. (4.14) in the form:

$$E_r = -c_1 \omega_{n_\sigma} + c_2. \quad (4.15)$$

In Fig. 4.2 and Tab. 4.2 we show the results of this regression for three different numerical setups.

In the first case (Fig. 4.2(a)), which uses the default Dirichlet radial boundary condition, i.e. $f_1|_{x_{\min/\max}} = 0$ and thus $\phi_1|_{x_{\min/\max}} = 0$, we find that our approach fails. This is not very surprising as a monotonic solution for ϕ_1 with boundary values 0 cannot exist. The system reacts to this by developing a (spurious) field in the near-axis region. Another interpretation would be that the inner Dirichlet boundary acts as a hardly controllable particle and momentum source near the magnetic axis. It is important to note that the full force balance (4.13) is still fulfilled: a considerable parallel flow profile develops.

If we choose the more physically appropriate von Neumann condition on the inner radial domain boundary, i.e. $\frac{\partial f_1}{\partial x}|_{x_{\min/\max}} = 0$, the linear regression yields parameters that agree very well with the analytical prediction (Fig. 4.2(b)). Minor deviations

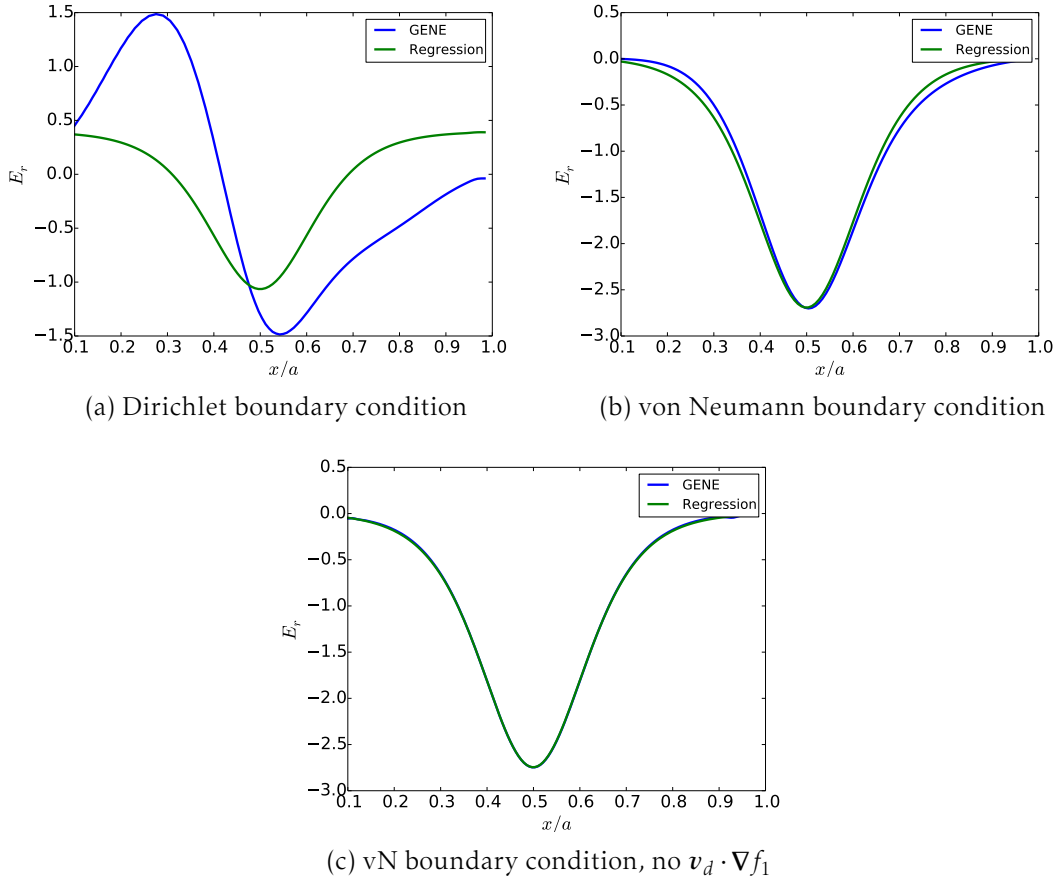


Figure 4.2: Radial electric field and possible fit to the density gradient profile

occur due to remaining small numerical momentum sources, whose contributions can accumulate over the long simulation time of several ion-ion collision times ($t = 5000$). An additional interesting test is to solve the neoclassical Vlasov-Poisson system with identical parameters but without the term $\mathbf{v}_d \cdot \nabla f_1$, i.e. Eq. (2.46). As can be seen in Fig. 4.2(c) the neoclassical radial electric field is still established in a global simulation that strictly enforces the neoclassical ordering.

In conclusion, we find that the correct choice of the radial boundary condition on the inside boundary is crucial for the calculation of the self-consistent neoclassical radial electric field. The Dirichlet condition is generally unsuited for long-wavelength phenomena ($k_x \rho \ll 1$). It also disturbs short-wavelength turbulence but only in a region of limited width at the edge of the simulation domain which usually is neglected.

4.2.2 The effects of potato orbits

After establishing the correct behavior of GENE in view of global simulations that cover both neoclassics and turbulence (see Chapter 6), we now study how nonlocality can fundamentally affect radial transport in purely neoclassical systems. Since both the local model as well as the standard neoclassical theory are based on the assumption that

R	ρ_*	ν_c	$c_{n,T}$	$w_{n,T}$	κ_n	κ_T
2.78	1/150	$3.863 \cdot 10^{-4}$	0.5	0.3	0.789	3.58

Table 4.3: Simulation parameters for global neoclassical benchmark (length scales normalized to $L_{\text{ref}} = a$)

the orbit width is small compared to magnetic field and/or background temperature and density gradient scales, global simulations are the logical choice to investigate situations where this does not hold. One such case appears in every tokamak: As described in Sec. 2.2.2 trapped drift orbits in the proximity of the magnetic axis can have a considerable radial extent. Accordingly, these orbits are given the name *potato* instead of banana orbit. Their region of relevance is estimated by the potato width Eq. (2.12) which we repeat here:

$$r_p = \sqrt[3]{4q^2\rho^2 R_0}.$$

Consequently, this also implies that the time scale separation between parallel (to the magnetic guide field) and perpendicular dynamics decreases. The boundary in collisionality between the banana/potato and plateau regimes is modified as well, as $\epsilon^{-3/2}$ in Sec. 2.2.2 is based on the assumption for the trapping fraction that $f_t \sim \sqrt{\epsilon}$ which is only valid for thin orbits - a possible expression for it in the potato region can be $f_t = (r_p/R)^{3/2}$.

Since transport phenomena in this region are nonlocal, it is important to understand that even if a diffusivity or heat conductivity is defined by dividing the radial fluxes by their respective gradient profiles, it merely becomes another way of expressing the flux [43, 52].

A particular property of our simulations is that they cannot include the archetypal potato orbit which exactly crosses the magnetic axis; the field aligned coordinate system becomes singular there so the numerical radial domain has to end a few ion gyroradii away from it. This is not a severe limitation as not many particles populate these specific orbits and the treatable paths that come close to the axis are physically very similar. Since the existing (semi-)analytical predictions for this region do not take the radial electric field into account, we also set the potential to zero.

As a first step we study a basic case where the gradient profiles of temperature have the peaked form of Eq. (4.8a) and the relevant parameters are as listed in Tab. 4.3. For these parameters we find a potato width of $r_p = 0.12a$. The collisionality profile $\nu_*(x)$ resulting from the choice of ν_c is well within the banana/potato regime, even when considering the previously mentioned modification to the boundary in the near-axis region. This is easily demonstrated when comparing $\nu_*\epsilon^{3/2}$ with the cubed trapping fraction f_t^3 in Fig. 4.3.

We compare the simulation results for the full (field-free) nonlocal drift-kinetic equation with both a Dirichlet and a von Neumann radial boundary and for its local counterpart that lacks the term $\mathbf{v}_d \cdot \nabla f_1$ and also does not include the gyroaverage operation (i.e. the drift-kinetic limit). As can be seen in Fig. 4.4, this additional term has almost no effect for radial positions beyond $x = 0.3 \sim 3r_p$. This is consistent with the

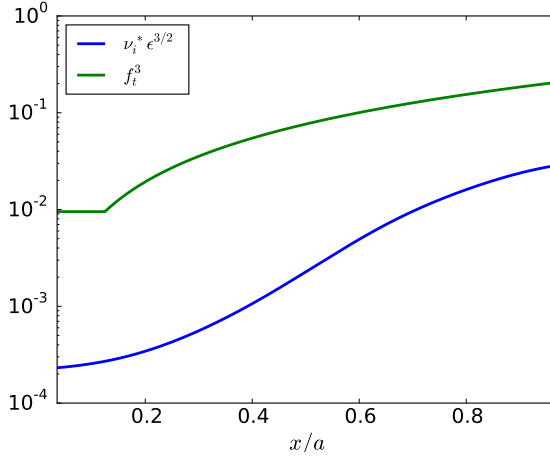


Figure 4.3: Collisionality and banana/potato-plateau boundary f_i^3 . (The Pfirsch-Schlüter regime begins at $\nu_* \epsilon^{3/2}$.)

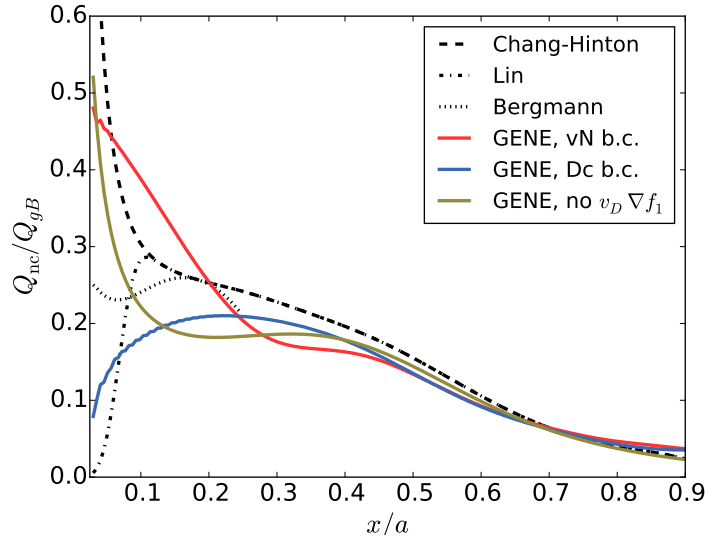


Figure 4.4: Radial heat flux profile for global neoclassical simulations with predictions for the potato region by Lin et al. [53] and Bergmann et al. [54]

fact that it is formally second order in the standard neoclassical ordering. Additionally, we find reasonable agreement with the Chang-Hinton formula. In the potato region, on the other hand, the simulations differ significantly. The numerical solution of the local-like drift-kinetic equation still follows the Chang-Hinton prediction and reproduces the singularity of the thin-orbit theory at the magnetic axis. The solution of the full equation in contrast seems to be strongly influenced by the choice of the radial boundary condition. The same qualitative result as for the Dirichlet boundary was found in Ref. [43]. The von Neumann boundary seems to result in a higher heat flux than the local prediction but has a decreasing slope so that it should not diverge at the magnetic axis.

In addition to the simulation results, we present a number of analytical approaches

were made to treat neoclassical transport in the wide-orbit region for the banana/potato and plateau collisionality regime⁸. In the banana/potato regime Ref. [53] (marked as “Lin” in Fig. 4.4 to 4.6) predicts a strong reduction of the heat flux near the axis of the form:

$$Q_{\text{nc}}/Q_{\text{CH}} = 1 - e^{-(x/r_p)^3} (1 + (x/r_p)^3), \quad (4.16)$$

i.e. zero flux at the magnetic axis. We are using the Chang-Hinton formula as the reference for the prediction of standard (thin-orbit) neoclassical theory here. Ref. [55] on the other hand states that, while no longer a random walk process in x , transport remains one in the poloidal flux ψ . Since the circular geometry provides $\frac{d\psi}{dx} = xB_0/\bar{q}$ (where $\bar{q} = q\sqrt{1-\epsilon^2}$), it is indeed possible to have small steps in ψ corresponding to large changes in x . The result of Ref. [55] is an enhancement of the banana heat flux by:

$$Q_{\text{nc}}/Q_{\text{CH}} \sim \sqrt{r_p/x}, \quad (4.17)$$

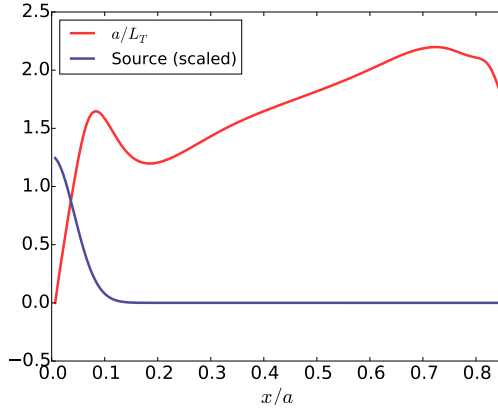
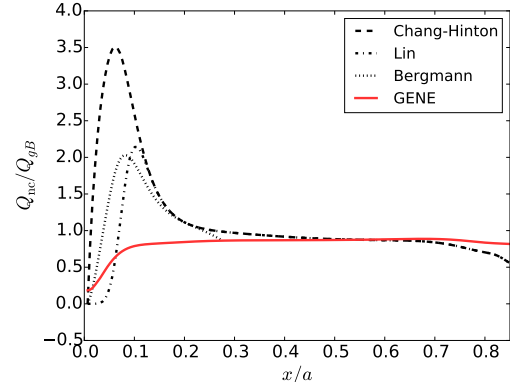
which is problematic as it does not resolve the singularity of the standard theory at the magnetic axis. Ref. [52] criticizes both works, pointing out certain hard to justify assumptions. Ref. [54] (marked as “Bergmann” in Fig. 4.4 to 4.6) tests these predictions numerically and empirically finds a modification of the heat flux by:

$$Q_{\text{nc}}/Q_{\text{CH}} = 1 - (1 - x/3r_p)^2, \quad (4.18)$$

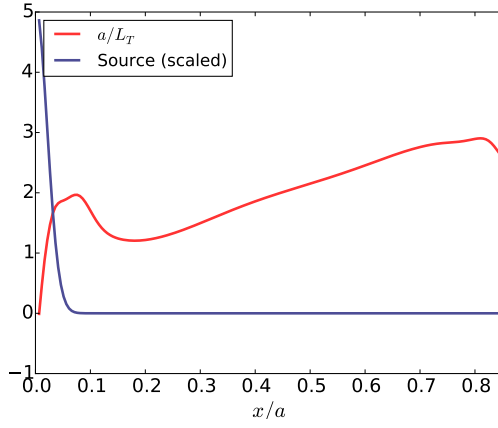
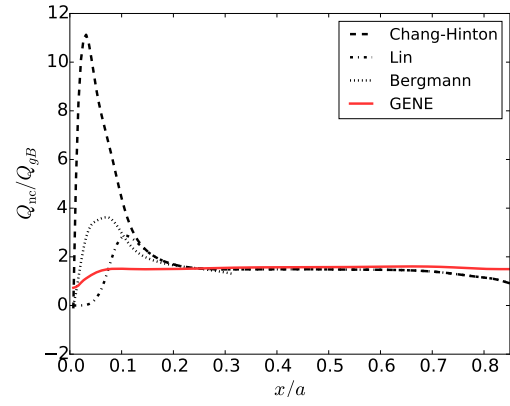
thus being qualitatively closer to the prediction of Ref. [53]. For the potato regime both Ref. [52] and Ref. [56] reach the conclusion that the prediction of standard neoclassical theory remains valid although they disagree in the method of derivation.

As can be seen in Fig. 4.4, we do not find strong quantitative agreement with any of these predictions for our simulations. Qualitatively we can agree the most with Ref. [54]. The strong dependency on the boundary condition and the necessity for relatively strong Krook-type heating to keep the temperature profile constant hint that the observed difference could be due to numerical artifacts. In order to address this we turn to a different approach: Based on the argument made in Ref. [52] that an analysis of the potato regime should also include the energy source, we perform flux-driven simulations with a localized heat source employing the resetting mechanism described in Sec. 3.4.2. The threshold for f_1/F_0 is 0.08. In the region $x/a > 0.9$ a Krook-type buffer zone serves as a smooth energy sink. For the geometry we now choose a major radius of $R = 5a$ in order to make the potato width slightly wider ($r_p = 0.15 - 0.18$ depending on the temperature profile evolution) and to achieve a much bigger collisionality interval in the plateau region. When we use $\nu_c = 3.863 \cdot 10^{-3}$ (as we will in the following) the entire radial domain has a collisionality on the very upper border of the potato regime. The scale parameter is kept at $\rho_* = 1/150$. For the density we assume a flat profile, which does not evolve in time. The initial state of the temperature gradient profile is like given in Tab. 4.3 but evolves according to the heat source. The simulations now require a run time not only several collision times long to reach a steady state but about a neoclassical confinement time ($\sim 10^5 a/c_{\text{ref}}$). Fortunately, neoclassical computations only require

⁸The Pfirsch-Schlüter regime does not have undisrupted orbits so their width becomes irrelevant. The near-axis tokamak core is also the hottest part of a fusion plasma, so collisionality will be low.


 (a) Source on axis: ω_{T_i} and source


(b) Source on axis: heat flux


 (c) Narrow (half width) source on axis: ω_{T_i} and source


(d) Narrow source (half width) on axis: heat flux

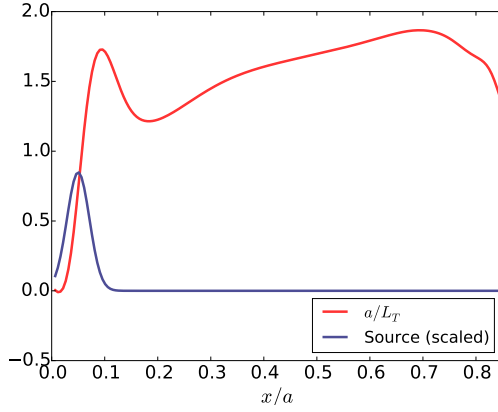
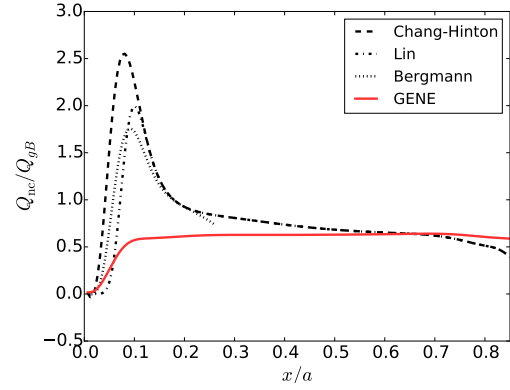

 (e) Source off axis ($x = 0.05$): ω_{T_i} and source

 (f) Source off axis ($x = 0.05$): heat flux

Figure 4.5: Effects of varying source profile on flux-driven neoclassical equilibria. Source amplitudes are scaled to arbitrary units. Predictions for the potato region are by Lin et al. [53] and Bergmann et al. [54].

solving the linear part of the gyro-/drift-kinetic equation, so computational cost is still at least one, but rather two orders of magnitude smaller than for the turbulent systems presented in Chapter 6.

In Fig. 4.5 we present the results for simulations where we keep the total input power, i.e. the volume integral of the source constant ($\hat{S}_0 = 1000$) but vary either its width (Fig. 4.5(c) and (d)) or its position (Fig. 4.5(e) and (f)).

Far away from the magnetic axis (e.g. at $x/a = 0.5$) we consistently find in all three cases that the heat flux agrees well with the Chang-Hinton prediction. However, both temperature gradient and transport have a higher value for the narrow source than in the other two cases. A possible explanation is that the very close boundary and the finite radial resolution affect the normalization of the power input for the narrow source profile resulting in a slightly higher power input.

In the region near the axis - and the source - the heat flux in all three cases (Fig. 4.5(b), (d), (f)) is smaller than the predictions we have presented. Since these all derive their value at a certain radial position on the temperature gradient (and quite strongly the local aspect ratio) at this position, their overestimate gives a strong indication of the nonlocal nature of transport there. The temperature gradient in each case (Fig. 4.5(a), (c), (e)) develops a distinct peak at the edge of the source region before reaching a local minimum at the potato radius, $x \approx 0.17$, and then monotonically increases until the outer sink region shows its influence. For the narrow source (Fig. 4.5(c)) the profile shape suggests that the observed peak is actually two overlapping maxima - one at the edge of the source, the other at about half the potato width. In the other two cases both positions coincide and possible effects of the source and the potato region are hard to separate. Fig. 4.6(a) and (b) demonstrate the effect of a power input increased by the factor 1.5: The neoclassical heat flux scales accordingly while the temperature gradient does not increase as much. Since the Chang-Hinton prediction based on this gradient widely agrees with the measured heat flux, this behavior appears to be consistent with the standard neoclassical model. The observations about shape of the gradient and transport profiles made for Fig. 4.5(a) and (b) on the other hand still hold. If we reduce the collisionality from borderline plateau to deeply within the banana/potato regime, the qualitative behavior of the heat flux profile in Fig. 4.6(d) is similar to the previously shown results as should be expected for equal power input. The temperature gradient (Fig. 4.6(c)), however, is significantly different: The maximum-minimum-monotonic growth radial dependence is still existent but much stronger pronounced and with a larger radial extent. A possible explanation would be the stronger dependency of the heat conductivity on the collisionality in the banana regime compared to the plateau and the according need for the temperature gradient to adapt to this. The position of the minimum is now at approximately $2r_p$. At the edge of the source region we find a change in the slope of the gradient profile reminding of the earlier conjecture of a double peak. The maximal gradient is at $x/a \sim 0.12$, about two thirds of the potato width.

These results demonstrate that new insights into neoclassical transport near the magnetic axis can be gained when the kinetic problem is solved taking a (controlled) source term into account. In particular, the potato width r_p appears to determine certain characteristics of the self-consistent temperature gradient profile. There are, however, many open questions left and more research is necessary to arrive at satis-

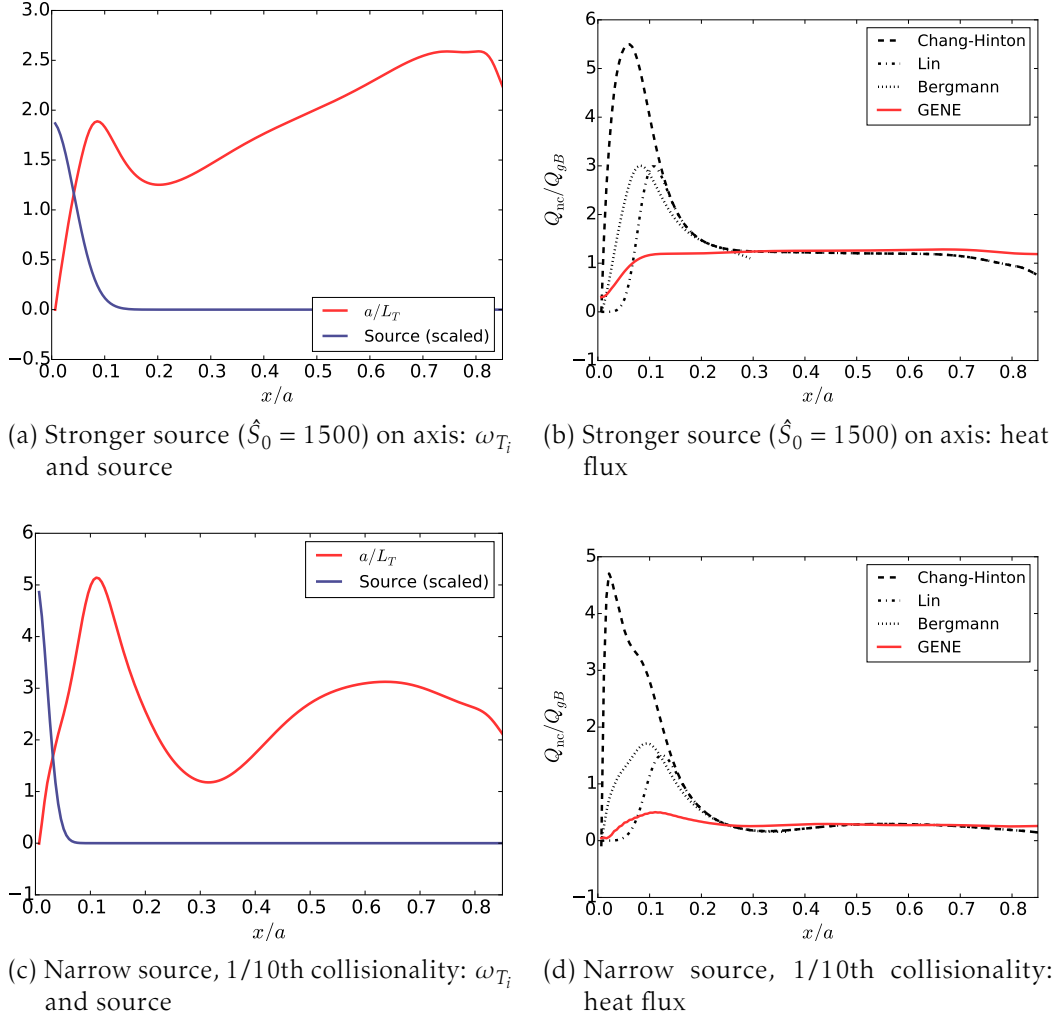


Figure 4.6: Effects of stronger source and lower collisionality on flux-driven neoclassical equilibria. Source amplitudes are scaled to arbitrary units. Predictions for the potato region are by Lin et al. [53] and Bergmann et al. [54].

fying explanations for the observed behavior and at quantitative predictions for the implications of wide drift orbits.

4.3 Summary

In this chapter the GENE code was used to perform simulations of purely neoclassical effects by solving only for the $k_y = 0$ mode of the linear drift-kinetic equation. First, it was reconfirmed that GENE is able to provide good estimates of the radial neoclassical heat flux over a wide range of collisionalities in local simulations by comparing with established analytical results. Secondly, it was demonstrated that the radially global version of the code is able to self-consistently calculate the neoclassical radial electric field which obeys the radial force balance equation. In this context the importance of

choosing a physically sound (von Neumann) boundary condition at the inner edge of the radial domain has been demonstrated.

Lastly, the role of so-called potato orbits for transport near the magnetic axis has been investigated. It was shown that the term $\mathbf{v}_d \cdot \nabla f_1$ in the Vlasov equation is necessary to cover these finite-orbit-width effects and the heat fluxes were compared with a number of predictions from previous analytical and numerical works. Based on the unsatisfying match of the fluxes and an observed strong influence of the radial boundary condition and adaptive heat source even without an electrostatic potential flux-driven simulations were also performed. There, a localized power source allows the fluxes and temperature to evolve into a self-consistent state. The simulations confirmed the nonlocality of neoclassical transport in the potato region. Additionally, the data indicated that the potato width r_p provides a relevant scale length for the self-consistently evolved ion temperature profile. These findings form a good basis for research work beyond this thesis.

In the following chapter the successful calculation of the radial electric field will serve as a motivation to study the effects on turbulence in flux-tube (local) simulations when a slowly varying long-range electric field akin to the neoclassical one is present.

Chapter 5

Effects of non-turbulent electrostatic fields on ITG turbulence

In Sec. 4.2.1 it was demonstrated that neoclassical effects provide a sheared electrostatic field in global simulations. Due to the mechanisms of turbulence in magnetically confined plasmas, which shall be elaborated on in the following, this radial electric field is a prime candidate for an interaction mechanism. As an intermediate step before investigating this in radially global simulations of turbulence including neoclassical effects the impact of additional $E \times B$ shear in local simulations is studied. The lower simulation cost of local simulations (roughly one order of magnitude less CPU time) allows us to do more systematic parameter studies and the periodic radial boundary conditions simplify the overall simulation setup and analysis of the resulting data. Since electrons are considered adiabatic, the radial particle fluxes are exactly 0 and the quantity of main interest is the turbulent transport of heat/energy.

5.1 Turbulence saturation by zonal flows

For these studies in the flux-tube limit we use a simple case of ion temperature gradient-driven (ITG) turbulence, a form of drift-wave turbulence [57], with adiabatic electrons in the usual circular equilibrium. The behavior of such a system has been studied thoroughly in the past and it is an established finding that the growth of unstable turbulent modes saturates by self-generated shear flows, so-called *zonal flows* [58]. Shape-wise, zonal flows in a tokamak are toroidally and poloidally symmetric structures with finite but small radial wavenumbers. Their damping effect can be understood descriptively in the form that they tilt and shear apart the turbulent eddies. The basic mechanism in terms of free energy can be described in the following way:

- The temperature gradient provides a source of free energy.
- Microinstabilities (so-called drift waves) tap into this reservoir to grow.

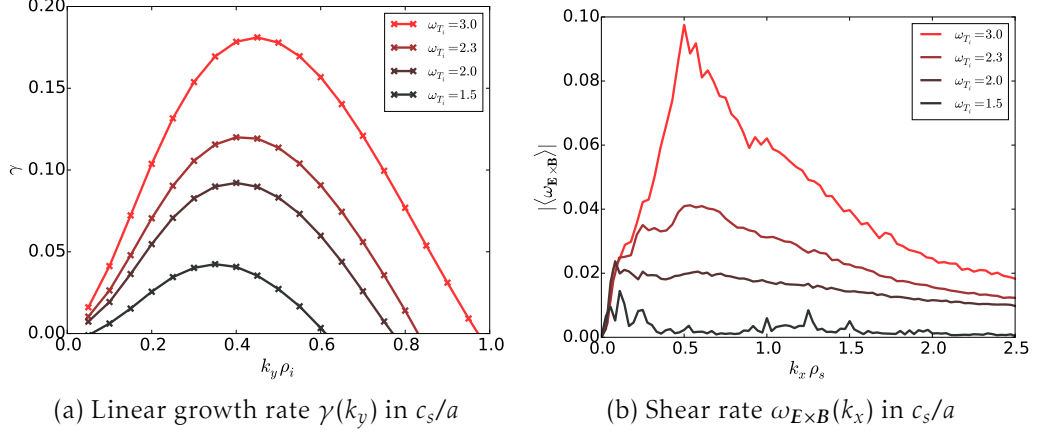


Figure 5.1: Linear growth rate and non-linear time-averaged $E \times B$ shear rate spectra for ITG turbulence

- The zonal flow mode can only access the energy in the drift wave thus damping it and in consequence limiting its own growth.
- Dissipation, e.g. Landau damping and collisions, removes free energy from the system.

The last item introduces an additional dependency: Increased collisionality dampens zonal flows and thus tends to increase the turbulent transport [59]. It is also important to note that zonal flows are a purely nonlinear effect: They are linearly stable $n = m = 0$ components⁹ of the fluctuating electrostatic potential ϕ_1 driven by the distribution function perturbation f_1 .

The reference setup for our simulations in this chapter are CBC-like parameters (see Tab. 4.1), where we vary the ion temperature gradient between values of $\omega_{T_i} = 2.0, 2.3, 3.0$. The numerical grid used is $(N_{k_x}, N_{k_y}, N_z, N_{v_{\parallel}}, N_{\mu}) = (192, 32, 32, 32, 20)$ with a radial domain size of $l_x = 175\rho_i$ and $l_x = 226\rho_i$ for the low temperature gradient, respectively. These relatively large boxes are required to observe the zonal flow pattern on higher radial modes than $k_{x,\min} = 2\pi/L_x$.

In a first step we only solve the linear system and measure the spectrum exponential growth rates $\gamma(k_y)$ which occurs without the nonlinear damping mechanism. This gives an indication how strong the system is driven and at which length scale the strongest. As can be seen in the spectrum Fig. 5.1(a) the peak linear growth rate for the reference system occurs at a wavenumber of $k_y \rho_i = 0.35 - 0.45$ with a tendency to lower wavenumbers for small gradients. Its value (see Tab. 5.1) depends strongly on the temperature gradient which is very characteristic for the turbulent system at hand [57].

It is clear that this growth needs to be balanced by a damping mechanism of similar strength for a quasistationary result if the nonlinear full Vlasov equation is solved. Since the primary damping effect in our system are $E \times B$ shear flows, we expect a

⁹ n and m are the toroidal and poloidal mode numbers, i.e. as stated before the zonal mode is toroidally and poloidally symmetric.

ω_{T_i}	γ_{\max}	$\sqrt{\omega_{E \times B}^2}$	$\overline{Q_{\text{turb}}}/Q_{\text{gB}}$
3.0	0.18	0.67 ± 0.01	10.7 ± 0.3
2.3	0.12	0.37 ± 0.01	5.2 ± 0.1
2.0	0.09	0.25 ± 0.01	3.3 ± 0.1
1.5	0.04	0.05	0.02 ± 0.002

Table 5.1: Dependency on the temperature gradient of ITG simulations (errors according to Sec. 3.5.3, growth rate and $\mathbf{E} \times \mathbf{B}$ shear in units of c_s/a)

shearing rate $\omega_{E \times B}$ of a similar magnitude to the growth rate. In fact, since shear flows that are shorter-lived than the turbulent eddies provide no effective damping, the time averaged root mean square shearing rate is usually several times bigger, as can be seen in Tab. 5.1. Ref. [60] derives an expression for an efficient $\mathbf{E} \times \mathbf{B}$ shearing rate based on the ratio between the eddy decorrelation rate and the fluctuation frequency of the flux-surface averaged electrostatic potential $\langle \phi(k_x) \rangle$. Unfortunately, it is difficult to find a robust estimate for this ratio, since correlation estimators tend to be biased and ϕ actually contains a frequency spectrum. Nonetheless, the conclusion of Ref. [60] is that the small k_x components of the shear rate contribute considerably stronger to turbulence damping than their shorter-wavelength counterparts. This means that the components $k_y \rho_i \gtrsim 1$ of the shear rate spectrum in Fig. 5.1(b) are almost irrelevant for the saturation of turbulence. It also implies that temporally (nearly) constant shearing rates such as the one from the neoclassical field or an externally imposed one will have a stronger effect compared to their amplitude. The lowest gradient of $\omega_{T_i} = 1.5$ is a special case: While the linear simulation still finds unstable modes, its nonlinear counterpart results in practically zero turbulent heat transport and a very small $\mathbf{E} \times \mathbf{B}$ shearing rate. This difference in behavior between linear and nonlinear case is the so-called *Dimits shift* [50] and is specifically caused by the presence of zonal flows; notably growth rate and $\mathbf{E} \times \mathbf{B}$ shear rate are nearly equal. Since collisions dampen zonal flows, the borders of this gradient range become less pronounced in collisional simulations (*Dimits shift softening* [59, 61]).

Further insight into zonal flows can be gained by studying the time evolution of the flow patterns. In Fig. 5.2 we show the typical behavior of the flux-surface averaged electrostatic potential as a function of radial coordinate and time. All three temperature gradient amplitudes share two important features: Firstly, large scale ($20 - 50 \rho_i$) structures remain mostly constant in time for several hundreds of time units but occasionally change their position in a rapid fashion. These changes occur much more rarely in the case of weak turbulence (note the different time scales in Fig. 5.2). The shifts of the zonal flows are coupled to the second feature: a fine structure of diagonal ripples. These represent the turbulent fluctuations which move into a direction determined by the sign of the local shear. Since the turbulence drive gets weaker from Fig. 5.2(a) to 5.2(c) they become less pronounced in the latter. We will elaborate on this pattern of *avalanches* and a $\mathbf{E} \times \mathbf{B}$ *staircase* [62] in the context of global, especially flux-driven, simulations in Chapter 6. The nature of the local model - fixed constant mean gradients and periodic radial boundary conditions - prevents them from

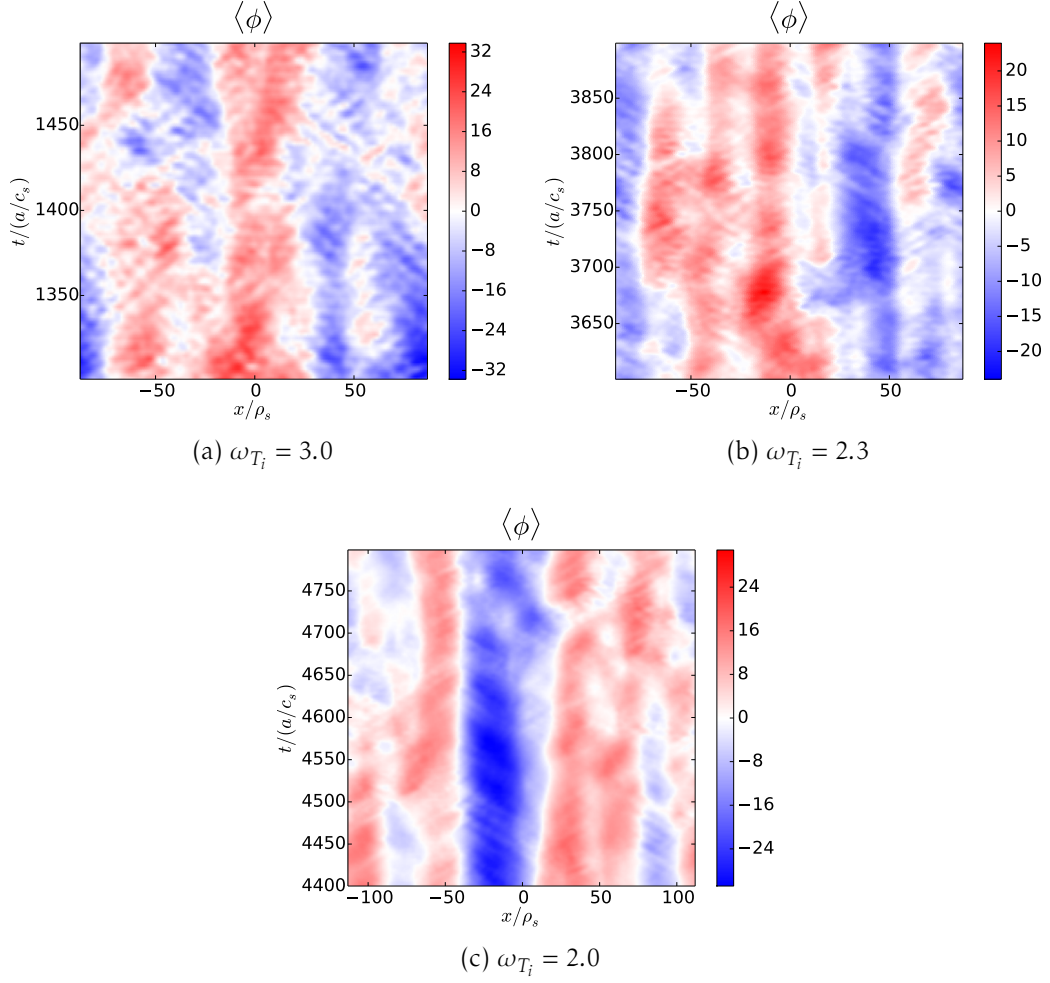


Figure 5.2: Spatio-temporal behavior of the intrinsic flux-surface averaged electrostatic potential: zonal flow patterns

being a defining effect of the system here.

The next step is now to expose such a system of ITG turbulence and zonal flows to additional shear of the likeness of but not limited to what the neoclassical electric field in global simulations can provide.

5.2 Effects of long wavelength external potentials

Since it is impossible to calculate the neoclassical radial electric field in local simulations (see Sec. 2.3.7), we have to find a way of modeling it. Even if the former was possible, it would be the $(k_x, k_y) = (0, 0)$ Fourier component, hence constant and we would only expect notable effects, when E_r is strong enough to modify the topology of drift orbits [52, 63]. Consequently, in order to approximate a system where the scales of turbulence and neoclassical field are not entirely disjunct we choose to impose an external potential

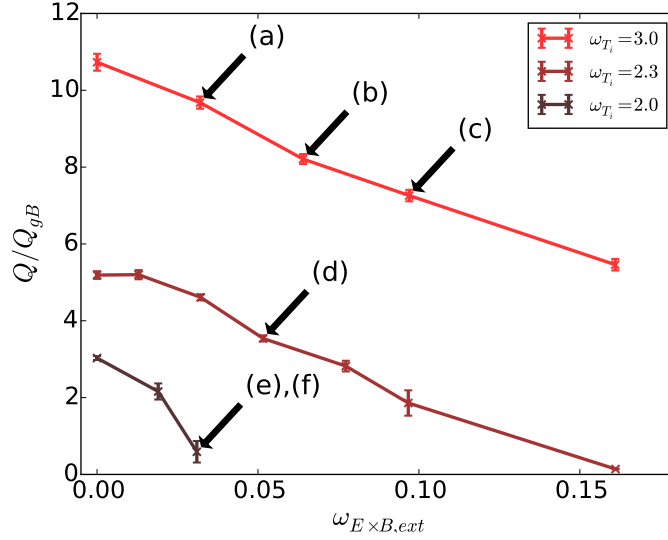


Figure 5.3: Turbulent heat flux reduction by external $E \times B$ shear ($k_{\text{ext}} = k_{x,\text{min}}$). Annotations refer to Fig 5.4.

of the following form:

$$\phi_{\text{ext}}(x) = \phi_0 \sin(k_{\text{ext}}x + \delta_{\text{ext}}), \quad (5.1)$$

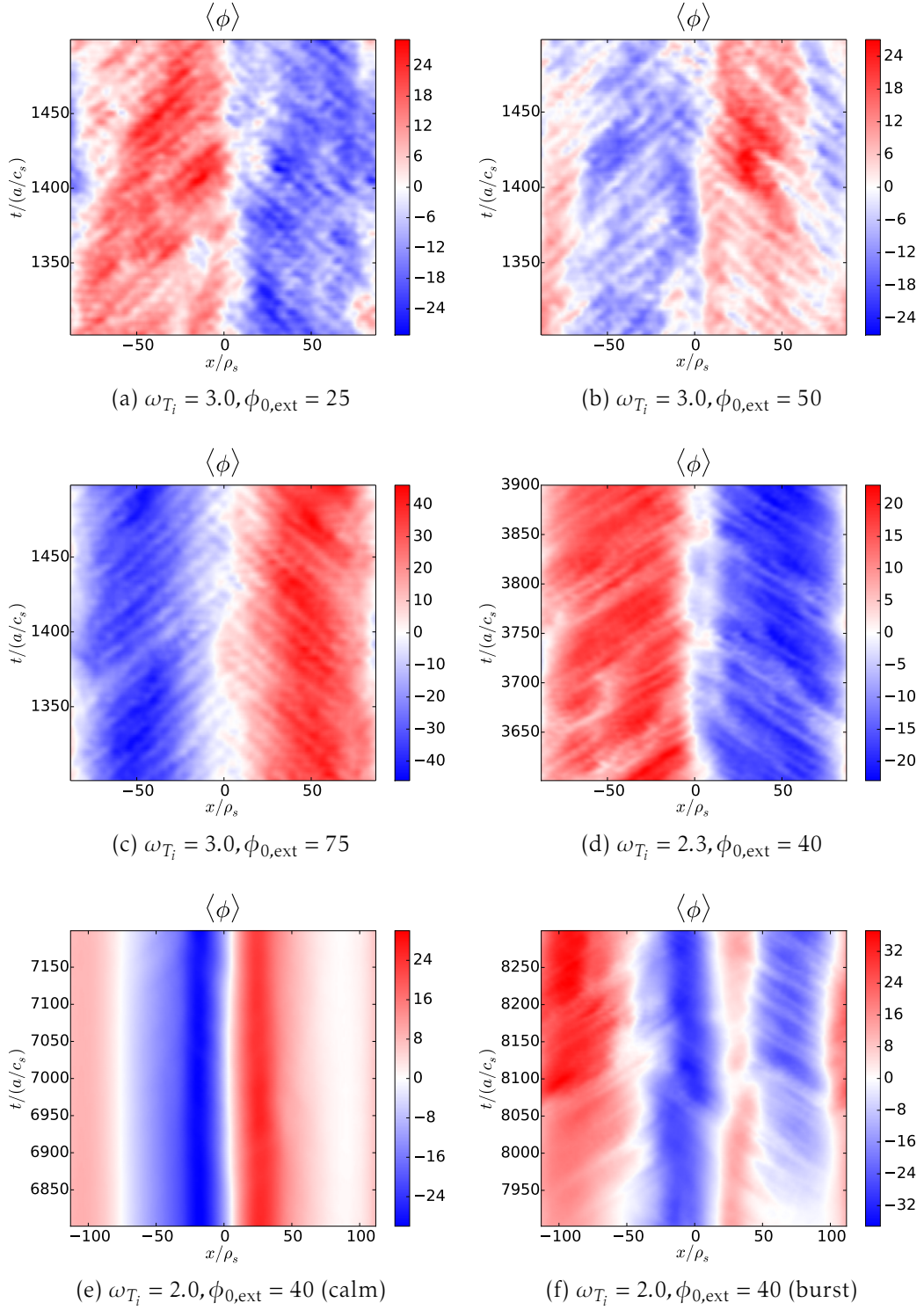
$$\tilde{\phi}(k_x) = \begin{cases} \mp \frac{i}{2} \phi_0 e^{\pm i \delta_{\text{ext}}} & \text{for } k_x = \pm k_{\text{ext}} \\ 0 & \text{for } k_x \neq \pm k_{\text{ext}}, \end{cases} \quad (5.2)$$

where the tilde denotes a Fourier transformed variable. This field imposes an additional (temporally) static shearing rate on the system:

$$\omega_{E \times B, \text{ext}} = \frac{\partial^2 \phi}{\partial x^2} = k_{\text{ext}}^2 \tilde{\phi}. \quad (5.3)$$

Simulations are initially started without the external field until a saturated state is established; at this point the system can adapt to the additional shear more quickly and a new steady state is reached. Since we are mainly concerned with long wavelength radial electric fields, we focus on the lowest possible wavenumber for k_{ext} , $k_{\text{ext}} = 2\pi/L_x$.

As can be seen in Fig. 5.3 the system behaves in the expected way: Additional shear reduces the turbulent radial heat flux. Most noteworthy, a relatively small external shear of e.g. 10% of the intrinsic shear rate (see Tab. 5.1) is enough to cause a reduction of the flux by 25% for $\omega_{Ti} = 3.0$. For weak turbulence drive ($\omega_{Ti} = 2.0$) this becomes dramatic enough to almost completely suppress turbulent activity. In fact, transport in this case mainly occurs in the form of intermittent bursts (also giving rise to a larger uncertainty for the mean flux). These observations confirm the conjecture made in the previous section that a static $E \times B$ shear is damping turbulence more effectively than its self-generated fluctuating zonal flow patterns. Obviously, Ref. [60] consistently gives $\omega_{\text{eff}} = \omega_0$. It is also be found that a spatially constant shearing rate results in a similar reduction if it is equal to the root mean square average of the sinusoidal rate.


 Figure 5.4: Total $\langle \phi \rangle$ patterns for an external potential with $k_{\text{ext}} = k_{x,\text{min}}$

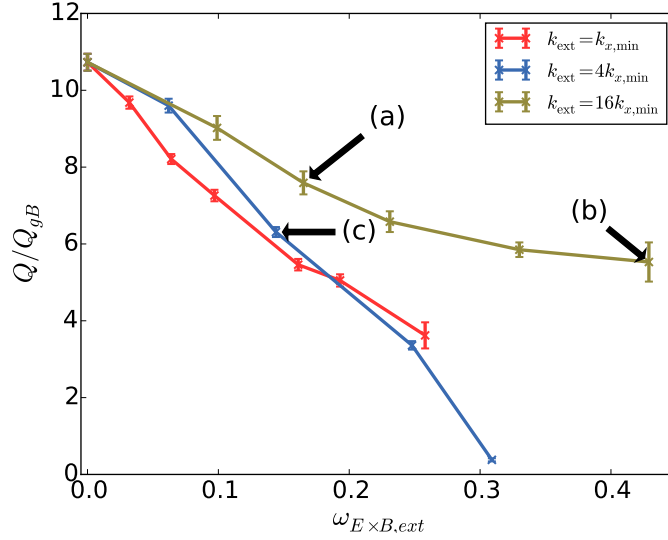
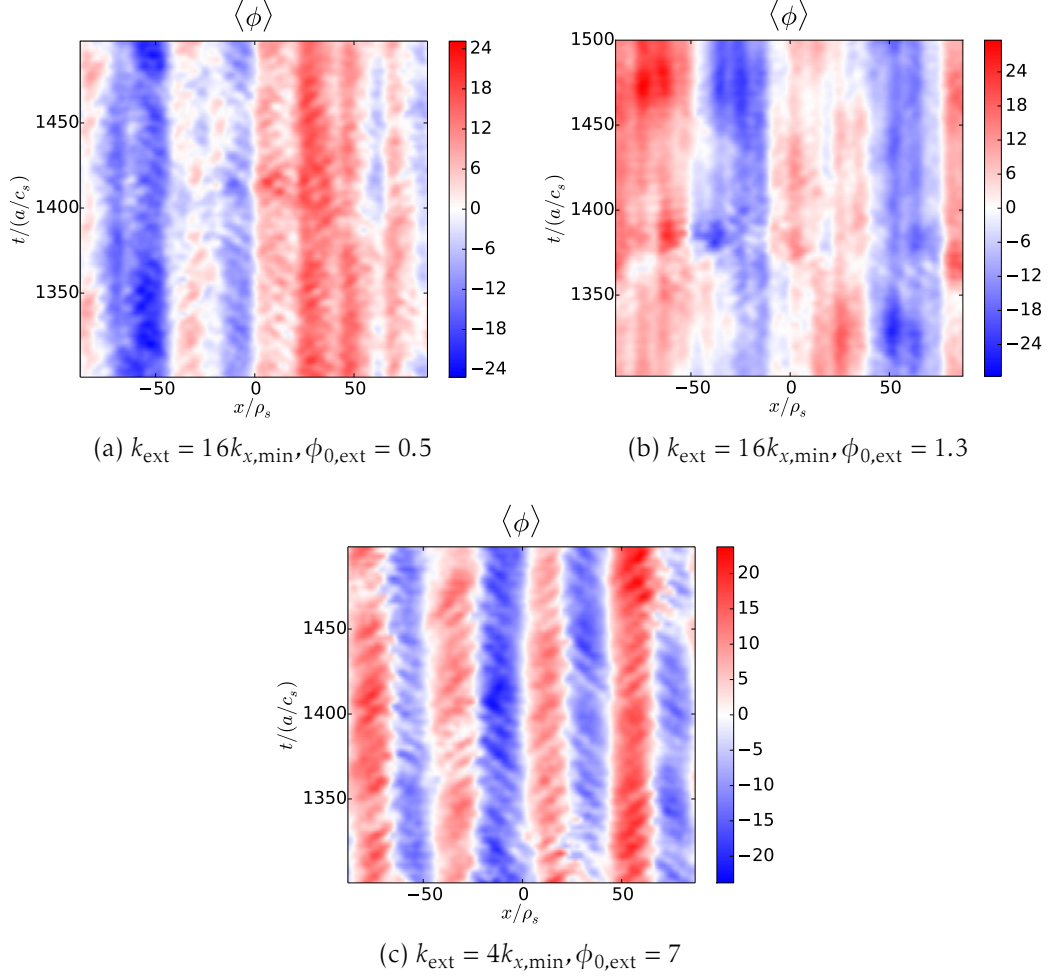


Figure 5.5: Turbulent heat flux reduction by external $E \times B$ shear ($\omega_{T_i} = 3.0$). Annotations refer to Fig .5.6

The variation of the external field and hence the shear rate over the radial domain has interesting effects, though. As can be seen for the time dependency of the total (intrinsic + external) potential in Fig 5.4, the system adapts to the externally introduced pattern: The intrinsic potential tries to shield the external one in order to reach a state where their total amplitude is similar to the unperturbed system. If the external field is weak enough it is overcompensated by the internal one as in Fig. 5.4(a) leading to a pattern of inverse sign compared to the imposed potential of Eq. (5.1) with $\delta_{ext} = 0$. When the external amplitude increases this becomes no longer possible (Fig. 5.4(b)) and the total amplitude is reduced. Finally, an even larger $\phi_{0,ext}$ means that the potential structure is dominated by the external field as in Fig. 5.4(c).

All three cases (Fig. 5.4(a)-(c)), however, have in common that the radial position of the shear flows is determined by the external source. While Fig. 5.4(a)-(c) only cover 200 time units, they are representative for the entire simulation time as soon as adaption to the external field has occurred. This is a distinctly different behavior than in the undisturbed case in Fig 5.2(a), but the periodic boundary conditions and the constant background gradient imply that the position of the shear flows will hardly affect the turbulent fluxes. For weaker ion temperature gradients the phenomenon becomes less pronounced: While $\omega_{T_i} = 2.3$ (Fig. 5.4(d)) still robustly positions the potential pattern on k_{ext} , the very weak turbulence of $\omega_{T_i} = 2.0$ does not. When almost no turbulent transport occurs (Fig. 5.4(e)), we find partial shielding of the external potential. A burst of turbulent activity (Fig. 5.4(f)), on the other hand, is characterized by a clear deviation from the imposed pattern. This could possibly be related to the larger eddy sizes of weak turbulence - compare the growth rate peaks in Fig. 5.1(a) - which makes the zonal flow pattern appear narrower and easier to move across for them.

The role of the external field's length scale can be studied directly by choosing higher wavenumbers for k_{ext} . We study the cases $4k_{x,min}$ and $16k_{x,min}$ for the strongly

Figure 5.6: Total $\langle \phi \rangle$ patterns for $\omega_{Ti} = 3.0$ with varying k_{ext}

turbulent system with $\omega_{Ti} = 3.0$. In Fig. 5.5 their turbulent heat flux is compared to the result for previous case of $k_{\text{ext}} = k_{x,\text{min}}$ when the external $E \times B$ shearing rate amplitude is comparable.¹⁰

We find that external shear rate patterns with higher wavenumbers are considerably less effective in damping ITG turbulence. The systems with $k = 16k_{x,\text{min}}$ even reach a state where the turbulent flow only weakly depends on the external shear before it abruptly vanishes at $\omega_{E \times B \text{ext}} \approx 0.55$ (not shown in Fig. 5.5). The intermediate case of $k = 16k_{x,\text{min}}$ is also less effective for low shear rate amplitudes but quickly becomes comparable to the minimal wavelength case. The time-resolved analysis of the potential in Fig. 5.6 helps to explain this behavior. Both in Fig. 5.6(a) and (b) the zonal potential pattern only partly adapts to the externally imposed structure. It is apparent that the turbulent fluctuations can move across the underlying potential modulation, especially in its weaker form in Fig 5.6(a). Fig. 5.6(b) has even some resemblance to the

¹⁰The external potential, in fact, acts on the gyrocenters - it does not contain a gyroaverage. Hence, the $16k_{x,\text{min}}$ case has a slightly larger amplitude in particle space.

unperturbed weakly driven situation of Fig. 5.2(c). On the other hand, $k_{\text{ext}} = 4k_{x,\text{min}}$ in Fig. 5.6(c) produces a regular 4-periodic potential structure. It still contains occasional bursts that go across the pattern, though. This could explain why $k_{\text{ext}} = 4k_{x,\text{min}}$ is less effective in turbulence damping at smaller amplitude.

Finally, we investigate a system with $\omega_{T_i} = 3.0$ and $k_{\text{ext}} = k_{x,\text{min}}$ again, where we choose a special value for the magnetic shear: $\hat{s} = 0$. This parameter is of particular interest because enhanced confinement scenarios in experimental tokamaks often have regions with very low or even negative magnetic shear. Specifically there - in internal transport barriers - the turbulence can become suppressed [64]. The magnetic shear is not the only ingredient of such a barrier, though. In our simulations we find that the turbulent ion heat flow is systematically smaller than for CBC-like shear by around 20%. This is consistent with the observation of a maximum of the ITG linear growth rate at $\hat{s} \sim 0.6$ [65, 66]. The impact of external $\mathbf{E} \times \mathbf{B}$ shear is very similar to the behavior shown in Fig. 5.3; we find a flux that is 20-25% smaller than the $\hat{s} = 0.796$ case for all external field amplitudes.

5.3 Summary

In this chapter local simulations were used to systematically study the effect of long-wavelength $\mathbf{E} \times \mathbf{B}$ shear on ion temperature gradient driven (ITG) turbulence and the zonal flow pattern connected to it. It was demonstrated that a sinusoidal external electrostatic potential can reduce the radial turbulent heat flux. It is also more effective at turbulence damping than the self-generated fluctuating zonal potential. Furthermore, it was shown that the intrinsic flow pattern accommodates and adapts to the imposed structure. This is less pronounced for turbulence closer to the marginal state, though. External potentials with shorter radial wavelength are found to be less effective to suppress turbulence compared to the lowest wavenumber in the system because eddies can move across the flow pattern.

Since the neoclassical radial electric field in global simulations establishes a similar long wavelength $\mathbf{E} \times \mathbf{B}$ shear pattern, these observations motivate a possible interaction mechanism for turbulence and neoclassical effects in global simulations which will be investigate in the following chapter.

Chapter 6

Synergy between turbulence and neoclassical effects

After successfully establishing a possible interaction mechanism between ITG turbulence and neoclassical effects by means of the local model, this concept can be put to the test in global simulations that include both effects. Such work is particularly facilitated by the fact that GENE as a δf code allows to selectively remove neoclassical effects by suppressing the term $v_d \cdot \nabla F_0$ in the Vlasov equation. We will refer to this term as the *neoclassical source* in the following. For simplicity, the simulations in this chapter all include only one ion species (hydrogen) and treat the electrons in the adiabatic limit. As a consequence no radial particle transport occurs both in the turbulent and neoclassical channel and the focus is put on the radial ion heat transport.

First, systems are investigated where the background temperature and density profiles are kept constant by an adaptive heating, then the more realistic but also more costly model of a self-consistent profile evolution according to a fixed power input is used. For the numerical methods employed see Sec. 3.4.1 and Sec. 3.4.2, respectively. Adhering to the observations of Sec. 4.2.1 a von Neumann boundary condition on the inner radial boundary is used. All simulations in this chapter have length scales normalized to the minor radius a and employ a circular geometry with a major radius $R_0 = 2.78a$. The minor radius serves as the reference length L_{ref} (see Sec. 3.3).

6.1 Gradient-driven setups

The role of neoclassical effects in systems with fixed gradient profiles have been previously studied with the ORB5/NEMORB [67] code in Ref. [61]. Based on the notion that neoclassical effects are inherently connected to collisions, noncollisional and collisional turbulence simulations are compared. The central result for the heat diffusivity χ is that

$$\chi_{\text{tot}}(v_*) > \chi_{\text{turb}}(v_* = 0) + \chi_{\text{NC}}(v_*). \quad (6.1)$$

For a qualitative explanation of this it is, however, not necessary to involve neoclassical effects: Collisions themselves dampen zonal flows and hence can increase the level of turbulent transport [58](see Sec. 5.1). In contrast, we will compare collisional systems with and without neoclassical effects.

shape	$c_{n,T}$	w_n	w_T	$\delta_{n,T}$	κ_n	κ_T
peaked	0.5	0.15	0.25	-	0.789	3.49
flat-top	0.5	0.05	0.05	0.25	0.789	3.49

Table 6.1: Profile parameters for gradient driven simulations. For their definition see Sec. 4.2 and Eq. (4.8a), (4.9).

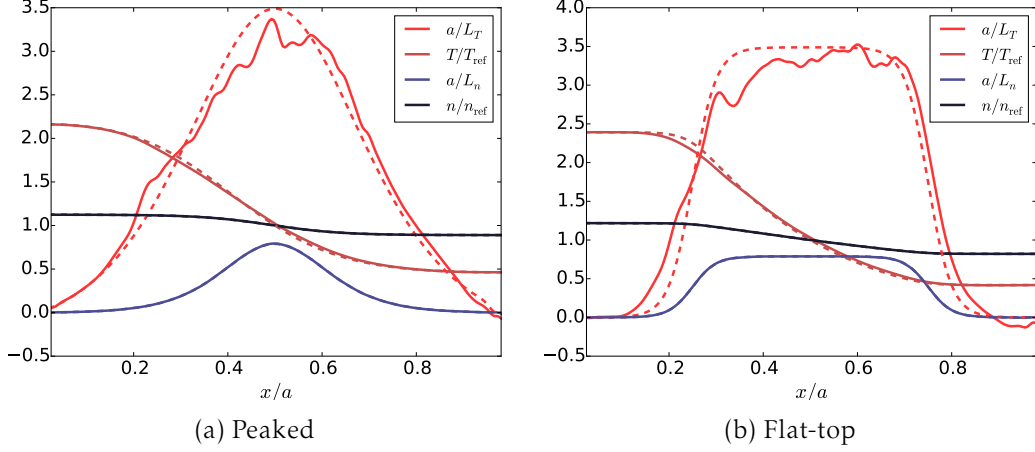


Figure 6.1: Shape of the radial profiles for T_i and n_i . Dashed: initial state, solid: time average over 500 time units at $t \sim 2000a/c_s$

For gradient-driven simulations we set up temperature and density gradient profiles according to either Eq. (4.8a) or (4.9) and keep them fixed in a time-averaged sense by using Krook type heating. We study both cases with peaked (Eq. (4.8a)) and flat-top (Eq. (4.9)) gradient profiles with the shape and position parameters given in Tab. 6.1. Their initial state and their time average over several hundred time units at around $t = 2000$ in a typical simulation are shown in Fig. 6.1. While some deviation from the initial state can be found, it is not problematic and based on a trade-off with the modification of the system caused by a stronger Krook source. The safety factor profile has the monotonically increasing form of Eq. (4.10). The typical grid is chosen as $(N_x, N_{k_y}, N_z, N_{v_{\parallel}}, N_{\mu}) = (N_x, 32, 32, 64, 32)$, where N_x is adapted when the system size parameter ρ_* is changed to ensure 1 – 1.33 grid points per ion gyroradius. The ion-ion collision frequency varies over the radial domain, but its value at $x = 0.5a$ is determined by setting the parameter $\nu_c = 3.863 \cdot 10^{-3}$. This corresponds to a collisionality of $\nu_*(x = 0.5a) = 0.29$, which is in the banana regime but not very far. The simulation time is chosen to cover at least 2 ion-ion collision times at all radial positions in order to ensure reasonably converged neoclassical fluxes.

6.1.1 System size effects

The physical parameter of primary interest is the normalized gyroradius ρ_* . Any observed interaction between ITG turbulence and the neoclassical effects should weaken and disappear when ρ_* decreases since the simulations then approach the local (flux

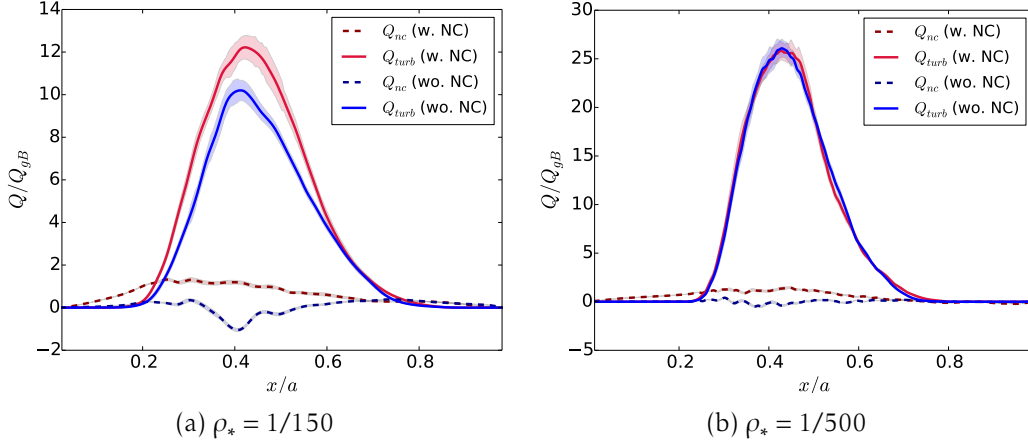
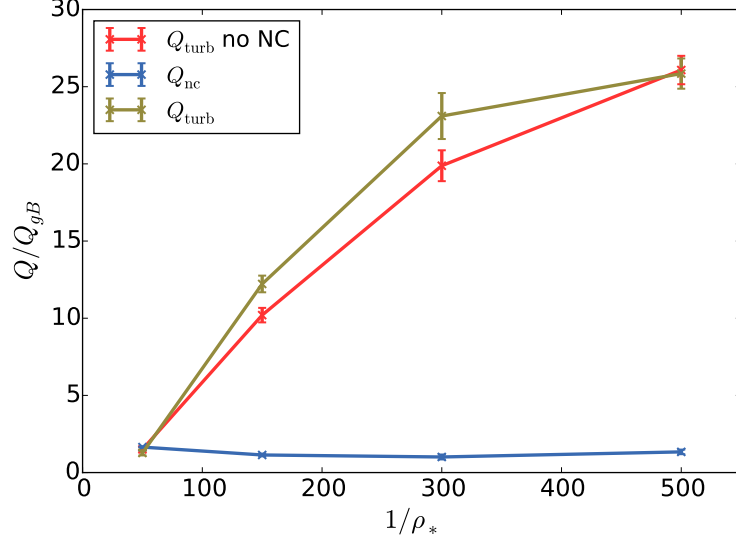


Figure 6.2: Neoclassical and turbulent radial heat flux profile (peaked gradient, averaged over last 600 time units); uncertainties according to Sec. 3.5.3

tube) limit. The ρ_* considered here is its value at the position $x/a = 0.5$. The local ion gyroradius varies with the temperature and the magnetic field strength. It should also be noted that since both profiles are quite narrow the scaling of the turbulent flows does rather depend on an effective $\rho_{*eff} = \rho_*/\Delta_T$ (where Δ_T is related to w_T or δ_T respectively) [68, 69].

Peaked gradient profile

The weakening of interaction can be observed in Fig. 6.2 where the time-averaged heat fluxes are plotted as a function of the radial position for the peaked gradient profile for two different ρ_* . The turbulent flow is increased by the presence of neoclassical effects for $\rho_* = 1/150$ but remains the same within the statistical error for $\rho_* = 1/500$. The time-averaged so-called neoclassical flux Q_{nc} agrees well with the Chang-Hinton prediction if the neoclassical source is present. If it is absent, non-zero though small transport is measured in this channel. This reflects the statement of Sec. 3.5.2 that Q_{nc} is the flux on the $k_y = 0$ mode caused by the magnetic drift whose major but not exclusive contribution are neoclassical effects. If we consider additional values for ρ_* and compare the value of the time-averaged fluxes at the radial maximum of the turbulent flow (appearing at $x/a \approx 0.4$ for all cases), we arrive at the scaling shown in Fig. 6.3. The general trend that turbulent transport decreases with growing ρ_* is a well established observation [69, 70]. Due to the narrow profile shape (see above) the convergence to the local limit occurs at relatively large ρ_* . At this point it is important to remember that the fluxes are measured in units which imply the *gyro-Bohm* scaling, i.e. diffusive behavior with the scale of the ion gyroradius and thus locality. Neoclassical heat transport outside of the potato region (see Sec. 4.2.2) fulfills this condition and hence is mostly independent of ρ_* in Fig. 6.3. The observed scaling of turbulent transport means that system size effects start to play a role at large ρ_* . Below $\rho_* = 1/300$ the scaling is quite close to *Bohm-like*, i.e. $Q/Q_{gB} \propto 1/\rho_*$. Comparing its values for a fixed system size we find a systematic increase of 20 – 30% for the system with neoclassical effects for

Figure 6.3: Time averaged radial heat flux peak dependence on ρ_* .

$\rho_* \leq 1/300$. It should be emphasized that this difference is not the neoclassical flux, which is measured separately and comes on top for an estimate of the total energy flux.

For $\rho_* = 1/50$ both transport channels reach the same magnitude because the turbulent eddies' radial extent barely fits into the region where the temperature gradient can drive them. Since this case operates at the limits of the validity of the used gyrokinetic model and boundary artifacts can spread far across the radial domain we do not analyze it beyond this qualitative observation.

With the general interaction confirmed we return to the two cases of Fig. 6.2 and investigate how the presence of the neoclassical source modifies the spatio-temporal dynamics. The time resolved turbulent ion heat flux profiles in Fig. 6.4 all show the ripple structures we have already found in the local simulations of Chapter 5. These avalanches have been observed in several studies of ITG turbulence e.g. Ref. [69, 71]. Ref. [72] finds their direction to be connected to the sign of the $\mathbf{E} \times \mathbf{B}$ shear: $\omega_{\mathbf{E} \times \mathbf{B}} > 0$ means outward movement, $\omega_{\mathbf{E} \times \mathbf{B}} < 0$ inward movement. Obviously, in Fig. 6.4(a) and (b) the presence of neoclassical effects changes the avalanche directions from a singular one to a V shape. This is consistent with the results of Sec. 4.2.1, although the field profile does not exactly follow the pressure gradient due to the collisionality-dependent factor k in Eq. (4.12) which also varies in radial direction. In consequence, we attribute the transport modification at least partly to a change in the zonal $\mathbf{E} \times \mathbf{B}$ shear pattern by the neoclassical radial electric field. In contrast to our local results, however, the additional long range electric field now causes an increase not a reduction of heat transport. The explanation lies within the nonperiodicity of the radial domain. While the phase δ_{ext} of the external potential in Eq. (5.1) had no impact on the turbulence level of the local simulations, it matters for global simulations with their radially varying profiles. Indeed, if we look at the time averaged field and corresponding $\omega_{\mathbf{E} \times \mathbf{B}}$ for $\rho_* = 1/150$ (Fig. 6.5), the presence of the neoclassical field seems to align an area with very low shear - the minimum of E_r - with the peak of the gradient at $x = 0.5a$. Hence, the strongest turbulence drive would coincide with the weakest damping. Root

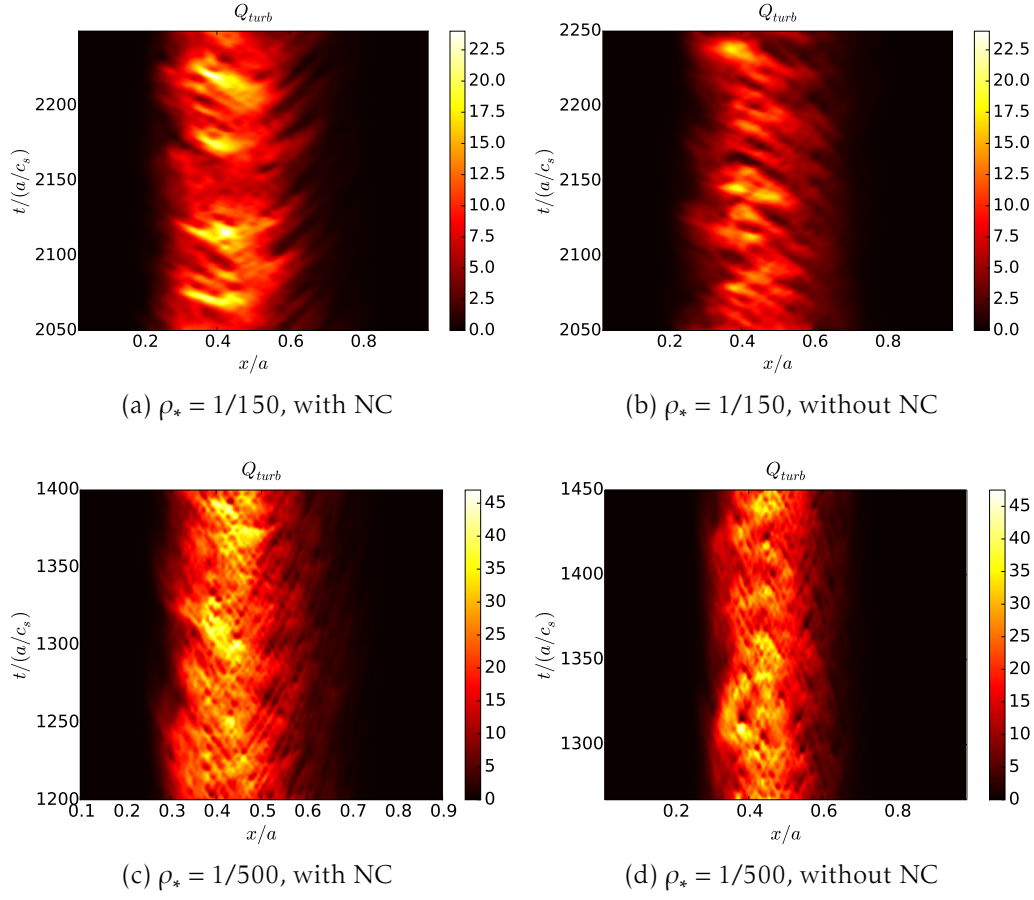
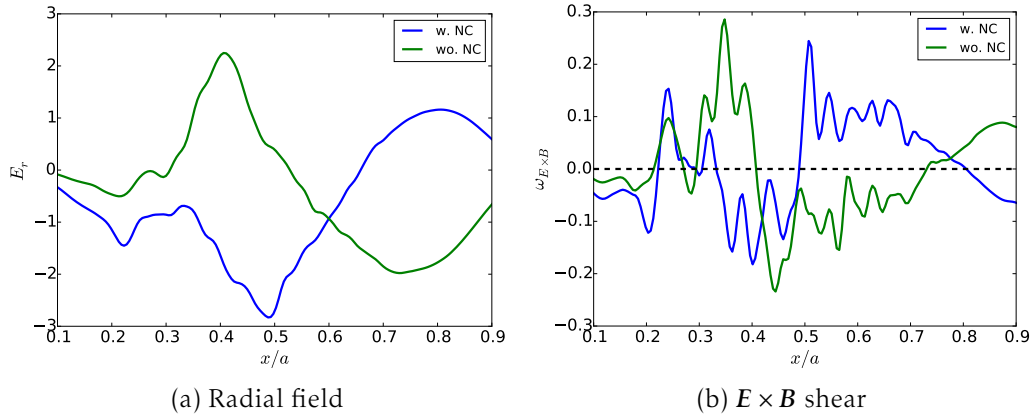


Figure 6.4: Time resolved turbulent radial heat flux profile (peaked gradient)

Figure 6.5: Time averaged radial electric field and shear, $\rho_* = 1/150$, peaked gradient

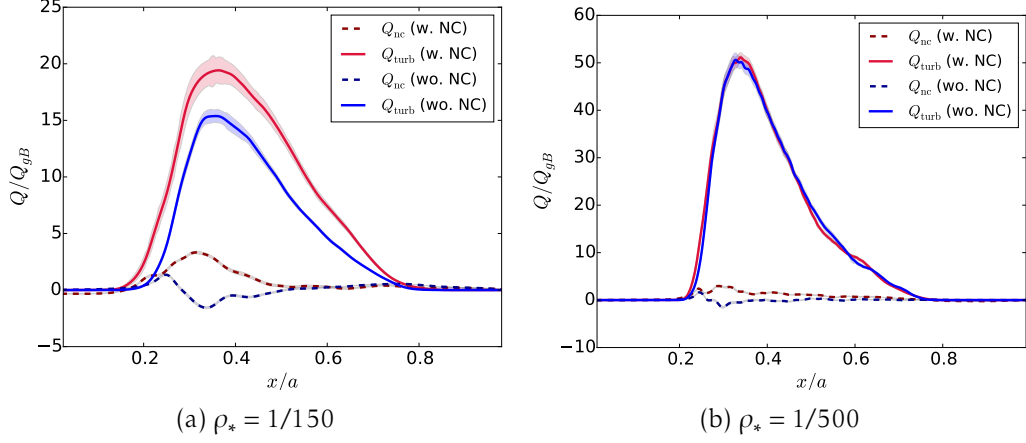


Figure 6.6: Neoclassical and turbulent radial heat flux profile (flat-top gradient, averaged over last 600 time units)

mean square radial averages of $\omega_{E \times B}$ on the other hand yield similar values for both cases. Accordingly, the flux increase by the presence of the neoclassical source is not in direct contradiction to the results of Sec. 5.2; the additional radial electric field does not generate a significant amount of absolute shear rate.

In the case of Fig. 6.4(c) and (d) the spatial scales of zonal flows ($20 - 50\rho_i$) and neoclassical field (system size, i.e. $500\rho_i$) are so far apart that the flow pattern is not generally affected: The direction of the avalanches changes multiple times independently of the long-range background field.

Flat-top gradient profile

A straightforward way to test the argument made about the alignment of temperature gradient and $E \times B$ shear profile is to study systems with the flat-top profiles of Fig. 6.1(b).

We find again a consistently increased ($\sim 30\%$) turbulent ion heat flux for $\rho_* = 1/150$ when the neoclassical source is present (Fig. 6.6(a)) and vanishing interaction between turbulence and neoclassical equilibrium for $\rho_* = 1/500$ (Fig. 6.6(b)). When we examine the $E \times B$ shear profile of the former case in Fig. 6.7(b), the simulation with neoclassical source exhibits a visibly lower level of shear in the region $x/a \sim 0.4 - 0.8$. Further inwards the shearing rate peaks in both simulations at $x/a \sim 0.3$ with approximately equal magnitude while the turbulent heat fluxes are clearly different. It can be misleading though to focus on a single radial position: Since the turbulent fluctuations have finite spatial correlations, transport is nonlocal and it is plausible that the narrower shear peak in the system with neoclassical effects is less effective in damping the heat flux. In conclusion, for a flat-top gradient the alignment argument is insufficient when only considering the temperature and $E \times B$ shear to explain the turbulent flux modification by the neoclassical source. Although the gradient is the dominant quantity for determining the turbulence drive, it is not the only one: The magnetic shear \hat{s} , for example, also plays a role, as was pointed out in Sec. 5.2 and Ref. [65, 66]. So the modification of the radial electric field by its neoclassical contribution remains a crucial

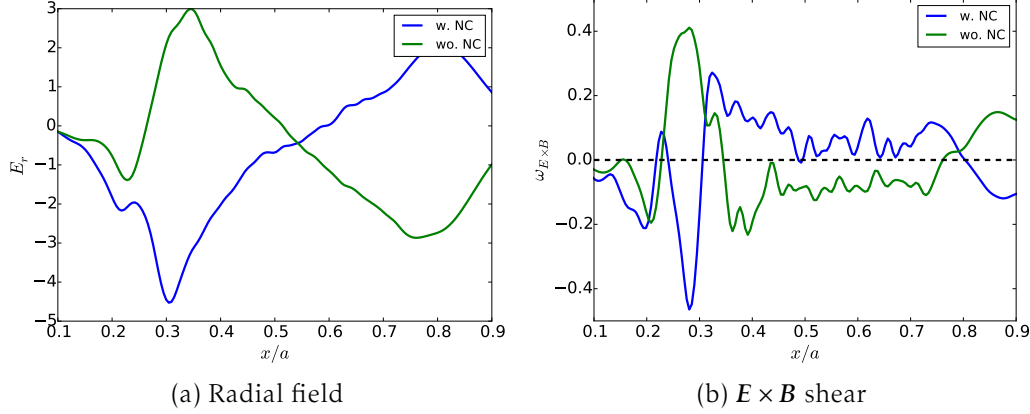


Figure 6.7: Time averaged radial electric field and shear, $\rho_* = 1/150$, flat-top gradient

effect as it still can align minimum shear regions with ones of the strongest linear growth rate.

6.1.2 Collisionality effects

The collision frequency in the results presented so far in this section is chosen artificially high in order to achieve convergence of the neoclassical fluxes with a reasonable computational effort. The neoclassical radial electric field is coupled to the parallel dynamics and establishes much faster. Hence, we investigate the influence of reducing the collision frequency which - as a side effect - brings it closer to a realistic value (as far as our model system can be considered realistic). This is achieved by setting the parameter ν_c to $1/3$ or $1/10$ of its original value, i.e. $\nu_c = 1.159 \cdot 10^{-3}$ ($\nu_*(x = 0.5a) = 0.095$) and $\nu_c = 3.863 \cdot 10^{-4}$ ($\nu_*(x = 0.5a) = 0.029$). We will refer to these cases as *medium* and *low* collisionality, respectively.

The turbulent heat fluxes measured in simulations for both collisionalities (Fig. 6.8) exhibit an interesting behavior: Without the neoclassical source term the energy flux is reduced with decreasing collision frequency as can be explained by a weaker collisional damping of zonal flows (see Sec. 5.1). If neoclassical effects are present, however, this dependency vanishes and we find a flux profile which is very similar for all three collisionalities considered so far. Hence, the level of turbulent energy transport remains independent from the collisionality over an order of magnitude. As can be seen in Fig. 6.8(c) our simulations cover a wide range of collisionalities from close to the plateau regime down to the definite banana regime. Even if the independence of the fluxes holds for $\nu_c \rightarrow 0$, it is not in contradiction to Ref. [61] and Eq. (6.1) because a different behavior for the limit $\nu_c \rightarrow 0$ and $\nu_c = 0$ is easily possible¹¹. Furthermore, a truly collisionless simulation needs to neglect the neoclassical source term, too. Otherwise, the numerically necessary velocity space hyperdiffusion operator acts as a crude collision term and any observed neoclassical effects should be considered spurious.

¹¹A prominent example for such an effect is the difference between the low viscosity limit of the Navier-Stokes equation and the Euler equation.

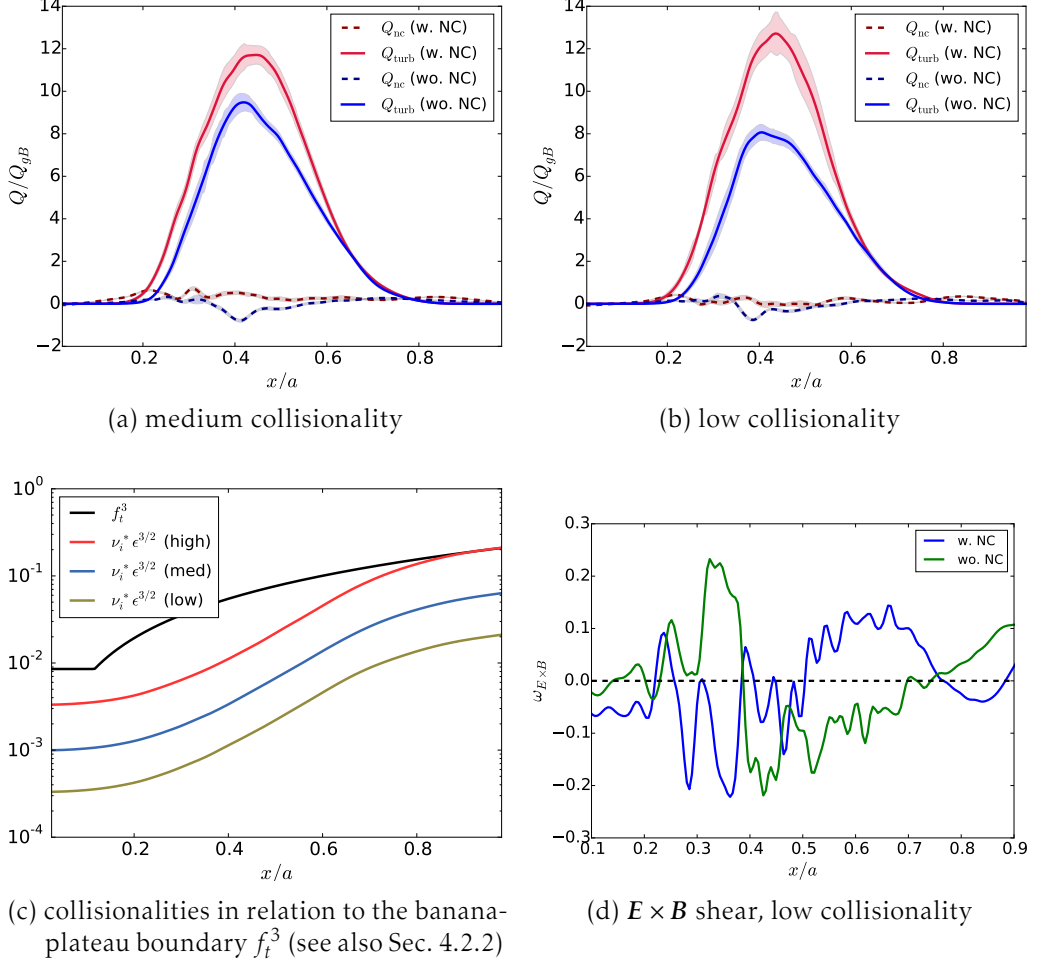


Figure 6.8: Collisionality dependence of turbulent radial heat flux profile and $E \times B$ shear (peaked gradient, averaged over last 500 time units)

When we study the $E \times B$ shear pattern for the low collisionality case in Fig. 6.8(d) we find again a region of low shear near the peak of the temperature gradient profile when the neoclassical radial electric field is present.

The neoclassical radial heat fluxes are naturally lower for smaller collisionality as was demonstrated for the local case in Fig. 4.1 in agreement with analytical predictions. Especially for Fig. 6.8(b), however, temporal convergence is not assured for the inner ($x/a \lesssim 0.5$) region. This is not problematic, though, as the radial neoclassical flux is not the effect causing the modification of the turbulence.

6.1.3 Safety factor effects

The last physical parameter we investigate in gradient-driven simulations is the safety factor profile $q(x)$. Instead of the monotonically increasing polynomial we now choose the form:

$$q(x/a) = 2.400 - 0.736x/a - 2.774(x/a)^2 + 0.950(x/a)^3 + 3.399(x/a)^4. \quad (6.2)$$

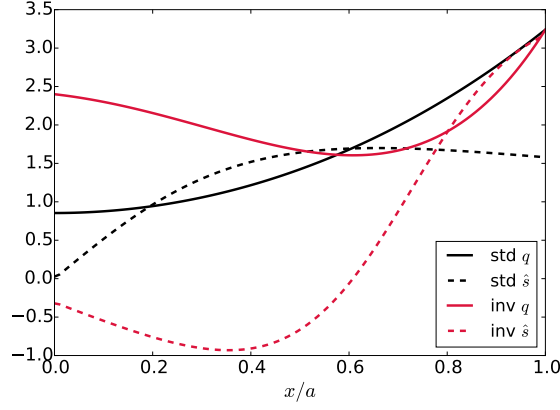


Figure 6.9: Safety factor $q(x)$ and magnetic shear $\hat{s}(x)$ profiles for the standard (Eq. (4.10)) and negative shear (Eq. (6.2)) cases

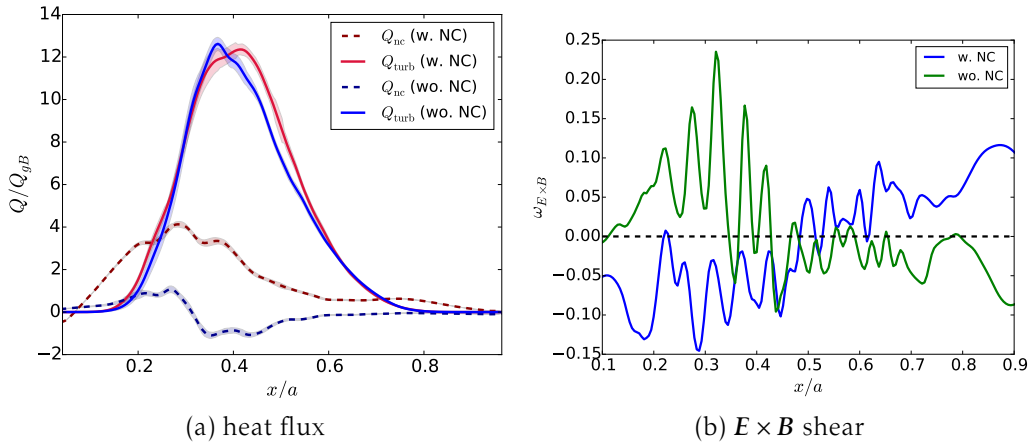


Figure 6.10: Effect of the negative \hat{s} safety factor profile on radial heat fluxes and $E \times B$ shear (peaked gradient, averaged over last 500 time units)

In Fig. 6.9 this function is compared with the one used in the global simulations so far (Eq. (4.10)). When the corresponding magnetic shear $\hat{s} = \frac{a}{q} \frac{\partial q}{\partial x}$ is considered, the particular feature of the new function is that its derivative and accordingly the magnetic shear are *negative* for $x/a = 0.0 - 0.6$ - sometimes this is called an *inverse shear*. This is the logical continuation of the last parameter study in Sec. 5.2 where we considered a local magnetic shear of 0. The inverse shear profile is used especially in experimental scenarios which have *internal transport barriers* (ITBs) [64, 73]. In an ITB the turbulent transport can be reduced to and below the neoclassical level and the temperature gradient becomes steep so that nonlocal effects are more relevant. Thus, physical parameters which correspond to such a barrier are of fundamental interest for this work. Here, we limit ourselves to the safety factor; all other parameters correspond to the peaked gradient case with high collisionality and $\rho_* = 1/150$ (Fig. 6.2(a)).

Comparing the radial turbulent heat fluxes for simulations with and without the neoclassical source term gives a peculiar result for this parameter set. As can be seen in Fig. 6.10(a) the fluxes are almost equal and around the level we found for the other

peaked-profile cases including neoclassical effects. The profile of the $E \times B$ shear is consistent with this as neoclassical and non-neoclassical simulation develop an almost equal level in the region of the temperature gradient profile maximum. While the agreement of the fluxes and shearing rates for these two simulations is most probably coincidental, we observe another example where the presence of the neoclassical radial field seems to strongly weaken the dependency of the turbulence on a plasma or confinement device parameter.

The neoclassical heat flux (when its source is present) on the other hand is significantly higher than for the monotonous q profile. This is not very surprising as neoclassical fluxes are known to scale with $q^2 \epsilon^{-3/2}$ (see Eq. (2.10) and Ref. [28]) and Eq. (6.2) provides higher values of q in the inner region where the local ϵ is small.

With an established interaction between neoclassical and turbulent effects in gradient-driven simulations for sufficiently large ρ_* we now turn to physically more comprehensive but also numerically more demanding flux-driven simulations.

6.2 Flux-driven setups

Flux-driven simulations expand the range of physical phenomena we can study by a number of effects such as self-organization. The heat source is no longer adaptive with the possibility of acting as a sink but a localized profile with fixed power input which is undeniably much closer to experimental conditions. As previously mentioned (see Sec. 3.4.2), this is the natural operation mode of full-f codes. Since this formalism automatically includes neoclassical effects, a number of results exist on the role they can play in turbulent flux-driven simulations. With the GYSELA code [74], for example, it is found that the poloidal rotation profile is dominated by the neoclassical mean flow and the $E \times B$ shearing rate attributed to it has a similar magnitude as the one caused by zonal flows [75]. Temperature gradients also tend to establish closer to their critical values than in gradient-driven simulations so that the level of neoclassical heat transport can compete with its turbulent counterpart [76]. In GT5D simulations [71, 77] closeness to criticality is observed as well in the form that a significant part of the turbulent heat flux occurs in the form of transient *avalanches*.

The heat source in our simulations is an input of fixed power and shape positioned in the radial region $x/a = 0 - 0.4$ (essentially a wider and flatter form of the shapes shown in Fig. 4.5). At the outer edge a Krook type buffer zone is used to dissipate heat smoothly. The temperature and density profiles are initialized according to the flat-top gradient profiles of Eq. (4.9) with an amplitude significantly above the critical gradient for the temperature which accelerates their following evolution. While the density profile remains static due to the adiabatic electron approximation, the temperature evolves to adapt to the heat source and its evolution makes an adaption of the background Maxwellian necessary in our formalism. The threshold we use for this is $|f_1/F_0| \geq 0.18$. This is a relatively large value but triggering the adaption too often can lead to undesired numerical artifacts and we analyze simulations in a state when the last such reset is around 1000 time units past, i.e. the system has evolved to remain significantly below the threshold at that point. We study a system of $\rho_* = 1/150$ for

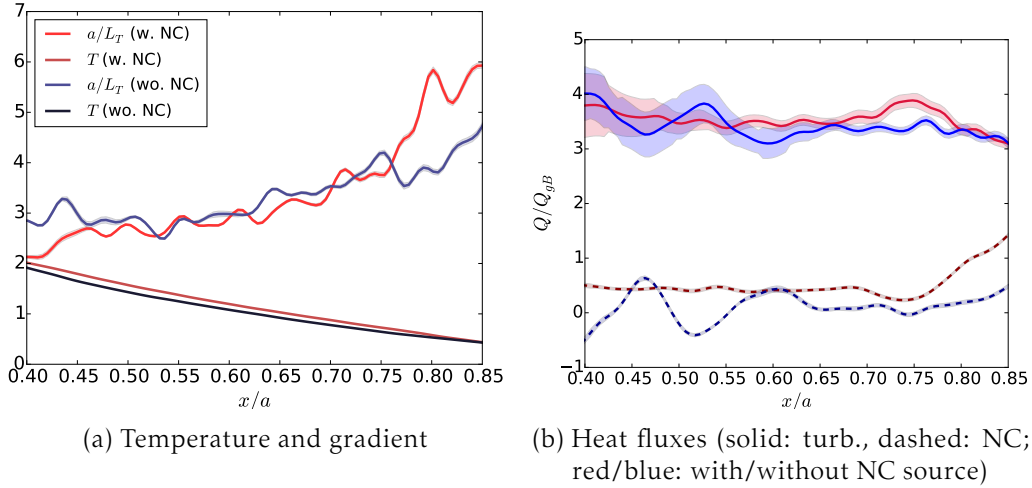


Figure 6.11: Flux-driven results in the source-free region ($\hat{S}_0 = 22500$, averaged over last 1000 time units); uncertainties according to Sec. 3.5.3

three different power inputs ($\hat{S}_0 = 11250$, 22500 and 45000) and examine the result of including or neglecting neoclassical effects.

In Fig. 6.11 we present the time averaged temperature and heat flux profiles in the radial region free of sources and sinks $x = 0.4 - 0.85$ for the stronger source and big ρ_* . As can be seen in Fig. 6.11(a) the temperature gradients for the simulation with and without neoclassical source are nearly equal with a tendency for a higher gradient without the neoclassical source. The exception is close to the outer buffer region which tends to influence the simulation up to $x \gtrsim 0.8$. The averaged turbulent heat fluxes in Fig. 6.11(b) accordingly have a similar magnitude. When the neoclassical source is present, however, some energy is also transported through the neoclassical flux channel. Hence, we would expect a slightly lower turbulent energy flux in that case. One possible explanation is that since neoclassical transport provides an evolution below the critical gradient, the non-neoclassical system is not as well converged and still consumes more heating power for temperature increase. Plotting the time evolution of T_i at three radial positions in Fig. 6.12 we find, in fact, that both cases are not fully converged yet. The systematically lower temperature in Fig. 6.12(b) compared to 6.12(a), however, confirms that the non-neoclassical system is evolving more slowly. Nonetheless, we can gain some interesting insights when observing the spatio-temporal behavior of both scenarios.

The time-resolved turbulent heat fluxes in Fig. 6.13 present a qualitatively different behavior depending on the presence of the neoclassical source: Both cases exhibit the fishbone-like patterns familiar from Fig. 5.4 and Fig. 6.4. As previously mentioned the direction of these avalanches is related to the sign of the $\mathbf{E} \times \mathbf{B}$ shear. Sign changes of the shear can lead to corrugations in the temperature profile in flux-driven simulations and the resulting pattern has been given the name *$\mathbf{E} \times \mathbf{B}$ staircase* [62, 78]. Curiously, in our simulations the most obvious structure which fulfills the criteria for a stair step is occurring close to the outer sink region at $x \sim 0.8$ in Fig. 6.13(a). The non-neoclassical simulation (Fig. 6.13(b)) has weaker steps at $x \sim 0.45$ and $x \sim 0.6$. It is clear that just as

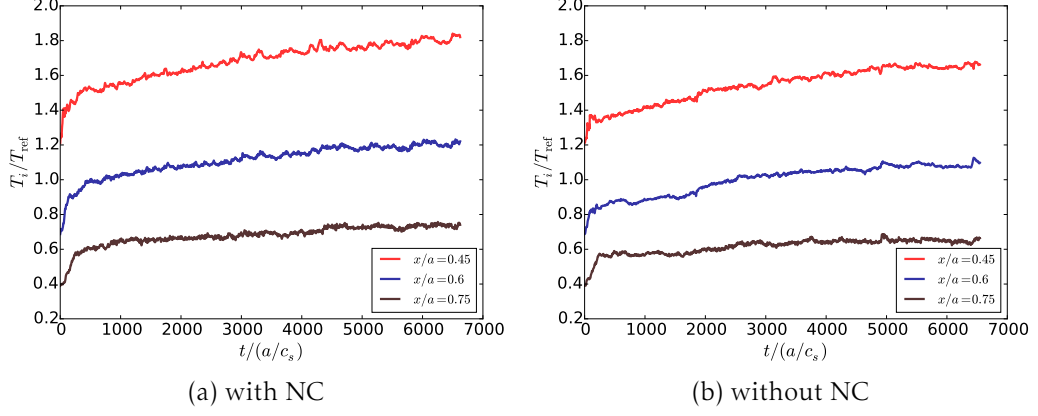


Figure 6.12: Time evolution of the temperature profile at three radial positions in a flux-driven simulation ($\hat{S}_0 = 22500$)

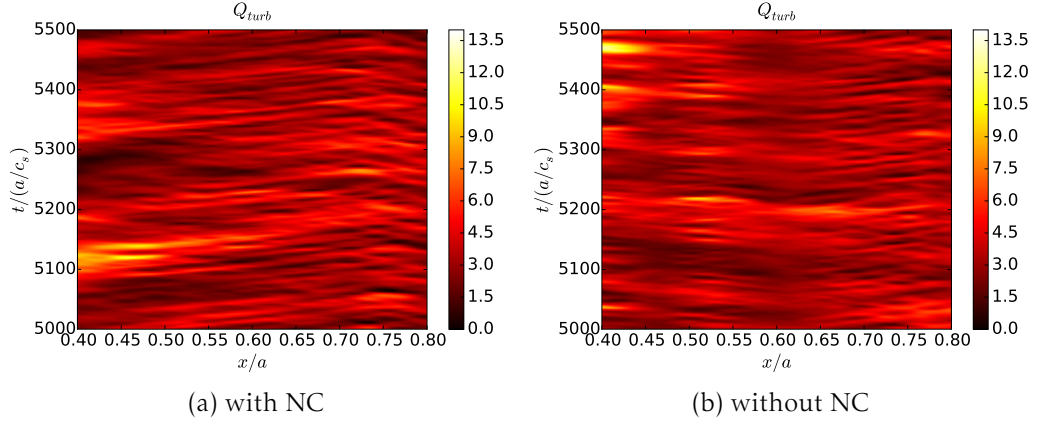


Figure 6.13: Time-resolved turbulent heat flux in the source-free region ($\hat{S}_0 = 22500$)

in gradient-driven simulations the avalanche pattern is fundamentally changed when neoclassical effects are included.

A phenomenon specific to the flux-driven systems, however, is their closeness to criticality. When the temperature gradient decreases below the critical level energy builds up and pushes it beyond criticality again. The collisional Dimits shift softening of the critical gradient smooths this behavior slightly. Hence, we can reproduce the observation of Ref. [76] and [71]. Since the neoclassical transport channel has no critical gradient, its presence will slow down this mechanism: While it is in our case not sufficiently large to transport all input heat, it provides a leak to the energy buildup. This shows up rather subtly in Fig. 6.13: Phases with low turbulent transport ($Q \lesssim 6$) are roughly 90 time units long in Fig. 6.13(a), but last only around 60 time units in Fig. 6.13(b).

Closeness to criticality is expected to be stronger when we turn our attention to a system with halved heating power ($\hat{S}_0 = 11250$) but otherwise identical parameters. As can be seen for the time-averaged quantities in Fig. 6.14(a) and (b) the system with neoclassical effects has both a slightly higher ion temperature gradient and turbulent

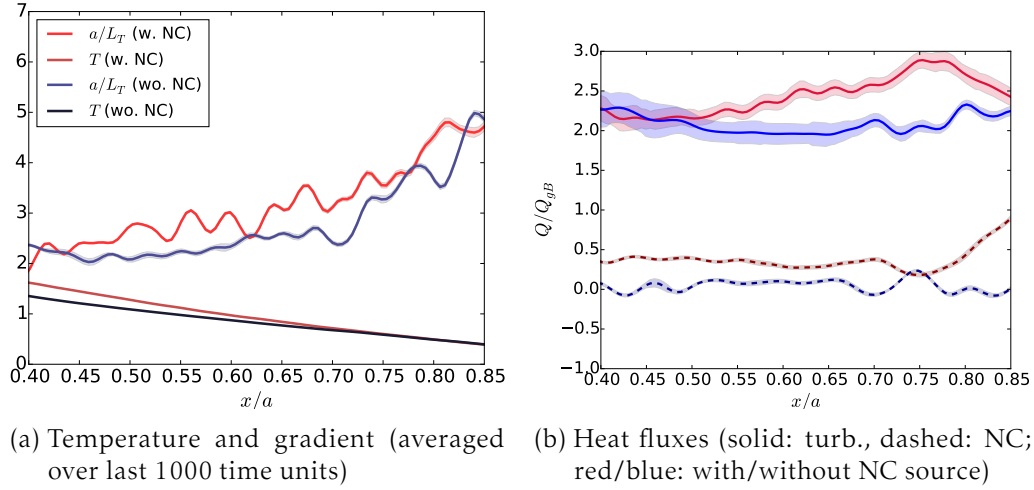


Figure 6.14: Flux-driven results in the source-free region for reduced source amplitude ($\hat{S}_0 = 11250$)

heat flux. This again points to the previously noted different convergence speed between the two cases which is consistently more severe for a weaker turbulence drive. Due to this we concentrate on comparing this system to the one with $\hat{S}_0 = 22500$. The central observation is that the turbulent transport almost halves as should be expected for half power input while the gradient is reduced only by very little. This phenomenon is known as *profile stiffness* and a well established observation in experiments [79, 80]. In the simulations of Chapter 5 we have shown it in its inverse form: When the gradient is imposed, the level of turbulent transport is extremely sensitive to it.

We can confirm the observed stiffness of the temperature gradient in a simulation with a stronger source ($\hat{S}_0 = 45000$). This also has the advantage that convergence of the profiles is reached more quickly. Indeed, in Fig. 6.15(a) and (b) we now observe nearly equal gradient with and without neoclassical source, but part of the radial heat transport occurs as neoclassical transport in the former case and the turbulent flow is accordingly smaller. For the time resolved fluxes we again find the well-established difference in avalanche direction. Furthermore, there now is a clear change to the intermittency of heat flux bursts: The system with neoclassical effects (Fig. 6.15(c)) appears calmer with phases of low turbulent transport ($Q < 5$) lasting up to $100 a/c_s$. Without the neoclassical channel on the other hand these phases end already after $30-40 a/c_s$.

Finally, collecting the information from the three heating power scenarios a comparison of the heat flux and gradients at the representative position $x/a = 0.6$ in Fig. 6.16 demonstrates the described stiffness in a very clear way: The temperature gradient remains nearly constant while the heat flux at least doubles from the weakest to the strongest power input.

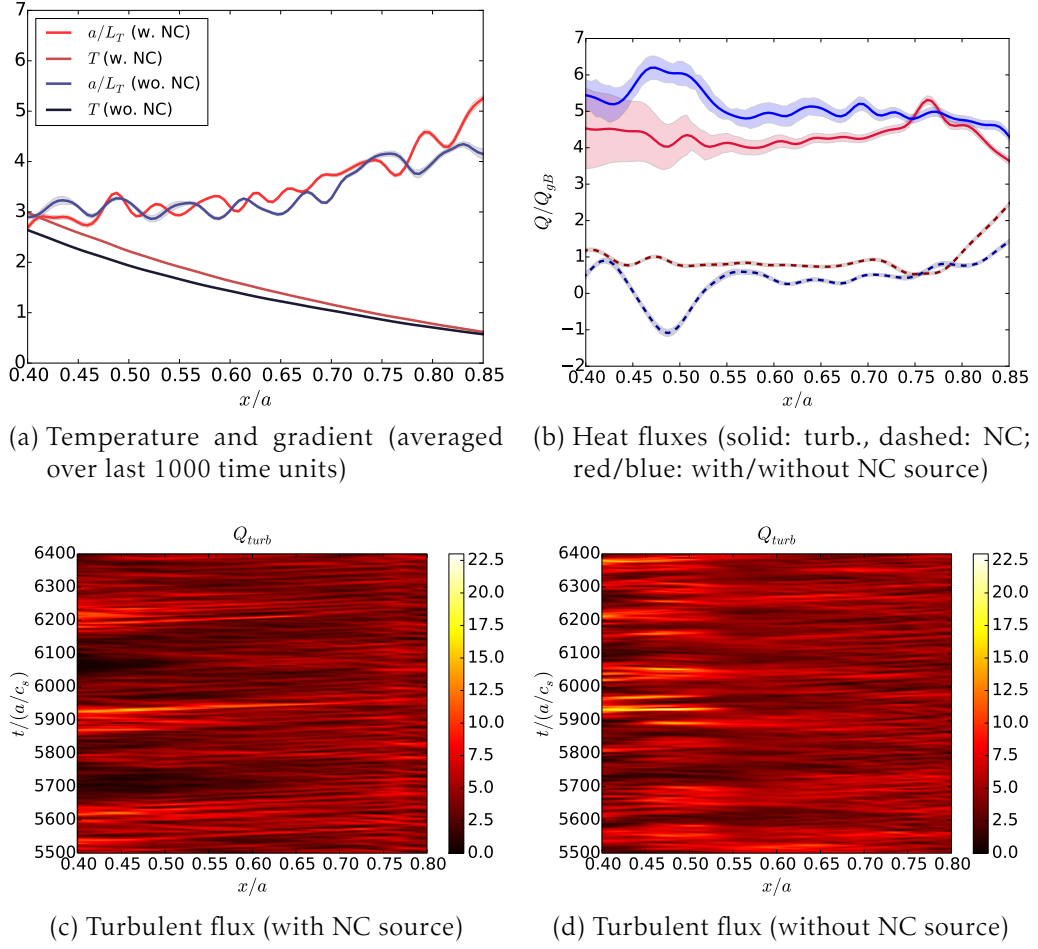


Figure 6.15: Flux-driven results in the source-free region for increased source amplitude ($\hat{S}_0 = 45000$)

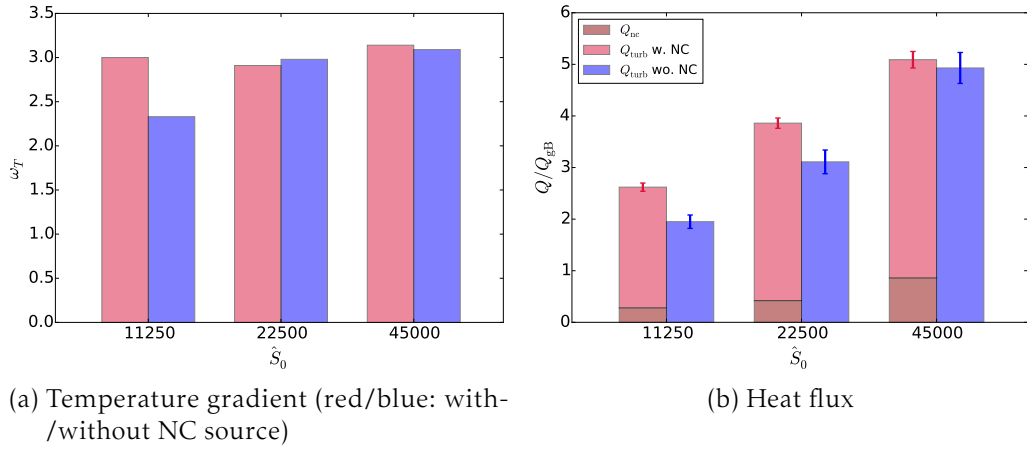


Figure 6.16: Comparison of the time averaged temperature gradients and heat fluxes at $x/a = 0.6$ for different power inputs

6.3 Summary

In this chapter radially global gyrokinetic simulations were used to explore the interaction between neoclassical and turbulent effects. In scenarios with fixed gradient (gradient-driven) it was demonstrated that this interaction only occurs when nonlocal effects play a role and vanishes for $\rho_* \leq 1/500$. This indicates that the analytical separation between the two effects in the local limit can be reproduced. It even implies that treating neoclassical and turbulent transport separately is valid before flux-tube simulations are justified by the turbulent scaling with ρ_* . This is often assumed to be the case for modeling of experiments. For larger ρ_* (or presumably ρ_{*eff}), however, including neoclassical effects in a turbulent simulation becomes strongly advisable. It was shown that the presence of neoclassical effects tends to reduce the dependence of turbulent transport on plasma parameters such as collisionality and safety factor profile. A possible explanation for this is that the neoclassical radial electric field determines the spatial positioning of the zonal flow pattern (similar to the results of Chapter 5) aligning zones with small $\mathbf{E} \times \mathbf{B}$ shear with ones of high turbulence drive. It was also possible to reproduce the phenomenon of radial heat flux avalanches whose direction follows the sign of the $\mathbf{E} \times \mathbf{B}$ shearing rate found in simulation results in the literature.

Finally, systems with fixed power input (flux-driven) were investigated where the temperature (gradient) profile evolves self-consistently according to a localized heat source. These simulations are considerably more complex computationally intensive but allow more insight into self-organization phenomena. It was possible to reproduce the basic qualitative behavior of results from full-f simulations, such as the occurrence of intermittent bursts as a transport mechanism for energy because the system is closer to criticality. The frequency and amplitude of these bursts is modified when the additional neoclassical transport channel is present. By comparing different energy input powers the experimentally and theoretically established phenomenon of profile stiffness was confirmed. However, further and longer simulations need to be performed to reach a truly self-consistent flux-power balance for our low input power cases. With the self-consistent steady-state profiles gradient-driven simulations can be performed in the future in order to better understand the difference between the two.

Chapter 7

Conclusions

In magnetically confined plasmas for nuclear fusion research two main channels for the cross-field transport of particles, heat and momentum exist: Neoclassical transport is driven by collisions and the curvature of the magnetic field. Turbulent transport arises from microinstabilities driven by the steep temperature and density gradients in the radial direction. The main goal of this work was to explore and confirm synergies between neoclassical effects and turbulence in tokamaks. This phenomenon is of importance for the modeling of small devices and for improved confinement regimes such as internal transport barriers and the edge barriers found in H-mode operation. Thus it is connected to one of the key physics tasks for the efficient operation of future power plants. While the specific situation of such barriers was not investigated, the foundation for such research was successfully established.

In the following we will review the main findings of this thesis and give prospects for future research based on them.

7.1 Summary

Gyrokinetic theory and the GENE code

Since the gyrokinetic Vlasov-Poisson equation system constitutes the theoretical model underlying this work, it was presented in the form as it is numerically solved by the Eulerian δf code GENE. Special focus was given to the elements crucial for the correct modeling of neoclassical transport such as the collision operator and features not used in the simulations of this work were neglected. It was also discussed how the gyrokinetic equation includes the drift-kinetic limit, which forms the basis of neoclassical theory.

After introducing the basic numerical approach of the GENE code, the two methods to handle the evolution of the kinetic profiles in global simulations were discussed. The first one employs an adaptive Krook-type heat source which fixes the time-average of the gradient profiles to their initial state, giving rise to so-called gradient-driven simulations. The second method utilizes a localized heat source and allows the kinetic profiles to evolve consistently to the fixed power input. For these flux-driven simulations, however, the validity of the δf splitting in the underlying equations needs to be preserved. In the course of this work, the existing basic mechanism for adapting the background distribution function F_0 to the evolved temperature and density profiles

was tested and refined by implementing, for example, filtering procedures to exclude gyroradius-scale fluctuations from F_0 .

Furthermore, radial turbulent and neoclassical particle, energy and momentum fluxes were calculated from the distribution function. In the case of neoclassical fluxes in global simulations, care was taken to find a form consistent with the definitions of standard (local) neoclassical theory. Since the fluxes correspond to physically measurable quantities, means of estimating their uncertainty were discussed, where their fluctuating nature and temporal autocorrelation are accounted for. The statistically most sound method was found to be the standard error of the mean based on batch means. Each batch consists of the flux measurements within a time window of several (typically five) estimated correlation times. Consequently, all uncertainties given in this work are based on this method.

Neoclassical equilibria

Before including turbulent fluctuations, purely neoclassical systems were investigated. As a first step, agreement between neoclassical heat fluxes in local simulations with analytic predictions for the different collisionality regimes was confirmed over a wide collisionality range.

It was demonstrated that it is possible to self-consistently calculate the neoclassical radial electric field in global simulations. Moreover it conforms to the radial force balance equation. In this context, it was found that it is important to use a von Neumann boundary condition on the inner edge of the radial simulation domain.

Finally, the tokamak region near the magnetic axis, where the standard assumption of (radially) thin drift orbits becomes invalid, was studied. A breakdown of standard local neoclassical theory and the importance of finite-orbit width effects in the potato-orbit region could be confirmed. Since a comparison with existing theoretical predictions in this region did not provide satisfying agreement in gradient driven simulations, flux-driven simulations over neoclassical confinement times were performed. There, indications were found that the potato radius r_p is a scale relevant for the temperature gradient profiles, which establish consistently to the localized fixed power input.

Interaction between neoclassics and turbulence

The study of the synergies between neoclassical and turbulent transport was carried out in several steps, with increasing complexity and computational cost per simulation, when moving from local (flux-tube) to radially global gradient- and finally flux-driven scenarios.

First, as a simple model, a constant sinusoidal long wavelength electrostatic potential was imposed on local simulations of ion temperature gradient-driven (ITG) turbulence. This external field can be considered an approximation of the shape and amplitude of the neoclassical radial electric field found in global simulations. By numerous nonlinear simulations, a clear connection between the turbulent heat flow and the external $E \times B$ shearing rate was found. An external shear of small amplitude (in comparison to the intrinsic shearing rate emerging from the turbulent state) can

significantly decrease heat transport. More importantly, the dynamics of the intrinsic shear flows (so-called zonal flows) adapt to the externally imposed radial structure, even for very weak external fields. Only when the wavelength of the external potential was chosen short enough, turbulent structures could be observed moving across the shear pattern. Consequently, they were damped less than by shear of comparable root mean square value but longer wavelength.

Secondly, the effect of neoclassical contributions (especially the self-consistently calculated electric field) on global gradient-driven systems was studied. As previously mentioned, an adaptive heating preserves the time-averaged gradient profiles in these cases. For scenarios with a normalized ion thermal gyroradius $\rho_* = \rho_i/a \geq 1/300$, a significant increase of the turbulent transport was observed – in addition to the neoclassical contribution to total cross-field transport. At $\rho_* = 1/500$ the separation of neoclassics and turbulence in the local limit was reestablished. Overall, the commonly found deviation from the gyro-Bohm scaling at high ρ_* for the turbulent fluxes was reproduced, while neoclassical transport was found to scale gyro-Bohm-like as expected. In addition, the presence of neoclassical effects strongly reduced the dependence of the turbulent transport on physical parameters such as collisionality and safety factor profile in our simulations. A possible explanation found was that the neoclassical field aligns zones of low $\mathbf{E} \times \mathbf{B}$ shear with regions of strong turbulence drive, e.g. the maximum of the temperature gradient profile.

Finally, similar investigations were performed in flux-driven systems with a localized heat source. Due to closeness to criticality, turbulent transport tended to occur in intermittent bursts. Amplitude and frequency of the bursts were reduced by the presence of the neoclassical transport channel. The behavior of scenarios with differing power input was compared and the widely known phenomenon of profile stiffness was observed, i.e. the value of the temperature gradient was found to be relatively independent of the power input.

The central conclusion drawn from this work is that it is possible to include neoclassical effects in gyrokinetic simulations and that there are a number of physically relevant scenarios where they modify the turbulent behavior in a significant way and should not be neglected. As long as the turbulent scaling justifies applying the flux-tube limit, it is also possible to treat neoclassical effects separately. For gradient-driven simulations with $\rho_* \geq 1/300$, however, neglecting the neoclassical contribution can lead to spurious heat flux measurements. This is even more the case for flux-driven scenarios.

7.2 Outlook

Since the presented work provides a basis of numerical evidence for neoclassical-turbulence interaction, it presents also a plethora of ways to expand on the fundamental observations. In the following, a number of concepts that go beyond points mentioned already in the respective chapters such as more quantitative investigations on the role of potato orbits and reaching full steady-state in turbulent flux-driven simulations are collected.

A very obvious step is to consider electrons no longer as adiabatic but as a fully gyrokinetic species. This allows to study other types of turbulence such as trapped electron modes, which exhibit a weaker zonal flow pattern and thus could react differently to the neoclassical field. Due to the higher grid resolution and time stepping requirements, however, this will be a computationally extremely challenging task – the global computations in this work are quite expensive already. A less computationally demanding future prospect involves using a shaped magnetic field geometry as it is used in experimental devices instead of circular concentric flux surfaces. This also gives the opportunity for investigations on the role of specific shaping parameters for neoclassical effects. Recently implemented extensions of GENE to include effects of plasma rotation can also be used to study the impact of rotation on neoclassical transport and whether it modifies the observed interactions with turbulence. The connection between the radial electric field and rotation by the radial force balance supports this idea. Neoclassical transport also plays an important role for the dynamic of impurities, e.g. tungsten ions, in the plasma. Including them in simulations opens a wide field for new physical insight.

The more general future goal for this work is, however, to gain a better understanding and ultimately a numerical model of transport barriers both in the core and the edge. While the relevance of internal transport barriers for a future fusion reactor can be argued, a successful model of them will be an important step towards understanding the edge barrier of the H-mode whose fundamental importance is widely accepted.

Appendix A

Definitions of collision frequencies

When performing benchmarks for neoclassical transport, one of the most important parameters is obviously the collision frequency, especially the self-collision frequency of the ions. Unfortunately, this quantity is not uniquely defined: Depending on the source it includes differing constant multipliers, SI or Gaussian units and the temperature defined as either $T = 1/2 m v_{th}^2$ or $T = m v_{th}^2$. Here, a number of conversions between them shall be provided for future reference.

The quantity ν_c from Eq. (3.3) serves as a good starting point for us as it can be set as an input parameter in GENE :

$$\nu_c = \frac{\pi e^4 n_{ref} L_{ref} \ln \Lambda}{2^{3/2} T_{ref}^2}. \quad (A.1)$$

Notably, it uses Gaussian units. On the other hand, Ref. [9] introduces ion-ion collision times of the form (using SI):

$$\frac{1}{\tau_{ii}} = \frac{\sqrt{2}}{12 \pi^{3/2} \epsilon_0^2} \frac{n_i Z^4}{m_i^{1/2} T_i^{3/2}}, \quad (A.2)$$

$$\frac{1}{\tau_i} = \frac{1}{\sqrt{2}} \frac{1}{\tau_{ii}}. \quad (A.3)$$

In terms of ν_c and other normalized quantities (see Sec. 3.3) and converting between SI and Gaussian units this can be written as:

$$\frac{1}{\tau_{ii}} = \frac{8\sqrt{2}}{3\sqrt{\pi}} \frac{\hat{n}_i Z^4}{\hat{m}_i^{1/2} \hat{T}_i^{3/2}} \nu_c \frac{c_{ref}}{L_{ref}}. \quad (A.4)$$

The definition for the ion-ion collision time found in Ref. [43] is:

$$\frac{1}{\tau_{i,V}} = \frac{1}{6\sqrt{\pi}} \frac{n_i Z^4 e^4 \ln \Lambda}{2\pi \epsilon_0^2 m_i^2 v_{th,i}^3}, \quad (A.5)$$

where, opposed to the previous expressions, $v_{th} = \sqrt{T/m}$ holds. If this is accounted for, we find that this expression agrees with $1/\tau_i$ in Eq. (A.3).

The physically most interesting quantity, on the other hand, is the collisionality ν_* , which in terms of Ref. [9] is defined as:

$$\nu_{*i} = \frac{qR_0}{\epsilon^{3/2} v_{th_i}}. \quad (\text{A.6})$$

Using Eq. (A.4) it can be expressed in GENE normalized quantities:

$$\nu_{*i} = \frac{8}{3\sqrt{\pi}} \frac{q\hat{R}_0}{\epsilon^{3/2}} \frac{\hat{n}_i Z^4}{\hat{T}_i^2} \nu_c. \quad (\text{A.7})$$

The advantage of this quantity is that it goes back to the oldest works on neoclassical theory [28], is used in the Chang-Hinton prediction [49] and is equivalently defined in the numerical works of Ref. [43] as well as Ref. [81]. Together with its physical meaning of defining the different regimes of neoclassical transport (see Sec. 2.2.2) this makes it the ideal quantity for comparing numerical results.

It should be noted here, though, that the Coulomb logarithm $\ln \Lambda$ still provides a source of discrepancies when different approximations for calculating it are used.

Bibliography

1. Bethe, H. A. & Critchfield, C. L. On the Formation of Deuterons by Proton Combination. *Physical Review* **54**, 862–862 (10 Nov. 1938).
2. Hurricane, O. A. *et al.* Fuel gain exceeding unity in an inertially confined fusion implosion. *Nature* **506**, 343–348 (Feb. 2014).
3. Gashev, M. A. *et al.* The basic technical characteristics of the experimental thermonuclear device tokamak-3. *Journal of Nuclear Energy. Part C, Plasma Physics, Accelerators, Thermonuclear Research* **7**, 491 (1965).
4. Spitzer Jr, L. *A proposed stellarator* tech. rep. (Princeton Univ., NJ Forrestal Research Center, 1951).
5. Viezzer, E. *et al.* Evidence for the neoclassical nature of the radial electric field in the edge transport barrier of ASDEX Upgrade. *Nuclear Fusion* **54**, 012003 (2014).
6. Highcock, E. G. *et al.* Transport Bifurcation in a Rotating Tokamak Plasma. *Phys. Rev. Lett.* **105**, 215003 (21 Nov. 2010).
7. Shafranov, V. D. Plasma Equilibrium in a Magnetic Field. *Reviews of Plasma Physics* **2**, 103 (1966).
8. Braginskii, S. I. Transport Processes in a Plasma. *Reviews of Plasma Physics* **1**, 205 (1965).
9. Helander, P. & Sigmar, D. *Collisional transport in magnetized plasmas* (Cambridge University Press, 2002).
10. Alfvén, H. On the motion of a charged particle in a magnetic field. *Arkiv för matematik, astronomi o. fysik* **27A**, 1 (1940).
11. Galeev, A. A. & Sagdeev, R. Z. Transport Phenomena in a Collisionless Plasma in a Toroidal Magnetic System. *Soviet Journal of Experimental and Theoretical Physics* **26**, 233 (Jan. 1968).
12. Peeters, A. G. The bootstrap current and its consequences. *Plasma Physics and Controlled Fusion* **42**, B231 (2000).
13. Kikuchi, M. & Azumi, M. Experimental evidence for the bootstrap current in a tokamak. *Plasma Physics and Controlled Fusion* **37**, 1215 (1995).
14. ITER Physics Base Editors, ITER Physics Expert Group Chairs and Co-Chairs & ITER Joint Central Team and Physics Integration Unit. Chapter 1: Overview and summary. *Nuclear Fusion* **39**, 2137 (1999).

15. Taylor, T. S. Physics of advanced tokamaks. *Plasma Physics and Controlled Fusion* **39**, B47 (1997).
16. Carrera, R., Hazeltine, R. D. & Kotschenreuther, M. Island bootstrap current modification of the nonlinear dynamics of the tearing mode. *Physics of Fluids (1958-1988)* **29**, 899–902 (1986).
17. Mangeney, A., Califano, F., Cavazzoni, C. & Travnicek, P. A Numerical Scheme for the Integration of the Vlasov-Maxwell System of Equations. *Journal of Computational Physics* **179**, 495–538 (2002).
18. Brizard, A. J. & Hahm, T. S. Foundations of nonlinear gyrokinetic theory. *Rev. Mod. Phys.* **79**, 421–468 (2 Apr. 2007).
19. Görler, T. *Multiscale effects in Plasma Microturbulence* PhD thesis (Universität Ulm, 2009).
20. Dannert, T. *Gyrokinetische Simulation von Plasmaturbulenz mit gefangenen Teilchen und elektromagnetischen Effekten* PhD thesis (Technische Universität München, 2005).
21. Huba, J. D. *NRL plasma formulary* tech. rep. (DTIC Document, 2013).
22. Landau, L. Die kinetische Gleichung für den Fall Coulombscher Wechselwirkung. *Phys. Z. Sowjet* **10**, 154–164 (1936).
23. Rosenbluth, M. N., MacDonald, W. M. & Judd, D. L. Fokker-Planck Equation for an Inverse-Square Force. *Phys. Rev.* **107**, 1–6 (1 July 1957).
24. Doerk, H. *Gyrokinetic Simulation of Microtearing Turbulence* PhD thesis (Universität Ulm, 2012).
25. D’haeseleer, W., Hitchon, W., Callen, J. & Shohet, J. *Flux Coordinates and Magnetic Field Structure* (Springer-Verlag, 1991).
26. Told, D. *Gyrokinetic Microturbulence in Transport Barriers* PhD thesis (Universität Ulm, 2012).
27. Rutherford, P. Collisional Diffusion In An Axisymmetric Torus. *Physics of Fluids* **13**, 482–& (1970).
28. Hinton, F. L. & Hazeltine, R. D. Theory of plasma transport in toroidal confinement systems. *Rev. Mod. Phys.* **48**, 239–308 (2 Apr. 1976).
29. Candy, J. & Belli, E. A. Neoclassical Transport Including Collisional Nonlinearity. *Physical Review Letters* **106**, 235003 (June 2011).
30. Belli, E. A. & Candy, J. An Eulerian method for the solution of the multi-species drift-kinetic equation. *Plasma Physics and Controlled Fusion* **51**, 075018 (2009).
31. Jenko, F., Dorland, W., Kotschenreuther, M. & Rogers, B. N. Electron temperature gradient driven turbulence. *Physics of Plasmas* **7**, 1904–1910 (2000).
32. Pueschel, M. J. *Electromagnetic effects in gyrokinetic simulations of Plasma Turbulence* PhD thesis (Westfälische Wilhelms-Universität Münster, 2009).
33. Görler, T. *et al.* The global version of the gyrokinetic turbulence code GENE. *Journal of Computational Physics* **230**, 7053–7071 (2011).

34. Arakawa, A. Computational design for long-term numerical integration of the equations of fluid motion: Two-dimensional incompressible flow. Part I. *Journal of Computational Physics* **1**, 119–143 (1966).
35. Doerk, H. & Jenko, F. Towards optimal explicit time-stepping schemes for the gyrokinetic equations. *Computer Physics Communications* **185**, 1938–1946 (2014).
36. Lederer, H., Hatzky, R., Tisma, R., Bottino, A. & Jenko, F. *Hyperscaling of Plasma Turbulence Simulations in DEISA in Proceedings of the 5th IEEE Workshop on Challenges of Large Applications in Distributed Environments* (ACM, Monterey, California, USA, 2007), 19–26.
37. Lapillonne, X. *et al.* Clarifications to the limitations of the s-alpha equilibrium model for gyrokinetic computations of turbulence. *Physics of Plasmas* **16**, 032308 (2009).
38. Merz, F. *Gyrokinetic Simulation of Multimode Plasma Turbulence* PhD thesis (Westfälische Wilhelms-Universität Münster, 2008).
39. Jarema, D. *Computer Physics Communications*. to be submitted (2015).
40. McMillan, B. F. *et al.* Long global gyrokinetic simulations: Source terms and particle noise control. *Physics of Plasmas* **15** (2008).
41. Lapillonne, X. *Local and Global Eulerian Gyrokinetic Simulations of Microturbulence in Realistic Geometry with Applications to the TCV Tokamak* PhD thesis (EPFL Lausanne, 2010).
42. Helander, P. Comments on 'Neoclassical heat flux due to poloidal electric field in arbitrary collisionality regime'. *Plasma Physics and Controlled Fusion* **37**, 57 (1995).
43. Vernay, T. *et al.* Neoclassical equilibria as starting point for global gyrokinetic microturbulence simulations. *Physics of Plasmas* **17**, 122301 (2010).
44. Cochran, W. G. *Sampling Techniques* 3rd (John Wiley & Sons, 1977).
45. Law, A. M. & Kelton, W. D. *Simulation Modeling and Analysis* 2nd ed. (McGraw-Hill, 1991).
46. Carreras, B. A. *et al.* Fluctuation-induced flux at the plasma edge in toroidal devices. *Physics of Plasmas (1994-present)* **3**, 2664–2672 (1996).
47. Balescu, R. *Transport Processes in Plasmas. Vol. 2: Neoclassical Transporttheory* (North-Holland, 1988).
48. Taguchi, M. Ion thermal conductivity and ion distribution function in the banana regime. *Plasma Physics and Controlled Fusion* **30**, 1897 (1988).
49. Chang, C. S. & Hinton, F. L. Effect of finite aspect ratio on the neoclassical ion thermal conductivity in the banana regime. *Physics of Fluids* **25**, 1493–1494 (1982).
50. Dimits, A. M. *et al.* Comparisons and physics basis of tokamak transport models and turbulence simulations. *Physics of Plasmas* **7**, 969–983 (2000).
51. Hirshman, S. & Sigmar, D. Neoclassical transport of impurities in tokamak plasmas. *Nuclear Fusion* **21**, 1079 (1981).

52. Helander, P. On neoclassical transport near the magnetic axis. *Physics of Plasmas* **7**, 2878–2883 (2000).
53. Lin, Z., Tang, W. M. & Lee, W. W. Neoclassical Transport in Enhanced Confinement Toroidal Plasmas. *Phys. Rev. Lett.* **78**, 456–459 (3 Jan. 1997).
54. Bergmann, A., Peeters, A. G. & Pinches, S. D. Guiding center particle simulation of wide-orbit neoclassical transport. *Physics of Plasmas* **8**, 5192–5198 (2001).
55. Shaing, K. C., Hazeltine, R. D. & Zarnstorff, M. C. Ion transport process around magnetic axis in tokamaks. *Physics of Plasmas (1994-present)* **4**, 771–777 (1997).
56. Shaing, K. C., Houlberg, W. A. & Strand, P. I. Local potato-plateau transport fluxes and a unified plateau theory. *Physics of Plasmas (1994-present)* **9**, 1654–1658 (2002).
57. Cowley, S. C., Kulsrud, R. M. & Sudan, R. Considerations of ion-temperature-gradient-driven turbulence. *Physics of Fluids B: Plasma Physics (1989-1993)* **3**, 2767–2782 (1991).
58. Diamond, P. H., Itoh, S.-I., Itoh, K. & Hahm, T. S. Zonal flows in plasma - a review. *Plasma Physics and Controlled Fusion* **47**, R35 (2005).
59. Lin, Z., Hahm, T. S., Lee, W. W., Tang, W. M. & Diamond, P. H. Effects of Collisional Zonal Flow Damping on Turbulent Transport. *Phys. Rev. Lett.* **83**, 3645–3648 (18 Nov. 1999).
60. Hahm, T. S. *et al.* Shearing rate of time-dependent $E \times B$ flow. *Physics of Plasmas* **6**, 922–926 (1999).
61. Vernay, T. *et al.* Synergy between ion temperature gradient turbulence and neoclassical processes in global gyrokinetic particle-in-cell simulations. *Physics of Plasmas* **19**, 042301 (2012).
62. Dif-Pradalier, G. *et al.* On the validity of the local diffusive paradigm in turbulent plasma transport. *Phys. Rev. E* **82**, 025401 (2 Aug. 2010).
63. Dirickx, M. & Weyssow, B. Effects of orbit squeezing on ion transport, poloidal mass flow and bootstrap current in the limit of very low collisionality. *Plasma Physics and Controlled Fusion* **42**, 711 (2000).
64. Wolf, R. C. Internal transport barriers in tokamak plasmas. *Plasma Physics and Controlled Fusion* **45** (Jan. 2003).
65. Dong, J. Q., Horton, W. & Kim, J. Y. Toroidal kinetic η_i -mode study in high-temperature plasmas. *Physics of Fluids B: Plasma Physics (1989-1993)* **4**, 1867–1876 (1992).
66. Jenko, F., Dorland, W. & Hammett, G. W. Critical gradient formula for toroidal electron temperature gradient modes. *Physics of Plasmas (1994-present)* **8**, 4096–4104 (2001).
67. Joliet, S. *et al.* A global collisionless {PIC} code in magnetic coordinates. *Computer Physics Communications* **177**, 409–425 (2007).
68. McMillan, B. F. *et al.* System Size Effects on Gyrokinetic Turbulence. *Phys. Rev. Lett.* **105**, 155001 (15 Oct. 2010).

69. Görler, T. *et al.* Flux- and gradient-driven global gyrokinetic simulation of tokamak turbulence. *Physics of Plasmas* **18**, 056103 (2011).
70. Villard, L. *et al.* Gyrokinetic simulations of turbulent transport: size scaling and chaotic behaviour. *Plasma Physics and Controlled Fusion* **52**, 124038 (2010).
71. Idomura, Y., Urano, H., Aiba, N. & Tokuda, S. Study of ion turbulent transport and profile formations using global gyrokinetic full-f Vlasov simulation. *Nuclear Fusion* **49**, 065029 (2009).
72. McMillan, B. F. *et al.* Interaction of large scale flow structures with gyrokinetic turbulence. *Physics of Plasmas* **18** (2011).
73. Connor, J. W. *et al.* A review of internal transport barrier physics for steady-state operation of tokamaks. *Nuclear Fusion* **44** (Apr. 2004).
74. Grandgirard, V. *et al.* A drift-kinetic Semi-Lagrangian 4D code for ion turbulence simulation. *Journal of Computational Physics* **217**, 395–423 (2006).
75. Dif-Pradalier, G., Grandgirard, V., Sarazin, Y., Garbet, X. & Ghendrih, P. Interplay between Gyrokinetic Turbulence, Flows, and Collisions: Perspectives on Transport and Poloidal Rotation. *Physical Review Letters* **103**, 065002 (6 Aug. 2009).
76. Sarazin, Y. *et al.* Large scale dynamics in flux driven gyrokinetic turbulence. *Nuclear Fusion* **50**, 054004 (2010).
77. Jolliet, S. & Idomura, Y. Plasma size scaling of avalanche-like heat transport in tokamaks. *Nuclear Fusion* **52**, 023026 (2012).
78. Dif-Pradalier, G. *et al.* Finding the Elusive ExB Staircase in Magnetized Plasmas. *Phys. Rev. Lett.* **114**, 085004 (8 Feb. 2015).
79. Baker, D. R. *et al.* Thermal diffusivities in DIII-D show evidence of critical gradients. *Physics of Plasmas (1994-present)* **8**, 4128–4137 (2001).
80. Peeters, A. *et al.* Confinement physics of the advanced scenario with ELMy H-mode edge in ASDEX Upgrade. *Nuclear Fusion* **42**, 1376 (2002).
81. Belli, E. A. & Candy, J. Kinetic calculation of neoclassical transport including self-consistent electron and impurity dynamics. *Plasma Physics and Controlled Fusion* **50**, 095010 (2008).
82. Hunter, J. D. Matplotlib: A 2D graphics environment. *Computing In Science & Engineering* **9**, 90–95 (2007).
83. JabRef Development Team. *JabRef* (2014).

Curriculum vitae

Diese Seite wurde aus Datenschutzgründen in der digitalen Version entfernt.

Danksagung

Teile dieser Seite wurden aus Datenschutzgründen in der digitalen Version entfernt.

Die zum Teil sehr aufwändigen Simulationen, auf denen die Ergebnisse dieser Arbeit beruhen, wurden mit folgenden Großrechnern durchgeführt: HELIOS (IFERC-CSC, Aomori, Japan), Hydra (RZG Garching), HPC-FF (FZ Jülich) sowie mehrere kleinere Linuxcluster.